Karlsruhe Institute of Technology

Michael Fidelis Groß

On Time-Resolved 3D-Tracking of Elastic Waves in Microscale Mechanical Metamaterials

2023
Dissertation

On Time-Resolved 3D-Tracking of Elastic Waves in Microscale Mechanical Metamaterials

Zur Erlangung des akademischen Grades eines
DOKTORS DER NATURWISSENSCHAFTEN
von der KIT-Fakultät für Physik des
Karlsruher Instituts für Technologie (KIT)

genehmigte

DISSERTATION

von

M. Sc. Michael Groß
geboren in Bretten

Tag der mündlichen Prüfung: 22. Dezember 2023
Referent: Prof. Dr. Martin Wegener
Korreferent: Prof. Dr. Muamer Kadic

Contents

List of Figures

Publications

Parts of this thesis have already been published ...
... in scientific journals:

- J.A.I. Martínez, M.F. Groß, Y. Chen, T. Frenzel, V. Laude, M. Kadic, and M. Wegener, "Experimental observation of roton-like dispersion relations in metamaterials", *Science Advances.* **7**, eabm2189 (2021),
- M.F. Groß, J.L.G. Schneider, Y. Wei, Y. Chen, S. Kalt, M. Kadic, X. Liu, G. Hu, and M. Wegener "Tetramode metamaterials as phonon polarizers", *Advanced Materials.* **35**, 2211801 (2023),
- M.F. Groß, J.L.G. Schneider, Y. Chen, M. Kadic, and M. Wegener, "Dispersion engineering by hybridizing the back-folded soft mode of monomode elastic metamaterials with stiff acoustic modes", *Advanced Materials.*, 202307553 (2023),

... and presented at the 17th Metamaterials Congress 2023:

- M.F. Groß, J.L.G. Schneider, Y. Wei, Y. Chen, S. Kalt, M. Kadic, X. Liu, G. Hu, and M. Wegener "Tetramode metamaterials as phonon polarizers", 17th Metamaterials Congress, Greece, Crete, September 2023.

Results in cooperation with J.L.G. Schneider have already been published ...
... in a scientific journal:

- Y. Chen, J.L.G. Schneider, M.F. Groß, K. Wang, S. Kalt, P. Scott, M. Kadic, and M. Wegener, "Observation of Chirality-Induced Roton-Like Dispersion in a 3D Micropolar Elastic Metamaterial", *Advanced Functional Materials.*, 2302699 (2023),

of whom I had the pleasure of supervising.

Chapter 1

1 Introduction

Every time I had to answer questions about my work to friends or family, they would stumble about the catchy term of a "metamaterial". Logically, I was prompted to immediately explain this ominous name. I can't help but feel obliged to answer this question here at the beginning of my thesis as well.

My first reply mostly was: "Something that goes beyond a material", which is arguably the most simplistic, yet bland explanation for a metamaterial that I could come up with. Actually, it is nothing more than the translation from Greek of the name proposed by Rodger M. Walser [1] in 2001. It is self-evident that my "audience" would not be satisfied by such meager explanation and demanded more details on the matter. However, there is to the best of my knowledge no rigorous definition of the name that could do justice to all instances of metamaterials that have been designed, discovered or studied so far. Nonetheless, a very appealing definition was given in 2019:

> *"Metamaterials are rationally designed composites made of tailored building blocks that are composed of one or more constituent bulk materials. The metamaterial properties go beyond those of the ingredient materials, qualitatively or quantitatively."[2]*

In my experience, this explanation, albeit phrased somewhat more casually by me, has resonated well even with people that have little to no background in the field.

Historically, metamaterials arguably made their biggest headlines so far in electromagnetism and photonics with the advent of a negative index of refraction [3–5] for electromagnetic waves and all its implications. However, I find examples from mechanics to be easier to grasp in concept. Among them, auxetic metamaterials are probably the most illustrative case [6]. An object that, when compressed axially, contracts laterally instead of expanding is a sufficiently familiar scenario, yet strange enough behavior to convey a glimpse at the vast capabilities and design choices we expect from metamaterials. In other words, the motivation behind metamaterials is to obtain material parameters or behaviors that vastly differ from any "ordinary" material [7] be it glass, metal, or polymers.

In contrast to those "ordinary" materials, metamaterials attain their properties primarily from the artificially and mindfully designed structure of their smallest building blocks, where the material parameters of their constituent material take on a secondary role [2]. For mechanical metamaterials, those building blocks are often times arranged in layers with a spatial periodicity. Thereby, they form an artificial metamaterial crystal, with the smallest building blocks acting as unit cells in analogy to basic solid state physics [8].

In this sense, auxetic metamaterials are just a small group of possible mechanical metamaterials, with plenty more that came up on the heels of their electromagnetic-metamaterial relatives over the last decades [9, 10]. To this date, mechanical metamaterials have developed into an ever growing field of research as was just recently reviewed in [11]. Two noteworthy representatives of the field are the realization of a new material class, namely pentamode metamaterials in 2012 [12], and the discovery of the mechanical counterpart to optical activity, namely acoustical activity in chiral metamaterials in 2019 [13]. The experiments on this elasto-dynamic effect incited, or in the words of the original authors "paved the road for" further studies to shape and tailor the propagation and polarization of elastic waves in three-dimensional (3D) mechanical metamaterials.

To observe acoustical activity, the displacement field induced by time-harmonic elastic waves, which are a superposition of the eigenmodes of the metamaterial, was tracked optically in two dimensions [13] at a single surface of the metamaterial. Tying onto those preceding studies, two goals for this thesis are formulated to expand on such displacement-tracking experiments.

The first goal focuses on the information about the underlying elastic-wave propagation, which lies encoded within the displacement field of the metamaterial. To extract this information, the displacement measurement must be expanded from one to several surfaces of the metamaterial and thus span multiple layers.

The second goal addresses that the displacement field has in general three components in space [14]. For elastic waves, this corresponds to an arbitrary polarization of the waves, which could not be captured fully in [13]. In order to obtain a more complete picture by sensing arbitrary wave or displacement polarizations, the measurement capability must be expanded into the third dimension, thereby including the so-far missing third displacement component.

As aforementioned, the interesting properties of metamaterials arise from sometimes complex mechanisms that are build into the unit cells. As such, metamaterial fabrication can be rather challenging. An established fabrication method is 3D laser microprinting [15]. Due to its enormous design freedom, it enables the production of almost arbitrary 3D structures and metamaterials [16–21]. While metamaterial samples can be fabricated along those lines with a sufficiently large number of a few dozens of unit cells, the unit-cell feature sizes remain on the microscale as the name of the fabrication method suggests.

Consequently, interesting elastic-wave behavior is shifted to ultrasound frequencies and the magnitude of the displacement shrinks down to the nanometer scale. A dedicated wave-tracking setup must thus provide sufficiently fine temporal as well as spatial resolution in its measurement capabilities. In [13], this was achieved by stroboscopic illumination of the metamaterial in a wide-field microscope and subsequent image-processing. How to integrate displacement measurements along the third dimension elegantly into this approach remains elusive to me.

Therefore, I choose to venture along a different path. In this thesis, I realize a self-build setup capable of measuring all three time-dependent components of the displacement field at local regions of interest. At its core, the setup is comprised of a confocal optical back-scattering microscope with a seamlessly integrated laser-Doppler vibrometer. While confocal imaging remains two-dimensional in its displacement-tracking, vibrometry covers the previously unmeasured third dimension. I circumvent stroboscopic illumination by using the high bandwidth of an effectively single-pixel detector in a confocal microscope together with synchronization of elastic-wave excitation and data acquisition. I demonstrate that this setup is capable of measuring time-resolved nanometer-scale displacements along all three spatial directions at ultrasound frequencies. Extending those measurements over a metamaterial through which elastic waves propagate allows to track those waves by their displacement fields and extract their dispersion relation. Subsequently, I present how I used this setup to conduct or supervise experiments on four mechanical metamaterials, each of which incorporate different mechanisms to tailor a specifically desired elastic-wave propagation.

In three cases, I report the observation of an interesting "roton-like" elastic-wave dispersion, which features a large frequency range of backward-waves, i.e. a region of negative refraction, somewhat leading back to [3–5]. Previously, such a behavior was predicted for sound waves in low-temperature liquid helium by Landau and Feynman [22–24] and observed in 1961 [25]. With the realized experimental setup, it is possible to observe such interesting wave behavior and its tailoring for elastic waves at ambient laboratory conditions. The roton-like behavior is induced for each instance by very different means, therefore touching three interesting design choices for elastic-wave control in metamaterials:

1. Nonlocality, where the displacement at a local point does not only depend on its nearest neighbours but also on sites further away [26].

2. Chirality, lifting the degeneracy of otherwise equivalent metamaterial eigenmodes and enabling hybridization [27].

3. The back-folding of soft modes in an extremal Cauchy-elastic material, following their definition of Graeme Milton and Andrej Cherkaev in 1995 [28].

Last but not least, following along the lines of Milton et al., I demonstrate experimentally how such an extremal material can be used as a polarizer device for elastic transverse waves. A task that becomes orders of magnitude simpler, when measuring displacements in three spatial directions simultaneously.

Outline of this thesis

Starting in Chapter 2, I give a brief introduction into linear Cauchy-elasticity as a sub-category of continuum mechanics, since it is the most basic theory to get into mechanical metamaterials. I focus on the generalized Hooke's law in three dimensions, as well as the behavior of elastic waves in simple mass-and-spring models. The Chapter concludes with a summary on 3D laser microprinting as a means for microscale-metamaterial fabrication.

In Chapter 3, I provide insight into the optical metrology I employed to measure displacements in three dimensions. My techniques of choice were confocal microscopy for in-plane displacement measurement, and laser-Doppler vibrometry for supplementing the out-of-plane displacement information. Consequently, I summarize both technologies, namely the data acquisition, data processing and attainable displacement resolution in detail.

In Chapter 4, I report the home-built experimental setup and describe methods for calibration of the system. Furthermore, a demonstration of the time-resolved elastic-wave tracking capabilities is given and extended to band-structure measurements on metamaterial-beam samples. This demonstration encapsulates the methodology which was used on three of the four metamaterials investigated during this thesis, the results of which are presented in the following Chapters as applications of the setup.

In Chapter 5, I present such band-structure-measurement results on two types of metamaterials that achieve a so-called roton-like dispersion for elastic waves. Two vastly different mechanisms are introduced to do so. Firstly, nonlocality and secondly, chirality. For each case, additional theoretic background information is provided which builds on the preceding Chapters before the experimental results are addressed.

In Chapter 6, I illuminate the results of experiments on another two mechanical metamaterials, which are attributed to the class of extremal Cauchy-elastic materials. It is those extremal properties that were exploited to tailor the dispersion relation of elastic waves distinctively. In the first instance, a transverse polarizer for elastic waves, the counterpart to a transverse polarizer in optics is reported. In the second instance, again a roton-like dispersion relation is achieved and modulated by combining extremal Cauchy-elastic properties with an intricate back-folding strategy of dispersion bands.

In closing, Chapter 7 concludes this work with a summary and a brief outlook.

Chapter 2

2 Continuum Mechanics and Metamaterials

This Chapter starts with an outline of basic quantities and relations from continuum mechanics for linear elasticity, which are necessary to understand the behavior of mechanical metamaterials. Since the experiments of this work address dynamic elasticity, an introduction to elastic waves and dispersion relation or band-structure calculations are given. The Chapter concludes with the description of 3D Laser Microprinting as the fabrication method for three-dimensional microscale metamaterials.

2.1 Summary on Linear Elasticity

Continuum mechanics is the theory to describe the response of bodies upon which forces are applied. In general, those bodies may be gases, fluids or solids. Mechanical metamaterials out of a polymer constituent are thus described by solid mechanics. The most simple response model of a solid material is linear elasticity [14]. For linear elastic materials, a body (out of a material) will return into its original shape, when all forces i.e. stresses are removed[1]. The behavior of linear elastic materials is captured by the generalized Hooke's law [29] in three dimensions. The law connects the forces per area, also called stresses, σ on a body, with its deformation, known as strain, ϵ by the effective elasticity matrix $\mathbf{C}$. In the following, I will provide a brief summary of the derivation of those quantities following the book of Gould [14]. Further insights and more rigorous treatments can be found in standard textbooks on the topic [30, 31].

For this Chapter, I will represent tensorial and vectorial quantities as upright bold face symbols, as it is common in the corresponding textbooks. Furthermore, I will use Einsteins sum-convention where necessary.

2.1.1 *The Stress Tensor*

In linear elasticity, forces upon a body can be distinguished into two categories. Forces that act as loads distributed within the volume are called body forces. The most prominent kind of body force is gravity due to the self-weight of the body. Loads that act onto the surface of a body are called surface forces. A complete description of forces on any point of the body is provided by the Cauchy stress tensor σ. To derive this tensor, it is instructive to perform a gedankenexperiment. A body is subjected to external forces on its surface. Cutting this body creates a surface $\Delta A_{\mathbf{n}}$ with unit normal vector $\mathbf{n}$. The forces within the body "emerge" on the newly created surface[2]. The magnitude and direction of the forces $\Delta \mathbf{F}_{\mathbf{n}}$ acting on the surface $\Delta A_{\mathbf{n}}$ are captured by the traction vector, which is locally defined by the limit of a vanishing surface area:

$$\mathbf{T}_{\mathbf{n}} = \lim_{\Delta A_{\mathbf{n}} \to 0} \frac{\Delta \mathbf{F}_{\mathbf{n}}}{\Delta A_{\mathbf{n}}} = \frac{\mathrm{d}\mathbf{F}_{\mathbf{n}}}{\mathrm{d}A_{\mathbf{n}}} \quad . \tag{2.1}$$

Forming the limit, the resulting traction vector specifies the stresses onto a point, however, for a given direction $\mathbf{n}$ only. Logically, a complete description of stress on a point independent of $\mathbf{n}$ is not yet achieved. Nonetheless, the traction vector is

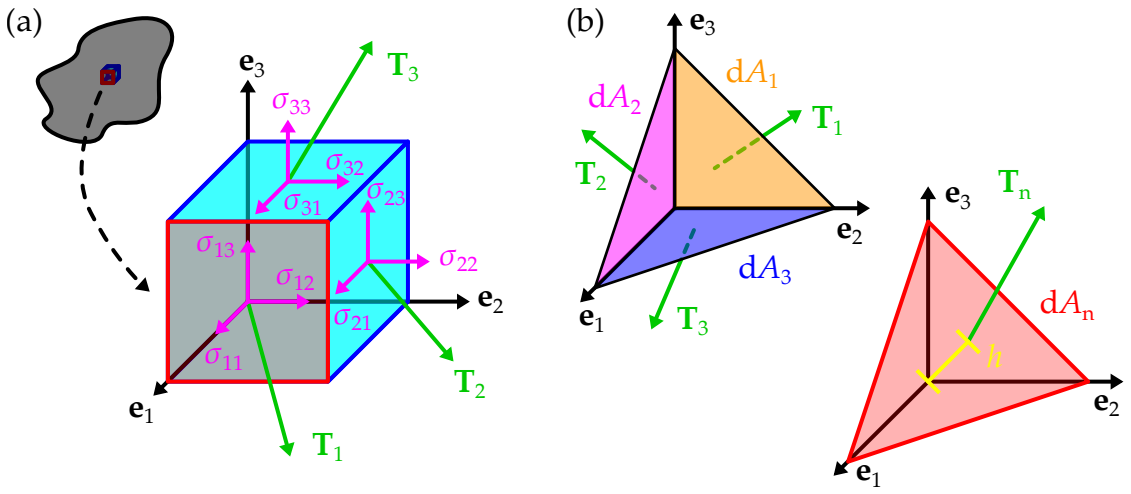

Figure 2.1: Schematics to visualize the derivation of the stress tensor. (a) An infinitesimal cube cut out of some linear elastic material. Each face is acted upon by a traction vector $\mathbf{T}$. The tripods on each face indicate the components of stress along the three Cartesian directions $\mathbf{e}_1$, $\mathbf{e}_2$ and $\mathbf{e}_3$. (b) Tetrahedron to derive stress on arbitrary surface. The top left tetrahedron highlights the back $\mathrm{d}A_1$, side $\mathrm{d}A_2$ and bottom $\mathrm{d}A_3$ surfaces with tractions $\mathbf{T}_1$, $\mathbf{T}_2$ and $\mathbf{T}_3$. On the bottom right, the front surface $\mathrm{d}A_\mathbf{n}$ with traction $\mathbf{T}_\mathbf{n}$ is highlighted in red. The height of $\mathrm{d}A_\mathbf{n}$ from the tip of the tetrahedron is given by h.

a useful tool to get there. Moving forward, a cube with infinitesimal edge length is cut out of a body. The orientation of this cube is chosen as such that the surface normal vectors correspond to the three basis vectors $\mathbf{e}_1$, $\mathbf{e}_2$ and $\mathbf{e}_3$, as depicted in Figure 2.1(a). The traction vector $\mathbf{T}_1$ on the front surface (red outline), can thus be expressed as:

$$\mathbf{T}_1 = \sigma_{11}\mathbf{e}_1 + \sigma_{12}\mathbf{e}_2 + \sigma_{13}\mathbf{e}_3 \,, \tag{2.2}$$

or more generally:

$$\mathbf{T}_i = \sigma_{ij}\mathbf{e}_j, \quad \text{with} \quad i,j \in \{1,2,3\} \,. \tag{2.3}$$

In this notation, the coefficients σ_{ij} are the stresses. The first index (i) relates to the basis vector denoting the face, the second index (j) denotes the direction along which the stress component acts. The next step is to generalize this consideration for surfaces, whose surface normal is not aligned with one of the basis vectors $\mathbf{e}_i$. Therefore, the surfaces of an infinitesimal tetrahedron are inspected, as illustrated in Figure 2.1(b). Again, three traction vectors are considered, acting this time on the back $\mathrm{d}A_1$, side $\mathrm{d}A_2$ and bottom $\mathrm{d}A_3$ surfaces, with normals each aligned with one basis vector. The forth surface $\mathrm{d}A_\mathbf{n}$ closing the tetrahedron is at an angle

[1] For a polymer constituent, a viscoelastic description that includes damping is more precise, but is omitted at this point for simplicity.

[2] Linear elasticity assumes vanishing moments i.e torques on infinitesimal surfaces.

with the basis vectors and has a normal vector $\mathbf{n}$ with components n_i:

$$\mathbf{n} = n_1\mathbf{e}_1 + n_2\mathbf{e}_2 + n_3\mathbf{e}_3 \quad \longleftrightarrow \quad n_i = \mathbf{n} \cdot \mathbf{e}_i \; . \tag{2.4}$$

Since $\mathbf{n}$ is not aligned with any basis vector, it is not possible to write down the components of stress to from the traction vector $\mathbf{T_n}$ right away. Instead, the traction vector has to be derived using Newton's equations of motion [32]. The latter state that the sum of all forces onto the tetrahedron must equal the mass m times the acceleration $\mathbf{a}$. For the following discussion it is sufficient to assume equilibrium of forces with $\mathbf{a} = 0$:

$$\mathbf{T_n}\,\mathrm{d}A_\mathbf{n} - \mathbf{T}_1\,\mathrm{d}A_1 - \mathbf{T}_2\,\mathrm{d}A_2 - \mathbf{T}_3\,\mathrm{d}A_3 + \left(\frac{h \cdot \mathrm{d}A_\mathbf{n}}{3}\right)\mathbf{f} = 0 \; . \tag{2.5}$$

The term with $\mathbf{f}$ represents the body forces onto the tetrahedron, for this case as gravity, and h represents the height of the surface $\mathrm{d}A_\mathbf{n}$ from the opposite tip of the tetrahedron. The areas of the surfaces are related by

$$\mathrm{d}A_i = \mathrm{d}A_\mathbf{n}\,(\mathbf{n} \cdot \mathbf{e}_i) \quad \longrightarrow \quad \mathrm{d}A_\mathbf{n} = \frac{\mathrm{d}A_i}{\mathbf{n} \cdot \mathbf{e}_i} = \frac{\mathrm{d}A_i}{n_i} \; , \tag{2.6}$$

which simplifies the middle three terms of Equation 2.5 to:

$$\left(\mathbf{T_n} - \mathbf{T}_i n_i + \mathbf{f}\frac{h}{3}\right)\mathrm{d}A_\mathbf{n} = 0 \; . \tag{2.7}$$

Applying the limit of $h \to 0$, yields:

$$\mathbf{T_n} = \mathbf{T}_i n_i = \mathbf{T}_1 n_1 + \mathbf{T}_2 n_2 + \mathbf{T}_3 n_3 \; . \tag{2.8}$$

With this equation, the components of $\mathbf{T_n}$ can now be expressed along the basis vectors:

$$T_j = \mathbf{T_n} \cdot \mathbf{e}_j \; . \tag{2.9}$$

Entering Equation 2.3 into Equation 2.8 and relabeling some indices, allows to arrive at the final relation for the components of $\mathbf{T_n}$:

$$T_j = \sigma_{ji} n_j \; , \tag{2.10}$$

or in explicit vector and matrix form:

$$\begin{pmatrix} T_1 \\ T_2 \\ T_3 \end{pmatrix} = \begin{pmatrix} \sigma_{11} & \sigma_{21} & \sigma_{31} \\ \sigma_{12} & \sigma_{22} & \sigma_{32} \\ \sigma_{13} & \sigma_{23} & \sigma_{33} \end{pmatrix} \cdot \begin{pmatrix} n_1 \\ n_2 \\ n_3 \end{pmatrix} \; . \tag{2.11}$$

Therein lies the second order Cauchy stress tensor σ with components σ_{ij}, which describe the stresses within the body along any choice of cutting plane.

A very visually appealing form of this derivation can be found online by Clayton Pettit [33]. In passing it is stated that the stress tensor in the scope of linear elasticity is symmetric:

$$\sigma_{ij} = \sigma_{ji} \ . \tag{2.12}$$

The proof is based on the conservation of angular momentum and the reader is referred to the corresponding literature mentioned at the beginning of this section.

2.1.2 *The Strain Tensor*

Strain of a body describes its deformation under any kind of load. For mechanical metamaterials, strain is especially important, since it is closely linked to the displacement field, which is measured in the experiments. Therefore, I take the time to superficially introduce and derive the strain tensor ϵ, following the literature mentioned above.

The derivation starts with the comparison of a body in two different configurations. The undeformed body is said to be in its reference configuration $\mathbb{R}_0$, and the deformed body is in the current configuration $\mathbb{R}_c$[3]. This is shown in Figure 2.2.

Nomenclature may vary between textbooks and authors. I want to use the convention that any points and quantities referring to the undeformed body in its reference configuration $\mathbb{R}_0$ are expressed with upper case letters. In contrast, for the deformed body in $\mathbb{R}_c$, lower case letters are used.

Each body is comprised out of material points such as $\mathbf{P}$ with position vector $\mathbf{X}$ in $\mathbb{R}_0$. The corresponding point $\mathbf{p}$ in the current configuration $\mathbb{R}_c$ is described by the position vector $\mathbf{x}$. The position vectors are linked by a bijective, continuous and smooth (differentiable) function χ, called the position function. It may be abbreviated as:

$$\chi(\mathbf{X}) = \mathbf{x}(\mathbf{X}) \quad \longleftrightarrow \quad \chi^{-1}(\mathbf{x}) = \mathbf{X}(\mathbf{x}) \ . \tag{2.13}$$

A second vector quantity which describes the displacement of point $\mathbf{P}$ to $\mathbf{p}$ is the important displacement-field function:

$$\mathbf{u}(\mathbf{X}) = \chi(\mathbf{X}) - \mathbf{X} = \mathbf{x}(\mathbf{X}) - \mathbf{X} \ . \tag{2.14}$$

At this point, I want to quickly address rigid body motion. As the name implies, these motions do not deform the body and thus generate zero strain. In the most general case, the position function takes the form:

$$\mathbf{x}(\mathbf{X}) = \mathbf{R} \cdot \mathbf{X} + \mathbf{c} \ , \tag{2.15}$$

[3] For each configuration, the material points occupy different positions in 3D space, and two equivalent descriptions of the body can be found. One either focuses on a fixed point in space and "watches" material points in relation to this point ore one focuses on a material point and "follow" its trajectory through space during deformation.

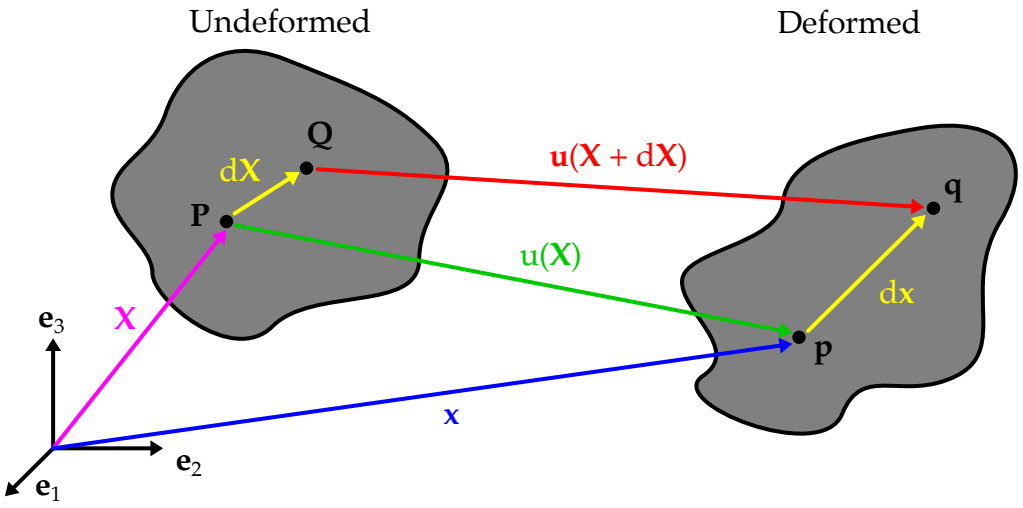

Figure 2.2: Schematics of undeformed body in reference configuration $\mathbb{R}_0$ and deformed body in current configuration $\mathbb{R}_c$ to visualize the derivation of the strain tensor. Upper case letters refer to $\mathbb{R}_0$ and lower case letters to $\mathbb{R}_c$.

with rotation $\mathbf{R}$ of the body and constant shift $\mathbf{c}$. The displacements induced by rigid body motions are excluded from the discussion here, since the experiments reported in this work address fixed samples[4]. More relevant are extensions and contractions of the body, which do induce a strain. This is equivalent to a change in distance $\mathrm{d}\mathbf{X}$ between neighbouring points $\mathbf{P}$ and $\mathbf{Q}$ to $\mathrm{d}\mathbf{x}$ for $\mathbf{p}$ and $\mathbf{q}$, when deforming the body (cf. Figure 2.2). Starting of, two possible paths should be considered when going from the origin to the point $\mathbf{Q}$. The first path is on the left hand side and the second path on the right hand side of the following equation:

$$\mathbf{X} + \mathrm{d}\mathbf{X} + \mathbf{u}(\mathbf{X} + \mathrm{d}\mathbf{X}) = \mathbf{x} + \mathrm{d}\mathbf{x} \,. \tag{2.16}$$

Solving for $\mathrm{d}\mathbf{x}$ and entering $\mathbf{u}(\mathbf{X}) = \mathbf{x} - \mathbf{X}$ equates:

$$\mathrm{d}\mathbf{x} = \mathrm{d}\mathbf{X} + \mathbf{u}(\mathbf{X} + \mathrm{d}\mathbf{X}) - \mathbf{u}(\mathbf{X}) \,. \tag{2.17}$$

The last two terms of Equation 2.17 can be substituted with the difference quotient for the displacement field:

$$\nabla \mathbf{u} = \quad = \frac{\mathrm{d}\mathbf{u}}{\mathrm{d}\mathbf{X}} = \frac{\mathbf{u}(\mathbf{X} + \mathrm{d}\mathbf{X}) - \mathbf{u}(\mathbf{X})}{\mathrm{d}\mathbf{X}} \,. \tag{2.18}$$

Which also defines the displacement-field gradient. Thus:

$$\mathrm{d}\mathbf{x} = \mathrm{d}\mathbf{X} + \nabla \mathbf{u}\, \mathrm{d}\mathbf{X} = (\mathbb{I} + \nabla \mathbf{u})\, \mathrm{d}\mathbf{X} = \mathbf{F}\, \mathrm{d}\mathbf{X} \,. \tag{2.19}$$

[4] The devil's advocate may state that in the experiment, thermal drifts of a sample (body) positions may induce such rigid body motion, which has to be accounted for.

This equation with identity matrix $\mathbb{I}$ defines the so called deformation gradient $\mathbf{F}$. The latter relates a infinitesimal length before deformation to the length after deformation with $\mathrm{d}\mathbf{x} = \mathbf{F}\,\mathrm{d}\mathbf{X}$. When comparing lengths of vectorial quantities, the norms have to be taken:

$$\mathrm{d}\mathbf{x} \cdot \mathrm{d}\mathbf{x} = (\mathbf{F}\,\mathrm{d}\mathbf{X}) \cdot (\mathbf{F}\,\mathrm{d}\mathbf{X}) = \mathrm{d}\mathbf{X}(\mathbf{F}^{\mathrm{T}}\mathbf{F})\,\mathrm{d}\mathbf{X}\,. \tag{2.20}$$

Therein, the Right Cauchy-Green deformation tensor is defined as $\tilde{\mathbf{C}} = (\mathbf{F}^{\mathrm{T}}\mathbf{F})$[5]. Expanding $\hat{\mathbf{C}}$ results in the definition of the strain tensor $\tilde{\epsilon}$

$$\tilde{\mathbf{C}} = (\mathbf{F}^{\mathrm{T}}\mathbf{F}) = \mathbb{I} + \nabla\mathbf{u} + \nabla\mathbf{u}^{\mathrm{T}} + \nabla\mathbf{u}^{\mathrm{T}}\nabla\mathbf{u} = \mathbb{I} + 2\tilde{\epsilon}\,. \tag{2.21}$$

Writing $\tilde{\epsilon}$ in the components of the displacement field is more instructive:

$$\tilde{\epsilon}_{ij} = \frac{1}{2}\left(\frac{\partial u_i}{\partial X_j} + \frac{\partial u_j}{\partial X_i} + \frac{\partial u_i}{\partial X_j}\frac{\partial u_j}{\partial X_i}\right)\,. \tag{2.22}$$

This symmetric tensor is valid for any magnitude of deformation. However in many cases, it is sufficient to limit oneself to small displacements, which very well be true for mechanical metamaterials in the ultrasound regime. Therefore, the infinitesimal strain tensor neglects the product term of derivatives in Equation 2.22, effectively linearizing the strain tensor:

$$\epsilon_{ij} = \frac{1}{2}\left(\frac{\partial u_i}{\partial X_j} + \frac{\partial u_j}{\partial X_i}\right) = \frac{1}{2}\left(u_{i,j} + u_{j,i}\right)\,,\ \text{with}\ u_{i,j} = \frac{\partial u_i}{\partial X_j}\,. \tag{2.23}$$

Similar to the derivation of the stress tensor, a visually appealing explanation of this derivation is found in the online lecture by Clayton Pettit [34].

2.1.3 *The Constitutive (Hooke's) law*

To complete the description of a body under load, the link between the stresses it is subjected to, to the strain that captures its deformation has to be made. This is achieved by the generalized Hooke's law [29] in three dimensions:

$$\boldsymbol{\sigma} = \mathbf{C} \cdot \boldsymbol{\epsilon} = \sigma_{ij} = C_{ijkl}\epsilon_{kl}\,. \tag{2.24}$$

The quantity $\mathbf{C}$ is the stiffness or elasticity tensor. Since both stress and strain are described by second order tensors, $\mathbf{C}$ is of the fourth order and thus has generally $4^3 = 81$ independent components. However, exploiting symmetries, several correlations between those components can be made which vastly reduces

[5] For $\hat{\mathbf{C}} = \mathbb{I}$, no lengths change and rigid body motion is present.

the number of independents. For the sake of brevity, those relations are only mentioned here.

The symmetry of $\sigma_{ij} = \sigma_{ji}$ and $\epsilon_{kl} = \epsilon_{lk}$ allows to describe each tensor with only 6 instead of 9 independent quantities. Furthermore, this means that $\mathbf{C} = C_{ijkl}$ has to be invariant under the permutation of the first two or the last two indices as well. Consequently, the number of independent quantities reduces from 81 to 36. The drastic reduction of independent quantities allows for a reduced index notation, also called Voigt-notation:

$$\hat{\sigma}_1 \to \sigma_{11}, \quad \hat{\sigma}_2 \to \sigma_{22}, \quad \hat{\sigma}_3 \to \sigma_{33}, \quad \hat{\sigma}_4 \to \sigma_{23}, \quad \hat{\sigma}_5 \to \sigma_{31}, \quad \hat{\sigma}_6 \to \sigma_{12}\,, \tag{2.25}$$

$$\hat{\epsilon}_1 \to \epsilon_{11}, \quad \hat{\epsilon}_2 \to \epsilon_{22}, \quad \hat{\epsilon}_3 \to \epsilon_{33}, \quad \hat{\epsilon}_4 \to 2\epsilon_{23}, \quad \hat{\epsilon}_5 \to 2\epsilon_{31}, \quad \hat{\epsilon}_6 \to 2\epsilon_{12}\,. \tag{2.26}$$

From the conservation of energy U in an elastic material, it can be shown (see appendix Section A.1) that $\mathbf{C}$ is symmetric, reducing the number of independent quantities down to 21. Further reductions can be achieved by the use of spatial i.e. material symmetries. If a material has three orthogonal planes of symmetry, it is called an orthotropic material. The stiffness matrix simplifies in Voigt-notation to:

$$\mathbf{C}_{\text{orth}} = \begin{pmatrix} C_{11} & C_{12} & C_{13} & 0 & 0 & 0 \\ C_{12} & C_{22} & C_{23} & 0 & 0 & 0 \\ C_{13} & C_{23} & C_{33} & 0 & 0 & 0 \\ 0 & 0 & 0 & C_{44} & 0 & 0 \\ 0 & 0 & 0 & 0 & C_{55} & 0 \\ 0 & 0 & 0 & 0 & 0 & C_{66} \end{pmatrix}. \tag{2.27}$$

This matrix is among the most general cases and is revisited in Chapter 6 on extremal Cauchy elastic materials. At this point, the Young's E modulus along a Cartesian direction, for example $\mathbf{e}_1$ can be identified:

$$C_{11} = E_{11} = \frac{\hat{\sigma}_1}{\hat{\epsilon}_1}\,. \tag{2.28}$$

This relation represents the uniaxial Hooke's law as it is usually first taught at an introductory level. Another established quantity is the Poisson's ratio ν. It describes the ratio of deformation along the Cartesian direction $\mathbf{e}_2$ and $\mathbf{e}_3$ for stress applied along $\mathbf{e}_1$. Thus, $\sigma_1 > 0$ while all other components are zero, the strains compute to:

$$\hat{\epsilon}_1 = \frac{\hat{\sigma}_1}{E_{11}}\,, \qquad \hat{\epsilon}_2 = -\nu_{12}\frac{\hat{\sigma}_1}{E_{11}}\,, \qquad \hat{\epsilon}_3 = -\nu_{13}\frac{\hat{\sigma}_1}{E_{11}}\,. \tag{2.29}$$

Further simplifications can be made for an isotropic material, where the stiffness

matrix becomes invariant under rotations:

$$\mathbf{C}_{\text{iso}} = \begin{pmatrix} E & -E/\nu & -E/\nu & 0 & 0 & 0 \\ -E/\nu & E & -E/\nu & 0 & 0 & 0 \\ -E/\nu & -E/\nu & E & 0 & 0 & 0 \\ 0 & 0 & 0 & G & 0 & 0 \\ 0 & 0 & 0 & 0 & G & 0 \\ 0 & 0 & 0 & 0 & 0 & G \end{pmatrix} , \tag{2.30}$$

and the shear modulus G and the bulk modulus K are introduced [35]. Due to the isotropic character of the material, all indices for those quantities can be dropped. Furthermore, they are related to each other:

$$E = 2G(1+\nu) , \qquad G = \frac{E}{2(1+\nu)} , \qquad K = \frac{E}{3(1-2\nu)} . \tag{2.31}$$

Obviously, for non-isotropic materials, the moduli will retain their directional dependency and thus indices have to be considered.

In closing, an important remark for the case of mechanical metamaterials has to be made. The material parameters such as E, K and ν are not the parameters of the constituent (i.e. polymer) out of which the metamaterial structure is fabricated. The latter only enter in to the simulation of the microstructure using e.g. finite-element-methods as it was done for this work by Yi Chen and Yu Wei and will be coarsely outlined below. The crucial distinction is that for a metamaterial one always searches for effective material parameters that allow to describe the metamaterial microstructure as a continuum and Hooke's law will then be written with an effective stiffness matrix $\mathbf{C}_{\text{eff}}$.

2.2 Fundamentals of Elastic Waves in Metamaterials

In the discussion above, all accelerations are set to zero. In other words, time-dependencies are neglected up to here and only static cases were considered. The transition to the dynamic behavior is made, which gives rise to elastic waves, the displacement field of which is the core measurement quantity in the experiments of this work.

The linear equation of motion is derived from Newtons second law [32]. Its component-wise formulation in integral form can be written as [14]:

$$\int_V \rho a_i \,\mathrm{d}V - \int_V f_i \,\mathrm{d}V - \int_A T_i \,\mathrm{d}A \overset{\text{(Gauss)}}{=} \int_V \left(\rho a_i - f_i - \sigma_{ij,j}\right) \mathrm{d}V = 0 , \tag{2.32}$$

with body forces f_i, mass density ρ, traction T_i and nonzero acceleration a_i. Here, $\sigma_{ij,j}$ denotes the derivative of σ_{ij} with respect to X_j (cf. Equation 2.23).

For the last equality of Equation 2.32, the divergence theorem (Gauss) on the area integral is used. Obviously, Equation 2.32 is true, when the integrand of the right hand side vanishes [30], such that the differential form reads:

$$\rho a_i - f_i - \sigma_{ij,j} = 0 \,. \tag{2.33}$$

Using the constitutive law (Equation 2.24) and inserting the definition for small strains (Equation 2.23), allows to express this relation in terms of experimentally accessible displacements following the lines of Hunklinger [36, p.169]:

$$\rho \frac{\partial^2 u_i}{\partial t^2} = \frac{\partial \sigma_{ij}}{\partial X_j} = C_{ijkl} \frac{\partial^2 u_l}{\partial X_j \partial X_k} = C_{ijkl} \cdot u_{l,jk} \,. \tag{2.34}$$

2.2.1 *Elastic Waves in Cauchy Continua*

An ansatz can be made, to solve Equation 2.34. For an infinite simple cubic material with its three axis aligned with Cartesian directions $\mathbf{e}_i$, a special case is chosen for demonstration. A wave propagating along the x-axis with wave vector $\mathbf{k} = (k_x, 0, 0)^{\mathrm{T}}$ has a displacement field of:

$$u_1(x,t) = U_1 \exp\left[-\mathrm{i}(\omega t - k_x x)\right], \; u_2 = u_3 = 0 \,. \tag{2.35}$$

Therein, U_1 is the displacement amplitude and i is the imaginary unit. The angular frequency relates to the ordinary frequency as $\omega = 2\pi f$. For this ansatz, a longitudinal polarization of the wave is assumed, which means means that the displacement vector $\mathbf{u}$ (for every position x) is parallel to the wavevector $\mathbf{k}$. Inserting the ansatz into Equation 2.34, yields the dispersion relation, i.e. the relation between wavenumber and frequency:

$$\omega_{\mathrm{long}} = \sqrt{\frac{C_{11}}{\rho}} \cdot k_x = v_{\mathrm{long}} \cdot k_x \,. \tag{2.36}$$

Here, the proportionality constant between k_x and ω is the phase velocity, and in this simple case identical to the velocity of sound, with which a longitudinal wave propagates. The same procedure can be followed for a wave propagating along the x-axis but polarized along the y-axis, i.e. a transverse wave, which propagates with the corresponding velocity:

$$\omega_{\mathrm{trans}} = \sqrt{\frac{C_{44}}{\rho}} \cdot k_x = v_{\mathrm{trans}} \cdot k_x \,. \tag{2.37}$$

Due to the symmetry of the material, the same result will follow for a wave propagating along the x-axis and polarized along the z-axis.

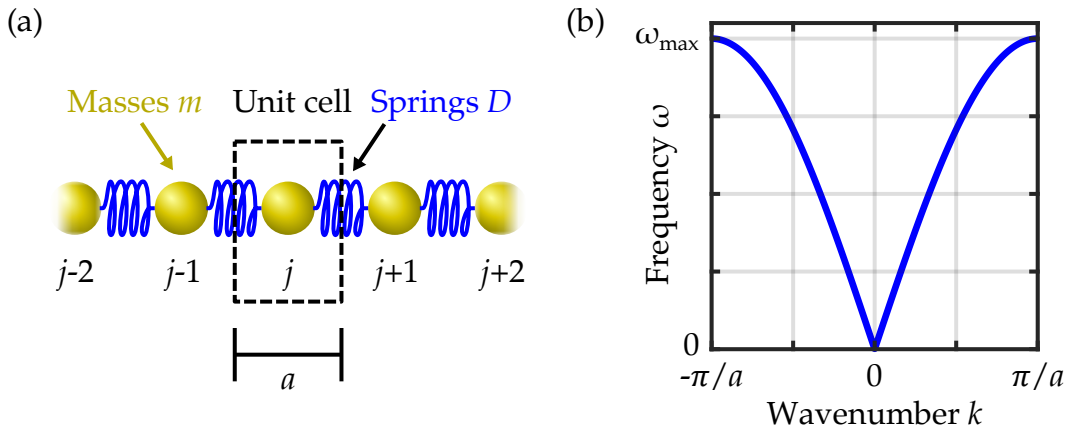

Figure 2.3: 1D chain of identical masses and their elastic-wave dispersion. (a) A segment of the chain. The masses m (yellow) are labeled with j and connected by Hooke springs of constant D. The distance between the masses is a, which is also the length of the unit cell (dashed box). (b) Dispersion relation for elastic waves with wavenumber k in the first Brillouin zone. For this 1D model, a single acoustic band is present.

In other words, these solutions to Equation 2.34 are degenerate. Up to this point, extremely simplified situations were discussed, where the waves propagate along high symmetry axis of the material. For the more general case of waves propagating along arbitrary directions with arbitrary polarizations, the propagation constants will obviously consist of several entries of the stiffness matrix $\mathbf{C}$. Furthermore, the periodicity of the underlying microstructure is not captured. However, this is crucial for the description of mechanical metamaterials.

2.2.2 *Elastic Waves in Periodic Media*

Arguably one of the simplest periodic media one can envision is a linear, one-dimensional (1D) chain of masses m, connected by massless springs of length a with Hooke spring constant D. While simple, the model can teach a lot about the wave propagation in periodic media, which is why it is found in every undergraduate text book on the topic of solid state physics [8, 36, 37]. The reason why it is reiterated here, is that it forms an accessible baseline for the understanding of the metamaterials discussed in Chapter 5.

Infinite Chain of Identical Masses

A segment of an infinite 1D chain comprised of identical masses is depicted in Figure 2.3(a). I chose superscripts for the mass-numbering to avoid confusion with vector components, even though this is a 1D i.e. scalar problem.

To derive the dispersion for elastic waves, the equation of motion according to Newton has to be solved. To do so, only the forces $F^{(j)}$ applied onto the mass j by its direct neighbors $j+1$ and $j-1$ are considered. Furthermore, the time-dependent displacement $u^{(j)}(t)$ of each j-th mass is defined as relative to the rest position[6]. Thus,

$$F^{(j)} = m \cdot \ddot{u}^{(j)} = D\left(u^{(j+1)} + u^{(j-1)} - 2u^{(j)}\right) , \tag{2.38}$$

where $\ddot{u}^{(j)}$ is second derivative of $u^{(j)}$ with respect to time. For the solution, the ansatz is made:

$$u^{(j)} = U \cdot \exp\left[-\mathrm{i}(\omega t - k \cdot j \cdot a)\right] , \tag{2.39}$$

with amplitude U. Inserting Equation 2.39 into Equation 2.38 yields the dispersion for the elastic waves:

$$\omega(k) = \sqrt{\frac{4D}{m}} \cdot \left|\sin\left(\frac{ka}{2}\right)\right| , \tag{2.40}$$

which only shows a single (acoustic) band and is plotted in Figure 2.3(a). Technically, Equation 2.40 is valid for $k \to \pm\infty$. Léon Brillouin [38] showed that it is sufficient to only inspect a limited range of k. This zone is called the first Brillouin zone (BZ). The size of the latter, is defined by the size of the primitive unit cell, highlighted as dashed box[7] in Figure 2.3(a). The bands that exceed the first BZ can be back-folded due to the symmetry of the crystal. Such back-folding is revisited in Chapter 6 of this thesis.

Finally, it becomes apparent that when taking into account the micro structure of the body or material, a vastly different dispersion relation for elastic waves will follow (cf. Equation 2.40 to Equation 2.36). It is only for small values of k, where the linear relationship between k and ω recovers in Equation 2.40.

Infinite Chain of Two Differing Masses

Obviously, the 1D consideration of a chain with identical masses falls short of an accurate description of a sophisticated mechanical metamaterial. A unit-cell in a metamaterial is comprised of much more than a single point of mass. The first expansion to be made, is to let every second mass M be larger then the original masses m. This model is illustrated in Figure 2.4(a). Naturally, the lattice periodicity has now changed from a to $2a$.

[6] The argument of $u^{(j)}(t)$ is dropped at this point for the sake of readability.

[7] Other choices of the unit cell will only alter the corresponding representation in k-space. However, the physics of wave propagation will remain invariant.

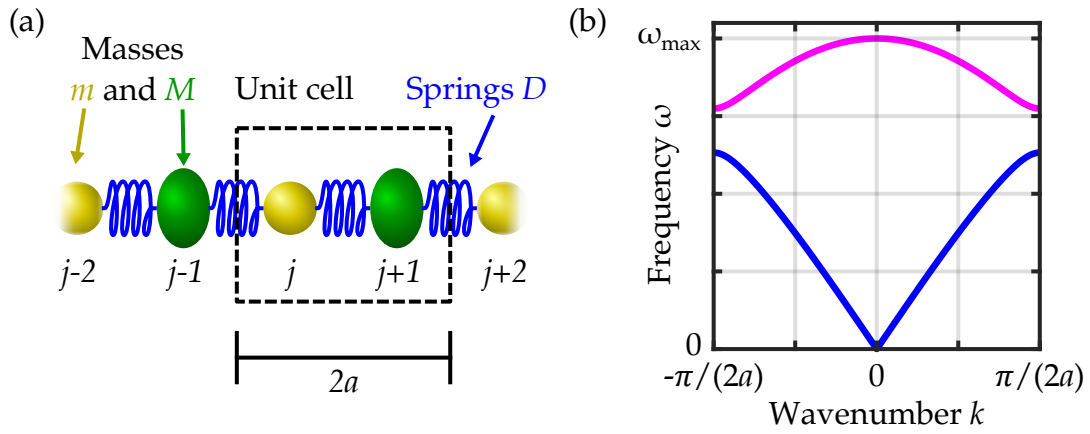

Figure 2.4: In analogy to Figure 2.3, but for two types of masses and their elastic-wave dispersion. (a) A segment of the chain with masses $M > m$, connected by Hooke springs of constant D. The length of the unit cell (dashed box) is twice the distance a between neighboring masses. (b) Dispersion relation for elastic waves with wavenumber k in the first Brillouin zone. An additional optical band (magenta) is formed, which is higher in frequency than the acoustic band (blue).

A coupled set of equations of motions results:

$$m\ddot{u}^{(j)} = D\left(u^{(j+1)} + u^{(j-1)} - 2u^{(j)}\right) , \tag{2.41}$$

$$M\ddot{u}^{(j+1)} = D\left(u^{(j+2)} + u^{(j)} - 2u^{(j+1)}\right) , \tag{2.42}$$

which is solved using the ansatz with complex amplitudes A and B:

$$u^{(j)} = A \cdot \exp\left[-\mathrm{i}(\omega t - k \cdot j \cdot a/2)\right] , \tag{2.43}$$

$$u^{(j+1)} = B \cdot \exp\left[-\mathrm{i}(\omega t - k \cdot (j+1) \cdot a/2)\right] . \tag{2.44}$$

Herein, two solutions, i.e. two bands appear in the dispersion relation:

$$\omega_{\mathrm{opt}}^2 = D\left(\frac{1}{M} + \frac{1}{m}\right) + D\sqrt{\left(\frac{1}{M} + \frac{1}{m}\right)^2 - \frac{4}{mM} \cdot \sin^2\left(\frac{ka}{2}\right)} , \tag{2.45}$$

$$\omega_{\mathrm{ac}}^2 = D\left(\frac{1}{M} + \frac{1}{m}\right) - D\sqrt{\left(\frac{1}{M} + \frac{1}{m}\right)^2 - \frac{4}{mM} \cdot \sin^2\left(\frac{ka}{2}\right)} . \tag{2.46}$$

The two bands are plotted in Figure 2.4(b). The lower band is called an acoustic band, while the upper band is termed an optical band. In short it can be stated that for every mass (i.e. atom) in the unit cell, and for every degree of freedom of such mass, an additional band emerges. The chirality-induced interplay and admixture of optical and acoustic bands is revisited in Chapter 5.

The solution of the coupled equations of motion above mathematically require the computation of an eigenvalue problem. Intuitively, the complexity and dimensionality of the matrices and vectors involved, increases dramatically when generalizing to real world samples. Therefore, the computation is generally performed using numerical means, which are outlined in the next section.

Summary

A very important conclusion for the methodology and experiments of this thesis can be drawn from the consideration above. Since metamaterial samples in the real-world are finite in dimension, the boundary conditions of these models have to be changed[8]. As a consequence, the propagating elastic waves will form a standing wave pattern from the superposition of waves propagating with k and back-reflected waves at the end of the sample, propagating with $-k$. The real part of the solutions for the corresponding equation of motion with the respective boundary conditions allow to compute an amplitude envelope of the finite chain (or metamaterial sample). For the case of the 1D chain of identical masses, this yields the amplitude envelope:

$$u(r = a \cdot j, t) = 2U \cdot \sin(k \cdot a \cdot j) \cdot \sin(\omega t) \ , \tag{2.47}$$

from which the time-dependency $\sin(\omega t)$ can be separated without loss of generality. Fourier transformation of this amplitude envelope with respect to the spatial coordinate $r = a \cdot j$ reveals the mode content at the frequency ω. Repeating this procedure for a range of frequencies ω extracts the band structure or dispersion relation of the chain.

Generalizing the $u(r, t)$ to a body comprised of points in 3D space that can be displaced along all three spatial directions, yields the three-dimensional displacement field $\mathbf{u}_{\mathbf{k},n}(\mathbf{r})$ with wave vector $\mathbf{k}$ and band index n of the elastic waves. It is exactly this displacement field that is sampled by the experimental setup I build for this thesis and that is described in Chapter 4. Spatial Fourier transformation of the displacement field along the direction of wave propagation in the metamaterial samples reveals the underlying elastic-wave dispersion or band structure and provides the information about the propagating elastic waves within the metamaterial.

[8] E.g. fixed masses with zero displacment at the first and last mass, or considering a ring of masses instead (cf. [8])

2.2.3 *On Numerical Band-Structure Calculations*

When modeling simple linear and 1D chains as described above, it is relatively easy and straightforward to find analytic solutions for the propagation of elastic waves and their respective displacement fields. For more sophisticated structures, like mechanical metamaterials, analytic solutions may be next to impossible to derive and numerical methods such as finite-element-analysis (FEA) have to be used. For the materials investigated in this thesis, this analysis was carried out by Yi Chen and Yu Wei who are co-authors and collaborators in the corresponding publications. They used the commercially available COMSOL Multiphysics package and the MUltifrontal Massively Parallel sparse direct Solver (MUMPS) to arrive at their results. Since the author himself did not perform any such analysis, only the governing equations that were solved are reported in short summary and for the sake of integrity. In order to find the eigenfrequencies $\omega_{\mathbf{k},n}$, with Bloch wavevector $\mathbf{k}$ and integer band index n, the rewritten linear elasticity Equation 2.33, now:

$$\frac{E}{2(1+\nu)(1-2\nu)}\nabla\left(\nabla\mathbf{u}_{\mathbf{k},n}\left(\mathbf{r}\right)\right)+\frac{E}{2(1+\nu)}\nabla^2\mathbf{u}_{\mathbf{k},n}\left(\mathbf{r}\right)=-\rho\omega_{\mathbf{k},n}^2\mathbf{u}_{\mathbf{k},n}\left(\mathbf{r}\right)\ , \quad (2.48)$$

is solved. The Bloch wavevector $\mathbf{k}$ is linked to the assumption of a certain type of wavefunctions for the displacement field, the Bloch waves $\boldsymbol{\psi}_{\mathbf{k},n}(\mathbf{r})$. These functions comprise of a lattice periodic function $\mathbf{u}_{\mathbf{k},n}$ with

$$\mathbf{u}_{\mathbf{k},n}(\mathbf{r})=\mathbf{u}_{\mathbf{k},n}(\mathbf{r}+\mathbf{R})\ , \quad (2.49)$$

and a complex phase factor such that [39]:

$$\boldsymbol{\psi}_{\mathbf{k},n}(\mathbf{r})=\exp\left(\mathrm{i}\mathbf{k}\mathbf{r}\right)\cdot\mathbf{u}_{\mathbf{k},n}(\mathbf{r})\ , \quad (2.50)$$

and thus

$$\boldsymbol{\psi}_{\mathbf{k},n}(\mathbf{r}+\mathbf{R})=\exp\left(\mathrm{i}\mathbf{k}\mathbf{R}\right)\cdot\boldsymbol{\psi}_{\mathbf{k},n}(\mathbf{r})\ . \quad (2.51)$$

Therein, $\mathbf{R}$ is a real-space vector that shares the same lattice periodicity as the underlying structure. In words, the eigenmodes of a periodic system will differ between equivalent sites at $\mathbf{r}$ and at $\mathbf{r}+\mathbf{R}$ only by a complex phase factor. This requirement is used as a boundary condition in numerical computation along a direction, where the sample is assumed to be infinite[9]. Consequently, $\boldsymbol{\psi}_{\mathbf{k},n}$ is fully defined when a solution for $\mathbf{u}_{\mathbf{k},n}$ is found.

Furthermore, the time-harmonic response of a metamaterial sample is computed for an excitation with angular frequency ω using:

$$\frac{E}{2(1+\nu)(1-2\nu)}\nabla\left(\nabla\mathbf{u}_{\omega}\left(\mathbf{r}\right)\right)+\frac{E}{2(1+\nu)}\nabla^2\mathbf{u}_{\omega}\left(\mathbf{r}\right)=-\rho\omega^2\mathbf{u}_{\omega}\left(\mathbf{r}\right)\ . \quad (2.52)$$

[9] These boundary conditions are also known as Floquet-boundaries.

In these equations, the material moduli according to Equation 2.28 and Equation 2.31 of the constituent material (polymer) enter. Damping due to viscoelasticity of the polymer can be modelled by an imaginary part of E. Both Equation 2.48 and Equation 2.52 were solved by Yu Wei and Yi Chen to predict the behavior of the metamaterials investigated in the scope of this thesis and addressed in Chapter 5 and Chapter 6.

2.3 Metamaterial Fabrication by 3D Laser Microprinting

To investigate any digitally-designed metamaterial experimentally, a translation device from the digital domain into the real world is needed. In principle, two pathways can be chosen. Well established subtractive manufacturing techniques, such as milling or cutting, which create the desired structure out of a raw material using computer numerical control, may come to mind first. However, a distinct peculiarity of 3D Metamaterials is their often highly complex geometry. This makes them challenging or even impossible to fabricate in such a manner. The milling head or cutter may simply not reach out to some of the positions where material should be removed, since they may be obstructed to the instrument by desired geometrical features.

In contrast to this methodology stands additive manufacturing with its several instances of 3D printers. For the mechanical Metamaterials investigated in this work, direct 3D laser printing was chosen. This technology is well established in the field [15] and allows to produce almost arbitrary 3D microscale polymer structures in sufficient quantity to form photonic [40, 41] or phononic crystals [42]. Therefore, this technology will be summarized in the following text.

2.3.1 *Principle and Workflow of 3D Laser Printing*

The technique of 3D Laser printing can conceptually be explained in very few words. A Laser beam is focused into a liquid negative-tone photoresist and induces a polymerization reaction [43, 44]. This phase-transition from liquid to solid creates a volume element, also called "voxel" following the style of "pixel" for two-dimensional images. The voxel is by definition the smallest building block a given 3D printer can realize. Scanning the laser focus in three dimensions through the photoresist builds up the structure one wants to realize. Finally, the residual photoresist needs to be washed away to reveal the structure. This workflow is depicted in Figure 2.5.

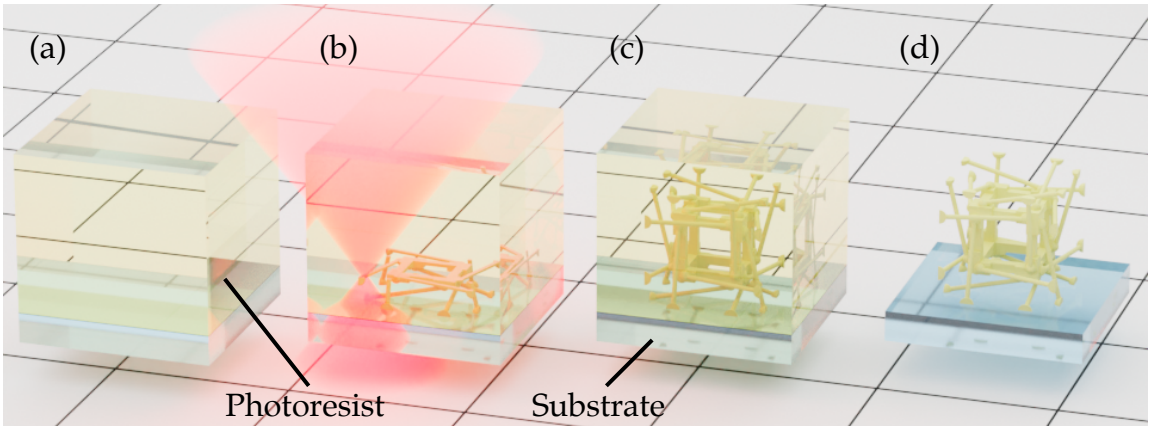

Figure 2.5: Depiction of a typical workflow to fabricate a 3D microstructure. (a) Liquid photoresist on a glass substrate. (b) A laser beam (red) is focused tightly into the photoresist. This exposure induces a 2-photon polymerization reaction at the focal region which additively builds the structure. (c) The printed microstructure, in this case a unit cell from [45], is still submerged in liquid photoresist. (d) Final microstructure after the unpolymerized photoresist is washed away using appropriate solvents. Inspired and adapted from [46, 47].

The intuitive question is now to ask about size of the structures and the speed with which they can be fabricated using this technology. In other words, what is the size of such voxels, and how quickly can these voxels be produced and connected. The answer to this question depends on various factors such as the photoresist system, the power and wavelength of the laser light source, the scan speed of the laser focus, and the optical components used in the printer. However, what is common about state-of-the art 3D laser printers is the use of two-photon absorption [48]. Using a non-linear process, instead of a single-photon absorption to trigger the polymerization response from the photoresist drastically reduces the voxel size and allows for even finer geometrical features to be realized [41]. At first glance, building up any structure sequentially out of tiny blocks may appear inherently slow. However, a laser focus can be scanned extremely fast. For this task, a common choice are galvanometric scanners. These devices are limited by the inertia of the mirrors and mechanics but nonetheless achieve extremely high focus velocities of $> 0.1\,\mathrm{m\,s^{-1}}$ in the writing plane, which places such printers among the fastest devices in the field. An overview and benchmarking of the multiple techniques and devices can be found in work of my colleagues [49]. As a summary, commercially available 3D laser printers are up to the task to fabricate metamaterial structures with hundreds of unit cells resulting in centimeter sized samples in a few hours while maintaining a minimum geometrical feature size of only a few micrometers [49, 50].

2.3.2 *Commercial Laser Printer*

The metamaterial samples I investigated in this work were fabricated with a commercially available 3D laser printer, the Photonics Professional Galvo Technology (PPGT, Nanoscribe) in conjunction with the 3D Microfabrication Solution Set Medium Features (3D MF, Nanoscribe).

The layout of the printer is shown in Figure 2.6. As standard issue for the PPGT, a pulsed frequency doubled erbium fiber laser with a pulse width below 100 fs, a repetition rate of 80 MHz and an emission wavelength centered at 780 nm is used. The laser power is controlled with an acousto-optic modulator. The maximum average laser power at the back-focal plane of the objective lens is 50 mW. The laser beam is focused onto a indium-tin-oxide (ITO) coated substrate by a 25× objective lens with a numerical aperture of NA = 0.8 (LCI Plan-NEOFLUAR, Zeiss). The ITO coat increases the refractive index contrast between photoresist and substrate, which facilitates to find the interface between photoresist and substrate. To fabricate metamaterial structures with the 3D MF, a commercially available photoresist (IP-S, Nanoscribe) is used. The printer features a "DIP-in" operation mode, in which the objective lens is directly immersed into the liquid photoresist. For the 3D MF, the writing field over which the laser focus can be scanned laterally by the galvanometric mirrors while maintaining has a diameter of 400 µm. If the structure exceeds this area, an xy-stage can translate the substrate laterally and stitching of the structure is required. The lateral size limit is hence given by the substrate size of 25 mm × 25 mm. Axial scanning of the laser focus is achieved by a microscopy z-drive, which moves the objective lens closer or further away from the substrate. The maximum height of the printed structure is limited by the travel range of the drive at about 8 mm (depending on substrate holder). In this configuration, the printer achieves a voxel size of 500 nm with a focus velocity of 100 mm s^{-1} are possible, resulting in a voxel rate of about 200000 s^{-1}. All specifications of the printer can be found on the website of the manufacturer [51].

2.3.3 *Sample Fabrication*

For the better understanding of the overall metamaterial fabrication procedure, I want to summarize crucial steps to arrive at a physical metamaterial sample from a numerical computer generated file. The metamaterials I investigated in my thesis were designed using the commercial COMSOL Multiphysics by Yi Chen or Yu Wei. The software provides the geometry data within an STL-file that has to be processed further.

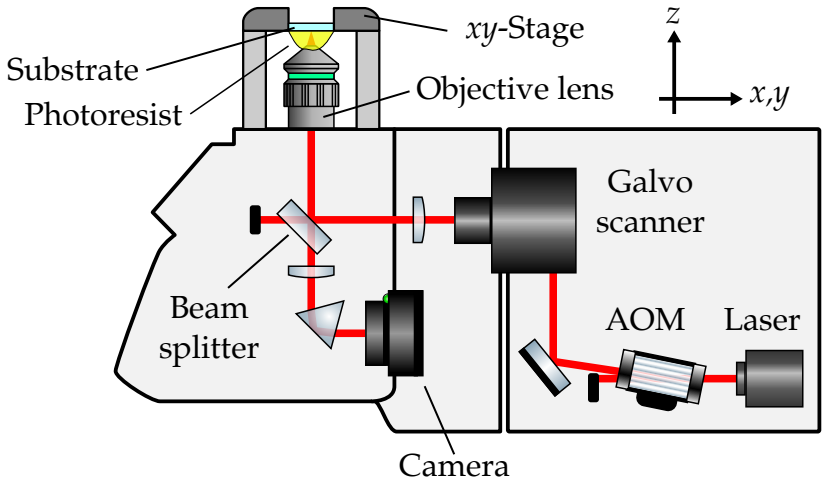

Figure 2.6: Schematic of the commercial laser printer (PPGT, Nanoscribe). The system resembles a confocal microscope in the inverse configuration. A femtosecond-pulsed laser beam (red) is focused by a microscope objective lens into a liquid photoresist, to induce a polymerization reaction via a nonlinear two-photon process. To adjust the laser power, an acousto-optic modulator (AOM) is used. The laser beam is scanned through the writing (x, y)-plane at the substrate surface using a galvanometric (Galvo) scanner. A microscope z-drive can be used (not shown) to move the objective lens axially. The printing process can be observed in real time with a build-in camera. Reproduced and adapted after [47, 51].

Machine Code Generation

To control the laser printer, the STL-file is translated into machine code with the commercially available DeScribe software (Nanoscribe). This code consists of trajectories along which the laser focus is scanned to polymerize the photoresist. To do so, the geometry is sliced into layers separated by the slicing distance d_{slice}. The resulting layers are hatched in-plane with trajectory lines spaced by the hatching distance d_{hatch}. These parameters can have a major influence on sample quality and printing time and are usually optimized for each type of metamaterial individually. A depiction of d_{slice} and d_{hatch} is shown in Figure 2.7(a). Furthermore, it may be necessary to dissect the geometry into smaller parts and slice these individually. Doing so allows for control over the order in which the parts are printed. If a structure features larger overhanging parts, or parts that are not initially connected when printing from the ground up, this method is indispensable to arrive at a well defined sample. In general, for each metamaterial a dedicated printing strategy has to be chosen. Last but not least, depending on the geometry, another important compensation step has to be taken into account.

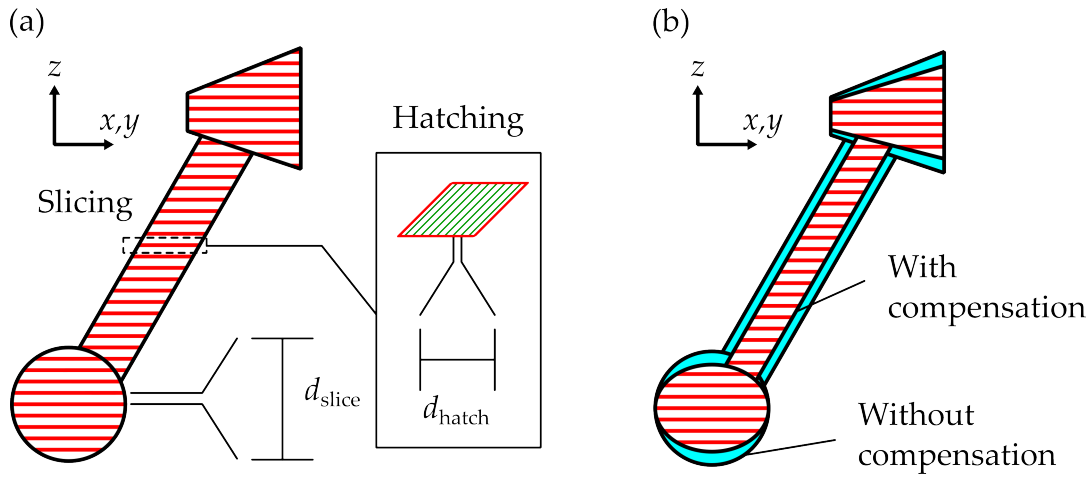

Figure 2.7: (a) Depiction of slicing planes (red) of a 3D geometry (black outline) through which the laser focus is scanned. The inset shows one such plane where the green lines represent the hatching lines i.e. the trajectories for the laser focus. The slicing distance d_{slice} and hatching distance d_{hatch} are marked. (b) Correction of the geometry to compensate for the asymmetry of the voxel along the z-axis. The light blue frame shows the uncompensated structure. The red lines are analogous to (a). The figure was inspired by Jonathan Schneider.

Voxel Compensation

In 3D printing, the voxels are elongated along the axis of the laser beam [52]. As a consequence, certain thin features which consist of only a few voxels may share the same elongation. Therefore, before generating machine code for the printer, the geometry data has to be scaled along this axis to precompensate for the voxel asymmetry. For most metamaterials I investigated in my thesis, this compensation was essential to arrive at a sample with high fidelity to its intended design. An illustration of the intended structure and a compensated structure is shown in Figure 2.7(b). Essentially, the geometry (or each component separately) is compressed along the axis of the laser beam.

Sample Developement

After printing, the sample is still submerged in unpolymerized photoresist. An appropriate method to remove the resist is either a bath of mr-Dev 600 (Micro Resist Technology) or alternatively propylene glycol methyl ether acetate (PGMEA) as a solvent. For the samples subject to this work, the submersion duration was at least 20 min, before the samples were transferred to either a bath of acetone or ethanol. Very delicate structures may be damaged when removing the sample from the bath due to capillary forces when air drying. To circumvent damage, supercritical point drying in CO_2 with a commercial device (EM CPD300, Leica) is necessary.

This concludes the fabrication process of a metamaterial sample. For the sake of integrity, I will state the fabrication parameters for each metamaterial investigated in this work in the corresponding Chapter. Tobias Frenzel and Jonathan Schneider performed the steps of designing a printing strategy and handled the voxel compensation for three out of the four metamaterials I investiagted.

Chapter 3

3 Optical Metrology for Displacement Measurement

To the human being, tracking any kind of object movement is done first and foremost visually. In more scientific terms, we track changes in position of an object, also called displacements, through optical means. In terms of mechanical metamaterials, as has been discussed in Chapter 2, the time-dependent displacement encodes the information about the dispersion relation of elastic-wave propagation in the material. In this Chapter, I introduce the methods from optical metrology I used to measure displacements in three dimensions. Therefore, I start with a brief introduction on confocal microscopy, as such a microscope forms the backbone of the experimental setup. Then, I summarize the image-processing algorithm used to extract in-plane displacement information well below the optical resolution limit. Lastly, I introduce and explain laser-Doppler vibrometry as a technology to provide the out-of-plane displacement information.

3.1 Confocal Optical Microscopy

The term confocal connotes "having the same focus". In the simplest case, this is meant with points in space in mind, which are imaged onto each other by a lens. In addition, there is either a slit or a pinhole involved that suppresses light originating from neighboring i.e. out-of-focus points. This increases image contrast significantly and results in the spatial sectioning for which the confocal imaging technologies are know.

The idea to use confocality for imaging dates back to Hans Goldmann in 1940 [53], who used a confocal system to increase the quality of images from the human eye. This concept was expanded by M. Minsky in 1955 with the invention of the first confocal scanning microscope [54, 55]. In such a system, there are in fact three points that fulfill the criterion of confocality. The first point is the light source illuminating the sample, the second point lies behind a microscopy objective lens and hence on the sample under investigation, and the third point is situated on a pinhole right in front of a photodetector. The latter records the light originating from the focal point on sample. This principle is depicted in Figure 3.1. To achieve the conjugation of all three points, the beam path has to be unfolded by a beam splitter. The previously mentioned pinhole in front of the detector strongly suppresses light originating from points that are not in the focus of the objective lens. The suppression increases dramatically with increasing axial distance from the focal spot of the objective lens. Shrinking the diameter of the pinhole enhances this suppression even further, but also reduces the overall available optical signal power, calling for sensitive photodetectors. So far, only light from a single point is detected efficiently. To generate two-dimensional sectioning images of a sample, the illumination has to be scanned through the focal plane of the objective lens. Recording the spatially resolved intensity profile during scanning allows to reconstruct images from the sample.

In principle, a confocal microscope can operate in two modes. In the first mode, the illumination excites a light source such as a fluorophor in the sample volume. The Stokes-shifted fluorescence light serves as the signal from which image contrast is generated. Usually, a wavelength selective beam splitter separates the illumination light from the fluorescence light. This application is widely spread in biology for cells and living tissue [56]. The second mode simply uses the back-reflected light from the sample surfaces. Image contrast is thus generated by the refractive index difference between either air (or immersion oil) and the sample.

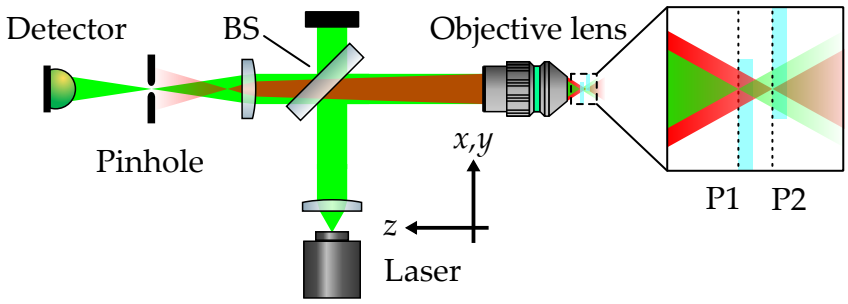

Figure 3.1: Schematic of the beam path in an confocal optical microscope. The illumination is provided by a laser. A beam splitter (BS) directs the laser beam (green) towards an objective lens which focuses the light onto a sample (light blue squares). Back-reflected light from the focal plane (P1) of the objective lens is collected and collimated by the same lens and focused through a pinhole. The light that passes through the pinhole falls onto a detector. Back-reflected light (red) from sample layers beyond the focal plane of the objective lens (P2) is not collimated by the objective lens. This creates a defocus in the plane of the pinhole which leads to a strong reduction in transmission and hence suppression of the background signal. The inset shows a magnification of the objective lens focal region.

Components

The scanning of the focus was historically first implemented by moving the sample with respect to the objective lens [55]. With the advent of lasers as light sources, providing highly directed beams, a lens scanning technique was employed [57]. Nowadays, galvanometric scanners are the preferred choice [58] to scan the laser beam over the sample. Similar to in a 3D laser printer, they enable much faster scanning of the laser focus. A larger scan speed poses some requirements on the detector. The photodecetor must provide a sufficiently large analog bandwidth, to keep up and capture the fast intensity fluctuation of the optical signal when the laser focus is scanned. Additionally, the detector must be sensitive enough to detect even small optical signals, which are common when using small pinhole diameters. Photodetectors, such as photomultiplier tubes (PMT) or avalanche photodiodes (APD) are up to the task by providing a build-in amplification of even small optical signals while offering a high analog bandwidth on the order of several megahertz [59]. This fast response is essential for the methodology introduced in this thesis within the following Chapter.

Resolution of an Confocal Optical Microscope

In microscopy, two criteria for the resolution are common. On one hand, there is E. Abbes criterion from 1873 for illuminated gratings [60]. It states that in order to recover the grating period correctly, the opening angle of the observing (objective) lens must at least collect the zeroth and the first order diffracted beam. On the other hand, the Rayleigh criterion considers self-luminous objects [61] which is an intuitive match for fluorescence microscopy.

However, an experimentally more accessible quantity to judge the resolution of an confocal microscope is the point-spread function (PSF). This function describes how the intensity distribution of an ideal point size light source is altered when viewed through the lens system. Even for an ideal lens system with no aberrations, the intensity distribution will be enlarged along all three spatial directions due to diffraction [62]. A metric to consider here is the full-width at half maximum along lateral $\mathrm{FWHM}_{\mathrm{lat}}$ and axial $\mathrm{FWHM}_{\mathrm{ax}}$ cuts through this function. Objects that are closer together than the respective FWHM cannot be resolved by the imaging system. Strictly speaking, these quantities are defined for self-luminous objects[1]. Nevertheless, their scaling law with respect to illumination wavelength λ and numeric aperture NA of the objective lens are identical to both Ernst Abbes and Rayleighs criteria. Instead of looking at absolute widths in space, it is convenient to use the Airy disk diameter d_{Airy} to set the scale along the lateral direction. This length is also known as Airy unit (AU):

$$d_{\mathrm{Airy}} = 1\ \mathrm{AU} = 1.22 \cdot \frac{\lambda}{\mathrm{NA}} \,. \tag{3.1}$$

Expressing the pinhole diameter d_{Ph} in AU facilitates the comparison of different imaging conditions and confocal microscope setups. To do so, d_{Airy} must be multiplied with the total microscope magnification, in order to obtain the correct value of one AU in the pinhole (or image) plane, since Equation 3.1 is valid for the focal plane of the objective lens. For a pinhole diameter that is several times larger than the Airy unit (in the plane of the pinhole), say $d_{\mathrm{Ph}} > 3$ AU, the lateral and axial resolution of the confocal microscope resembles that of a conventional wide-field system:

$$\mathrm{FWHM}_{\mathrm{lat}} = \frac{0.51 \cdot \lambda}{\mathrm{NA}} \,, \tag{3.2}$$

$$\mathrm{FWHM}_{\mathrm{ax}} = \frac{0.88 \cdot \lambda}{n - \sqrt{n^2 - \mathrm{NA}^2}} \,, \tag{3.3}$$

with refractive index n. For a vanishing pinhole diameter, or at least $d_{\mathrm{Ph}} < 0.25$ AU, the values of the FWHM will decrease by a factor of $1/\sqrt{2}$ [63].

[1] Self-luminous point sources are (reflecting) gold nanoparticles or (fluorescent) quantum dots.

Hence, the theoretical limit for the resolution yields:

$$\mathrm{FWHM}_{\mathrm{lat}} = \frac{0.37 \cdot \lambda}{\mathrm{NA}}\,, \qquad (3.4) \qquad \mathrm{FWHM}_{\mathrm{ax}} = \frac{0.64 \cdot \lambda}{n - \sqrt{n^2 - \mathrm{NA}^2}}\,. \qquad (3.5)$$

With a light source in the visible spectrum, such as a frequency doubled solid-state laser with an emission wavelength of $\lambda = 532\,\mathrm{nm}$ and the use of an air objective lens ($n = 1$) with $\mathrm{NA} = 0.6$, the resolution computes to $\mathrm{FWHM}_{\mathrm{lat}} = 0.3\,\mu\mathrm{m}$ and $\mathrm{FWHM}_{\mathrm{ax}} = 1.7\,\mu\mathrm{m}$.

Summary

Confocal laser scanning microsopy is an optical imaging technology with spatial sectioning due to the collection of light through a pinhole. A practical measure for the resolution of a confocal microscope is the FWHM of the PSF. A smaller pinhole diameter enhances the resolution of the system at the cost of optical signal intensity. Furthermore, the diameter of the pinhole dictates the stray-light suppression from out of focus sample planes, which increases contrast and thus the quality of optical images. A smaller pinhole diameter leads to a stronger suppression and therefore to finer sectioning. In theory, the finest sections can be obtained for a vanishing diameter of the pinhole. Obviously, this is be accompanied by a vanishing transmission through the pinhole and hence no photodetector signal at all. Even when using highly sensitive detectors such as photomultiplier tubes or avalanche photodiodes, the choice of the pinhole diameter remains a trade-off between stray-light suppression and available signal power.

Besides, choosing a too-fine optical sectioning can have additional drawbacks, depending on the subsequent image processing. This problem is elaborated on in Chapter 4, where digital-image cross-correlation analysis for image data obtained with an optical sectioning technique is addressed.

3.2 Digital-Image Cross-Correlation Analysis

In the investigation of microscale mechanical metamaterials, digital-image cross-correlation (DIC) analysis [64] has become an indispensable tool to extract the displacement field in two dimensions [13, 17, 19, 20, 65, 66]. The magnitude of the local displacement-field components, depending on the situation, are on the order of only a few nanometers. Hence, they are well below the resolution limit of a conventional optical microscope operating in the visible regime, as calculated with Equation 3.4. However with DIC, depending on signal-to-noise ratio of the images, a measurement accuracy of down to 1/100 of the pixel size [18], or even to the atomic-scale is possible [67].

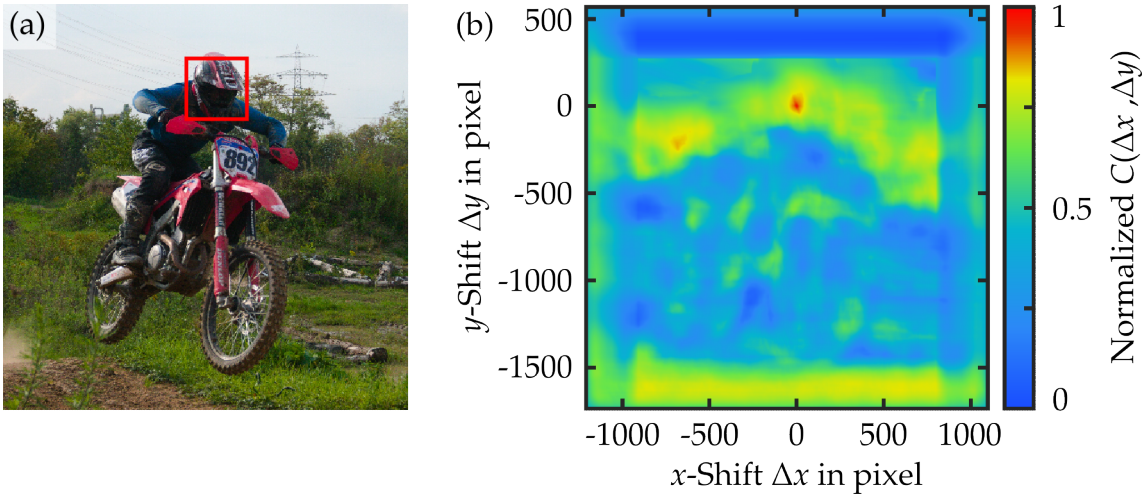

Figure 3.2: Example of a digital-image cross-correlation analysis. (a) A photograph of the author (taken by Alex Vogt) is shown as a base image I_1. The red square outlines the kernel $K(x, y)$ which contains the image feature (helmet) that should be tracked in I_1. (b) False-color plot of the resulting normalized cross-correlation function $C(\Delta x, \Delta y)$. For the computation, both I_1 and K were converted to grayscale images. The maximum of $C(\Delta x, \Delta y) = 1$ occurs for a shift of $\Delta x = \Delta y = 0$, which corresponds to a perfect match between kernel and base image. If the feature moves, the maximum of $C(\Delta x, \Delta y)$ occurs at a nonzero shift, yielding the displacement of the feature.

Therefore, DIC analysis is employed within this work to obtain the in-plane displacement-field components from optical images. A description of the procedure and how to obtain sub-pixelsize displacement information is given below.

3.2.1 *General Principle*

The principle of digital-image cross-correlation analysis is the comparison of two images. Those images are discretized in pixels with coordinates $x = n_x p$ and $y = n_y p$. Thereby, p is the pixel size and n_x,n_y are the integer numbering of the pixels. Commonly, one image I_1 is significantly larger i.e. has a larger number of pixels and is called the base image or in the scope of this thesis, region of interest (ROI). The second image is referred to as the kernel K and has significantly less pixels. The kernel contains the image feature or object that should be located in the base image, or tracked in other images. The metric for comparison of I_1 and K is the two-dimensional (normalized) cross correlation function:

$$C(\Delta x, \Delta y) = \int_{x_1}^{x_2} \int_{y_1}^{y_2} I_1(x, y) K(x + \Delta x, y + \Delta y) \mathrm{d}x \mathrm{d}y \, . \tag{3.6}$$

The integration is calculated over the region covered by K, that is from x_1 to x_2 and y_1 to y_2. $C(\Delta x, \Delta y)$ is a function of the shift $(\Delta x, \Delta y)$ between the kernel and the base image. Figuratively speaking, to compute $C(\Delta x, \Delta y)$ the kernel is shifted pixel-wise across the base image along x and y. For each shift $(\Delta x, \Delta y)$, the images K and I_1 are multiplied and summed up. Doing so yields a larger value of C, the greater the resemblance between the image features of I_1 and K. The result of this method is illustrated in Figure 3.2. Since in this example, K is correlated with the base image I_1, i.e. the image it is cropped out of, the maximum of C occurs for a zero shift at $\Delta x = \Delta y = 0$. If the feature contained in K was to be moved, i.e. a different image I_2 is used to calculate $C(\Delta x, \Delta y)$, the global maximum of $C(\Delta x, \Delta y)$ will occur at a nonzero shift, which is equal to the displacement of the feature.

In Figure 3.2(b), several side-maxima and edge-effects are visible. To minimize any additional extrema of $C(\Delta x, \Delta y)$, it is important to carefully choose the kernel such that a sharp and at best an unique feature with good contrast is included. Otherwise, a clear discrimination between the global maximum and local maxima may not easily be possible and the displacement measurement accuracy will suffer. In the scope of this work, the built-in MATLAB function *normxcorr2* was used to compute $C(\Delta x, \Delta y)$.

3.2.2 *Subpixel Precision with Digital-Image Cross-Correlation Analysis*

As stated above, the value of the shift is an integer of the pixel size. In most optical imaging systems, depending on the magnification, the pixel size may be on the order of the half-wavelength to satisfy the Nyquist-Shannon sampling theorem [68]. This may be to coarse to capture nanometer-scale (and certainly sub-nanometer) displacements. Subpixel accuracy can still be achieved, when investigating a 3×3 region around the global maximum of $C(\Delta x, \Delta y)$. The MATLAB build-in function *findpeak_dic* fits a 2D-parabola to this grid and determines the maximum which may lie at non-integer values of Δx and Δy. This is crucial to achieve the aforementioned resolution of 1/100th of the pixelsize p and to provide sufficient nanometer-scale amplitude resolution to investigate the displacement field of mechanical metamaterials.

Tobias Frenzel and Julian Köpfler have pushed this methodology further in their work, showing that the measurement error on the displacement can be brought down even below one Ångström [67]. To achieve this limit, averaging is needed which presupposes that the displacement field is uniform i.e. constant over a sufficiently large area. This is however not usually the case for the metamaterials studied in this thesis. Nonetheless, DIC analysis forms the backbone to measure the in-plane displacement-field components in this work, since displacement accuracy on the Ångström-scale is not necessary.

3.3 Laser-Doppler Vibrometry

Laser-Doppler vibrometry and anemometry are techniques to sense velocities using the frequency change of light upon reflection from moving objects. The foundation for the technique was provided by the Austrian mathematician Christian Doppler and his work on the color of stars in our universe in 1842 [69]. He discovered that the perceived color of stars changes periodically, and that the pattern of change is linked to a changing relative movement between the observer on earth and the stars in outer space. This observation was made decades before Albert Einstein published his theory of relativity in 1905 [70] which provides the theoretical explanation of the phenomenon nowadays known as the Doppler shift.

Quite some time passed from the discovery of the Doppler-effect to the exploration of laser-Doppler techniques in the laboratory. The field of vibrometry picked up momentum shortly after the advent of coherent radiation emitters, also known as lasers, foremost realized by Maiman in 1960 [71]. First experiments were published on fluid flow-patterns four years later [72] using a helium-neon laser spectrometer, arguably one of the first laser-Doppler anemometers.

To the date of this thesis, laser-Doppler vibrometry has made its way into a multitude of technological and scientific areas. Especially the non-destructive and non-contact measurement capabilities of laser-Doppler Vibrometers (LDV) are widely appreciated. Commercial-grade LDV [73] are used as tools for the calibration of accelerometers [74] medical research [75], and modal analysis in aerospace as well as automotive [76, 77] industries. It is this modal analysis that forms the bridge between industry and the investigation of elastic waves in mechanical metamaterials, which is at the core of this thesis. At this point, a distinction should be made. Previous work by others in the field [78, 79] (to name a few) was mainly concerned with macroscale metamaterials with centimeter-sized dimensions and not on microscale mechanical metamaterials.

In the following text, I summarize the equations for the longitudinal Doppler shift created by a moving mirror and explain the basic operation principle of a LDV. Furthermore, I will derive the equations describing the detector-signal and discuss the resolution of an LDV, which is important for the small displacement amplitudes common for microscale metamaterials. Finally, I describe the digital demodulation scheme used to retrieve the displacement amplitude from the Doppler-signal. A more in-depth discussion can be found in several books on the topic. Here, I will follow the lines of Rembe [80, 81], Castellini [82], Chiarotti [83] and their respective co-authors.

3.3.1 *The Longitudinal Doppler shift from a Moving Mirror*

The simplest case in which a Doppler shift of optical frequencies occurs is depicted in Figure 3.3(a). A receiver detects the optical frequency f_r of optical radiation from a source in constant collinear motion towards the receiver and emitting at f_s. The equation linking the two frequencies is derived from special relativity [70]:

$$f_r = \sqrt{\frac{c-v}{c+v}} \cdot f_s \,, \tag{3.7}$$

where c is the speed of light in vacuum and v the velocity of the source. According to relativity, it is equivalent to consider either the receiver or the source in motion, thus v should be understood as the relative velocity between the two participants.

To arrive at Equation 3.7, a Lorentz transformation from the source frame to the receiver frame of the corresponding electrical fields and laws of reflection is necessary. The mathematical tools for this task can be found in basic work on the topic [84]. Expanding this consideration to laser-Doppler vibrometry means that source and receiver coincide and the reflection on a mirror moving at velocity v_m has to be considered, cf. Figure 3.3(b). The mirror basically is the sample surface under investigation by a LDV. One way to treat this scenario rigorously is to compute two Lorentz-transformations. The first treating the mirror as a receiver when transforming from the source frame into the mirror frame and the second treating the mirror as a source emitting at a Doppler-shifted frequency.

Alternatively, derivations directly from the constant speed of light postulate and basic principles of wave optics are also possible [85]. A third and very illustrative way to look at the problem is to understand the mirror as a plane of symmetry, as it is shown in Figure 3.3(c). This means to think of an image source, the velocity of which v_s' is calculated by the relativistic formula for collinear velocity addition:

$$v_s' = \frac{v_m + v_m}{1 + \frac{v_m \cdot v_m}{c^2}} = \frac{2v_m}{1 + \left(\frac{v_m}{c}\right)^2} \,. \tag{3.8}$$

Inserting v_s' into Equation 3.7 yields the received optical frequency:

$$f_r = \frac{c-v}{c+v} \cdot f_s \,. \tag{3.9}$$

In practical applications of laser-Doppler vibrometry, the velocity of light far exceeds the velocity of the object under investigation, hence the approximation of $v \ll c$ and $(c+v) \approx c$ are valid. Subsequently, the Doppler shift f_D computes from the resulting frequency difference between source and receiver:

$$f_D = f_s - f_r = \frac{2v_m}{c+v_m} \overset{(v_m \ll c)}{\approx} 2f_s \frac{v_m}{c} \,, \tag{3.10}$$

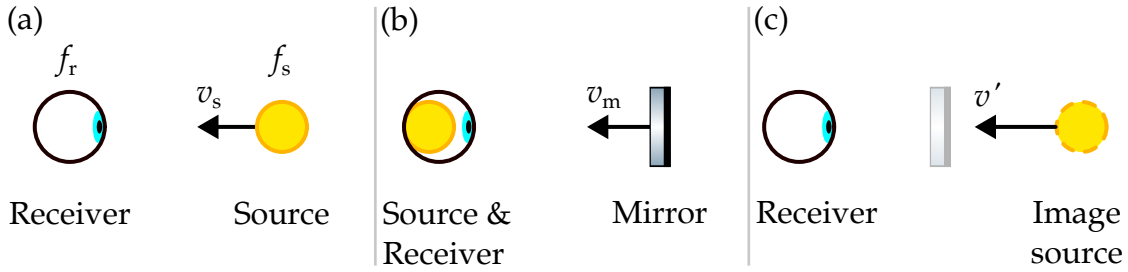

Figure 3.3: Illustration of collinear relative movement between source and receiver. (a) A resting receiver (eye) observes a source (star) moving at velocity v_s and emitting radiation at frequency f_s. The receiver detects the Doppler-shifted frequency f_r. (b) Situation comparable to a laser-Doppler vibrometer. Source and receiver are combined and thus are both at rest. The target is a mirror moving at velocity $v_m = v_s$. (c) Analogy to (b) but a image source moving at velocity $v'_s > v_m$ is considered.

which emphasizes that the shift in optical frequency is directly proportional to the velocity of the object under investigation.

3.3.2 *Working Principle of a single-point Laser-Doppler Vibrometer*

From Equation 3.10 it becomes clear that measuring f_D directly yields information about the velocity of the object under investigation. In practice, wavelengths used in LDV lie in the visible or near infrared regime. Consequently, the optical frequencies amount to several gigahertz, far transcending the accessible range of conventional semiconductor-photodetectors [59]. The solution is provided by interferometric means, that is overlaying the back-reflected laser beam with a second reference beam. Due to the Doppler shift, both beams exhibit a different optical frequency, giving rise to a beating in time of the resulting interference pattern. The frequency of this beating is exactly the frequency of the Doppler shift.

Layout and Components

Either a Michelson-configuration [86] or a Mach-Zehnder-configuration [87, 88] are generally chosen for the layout of the interferometer. These two options are illustrated in Figure 3.4. In both cases, a continuous wave laser with a large coherence length is employed. The laser beam is split into two arms by a beam splitter. The beam of one arm, the sample arm, is directed onto a reflective sample. The back-reflected light is overlayed with the beam in the second arm, the reference arm, onto the senstive area of a photodetector, such as a (avalanche) photodiode. The resulting photodiode current is converted into a voltage by one or more electronic amplifier stages. In practice, several additional lenses, polarizers or waveplates may be necessary to ensure the best possible efficiency of the system

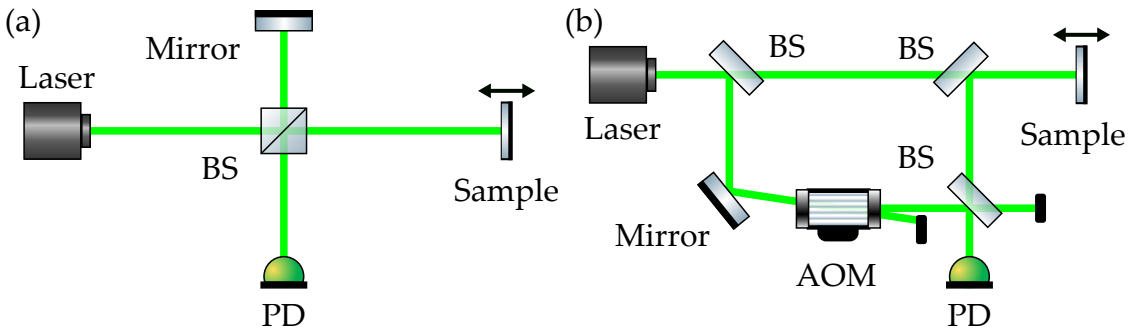

Figure 3.4: Simplified layouts for laser-Doppler vibrometers (LDV). (a) Homodyne LDV in a Michelson interferometer configuration, with a single beam splitter (BS) in the center. The reference arm lies between BS and the mirror at the top. The sample, a moving mirror, is on the right. The intensity created by the overlaying beams is detected by a photodiode (PD) at the bottom. (b) LDV in a Mach-Zehnder configuration. An acousto-optic modulator (AOM) in the reference arm turns the LDV into a heterodyne system.

but are omitted here for clarity.

The experienced reader may already recognize the similarity between the beam path of a Michelson interferometer and a confocal microscope as show in Figure 3.1. Hence at this point, it may seem intuitive to combine the two systems in such a manner. However, for the detection of small displacements and velocities, heterodyning techniques are useful [80]. To do so, one of the laser beams, typically the beam of the reference arm, is shifted in frequency by an acousto-optic modulator (AOM), cf. Figure 3.4(b). In practice, a Mach-Zehnder configuration is arguably easier to align, since no double-pass of the AOM is needed. Therefore, the Mach-Zehnder configuration is most common in commercial devices [83] and is chosen for the experiments in this work. Heterodyning enables for shot-noise limited detection of the optical signal. At the same time, it causes the beating of the intensity at the detector, and thus the detector signal, to be shifted to a higher frequency which has to be considered in the subsequent signal demodulation.

3.3.3 *Detector-signal and Resolution*

To derive the photodiode current $i(t)$ induced by the optical intensity on its sensitive surface, one has to consider the interference pattern generated by the electric fields from the sample arm and the reference arm of the interferometer. The most intuitive approach is to express those fields as plane waves which are solutions to the wave equation in vacuum [89]:

$$\frac{\partial^2 \mathbf{E}}{\partial t^2} = c^2 \frac{\partial^2 \mathbf{E}}{\partial x^2} \,. \tag{3.11}$$

Considering all fields share the same polarization, the vectorial problem turns scalar with the fields in complex notation:

$$E_r(t) = E_{r,0} \cdot \exp\left[i(2\pi f_r t - \varphi_r)\right] \ , \tag{3.12}$$
$$E_s(t) = E_{s,0} \cdot \exp\left[i(2\pi f_s t - \varphi_s)\right] \ . \tag{3.13}$$

Thereby, $E_{r,0}$ is the field amplitude for the reference arm and $E_{s,0}$ is the field amplitude for the sample arm. The optical path length of the two interferometer arms is captured by the phase terms φ_s and φ_r. The optical frequency of the laser radiation is f. For a heterodyne system, as described above, the frequency for the reference arm is shifted by the Bragg-frequency f_B of the AOM i.e.

$$f_r = f + f_B \ .$$

For the beam of the sample arm, the optical frequency is Doppler-shifted according to equation Equation 3.10, thus

$$f_s = f + f_D \ .$$

The total electric field E_{tot} at the detector is the sum of both fields:

$$E_{tot} = E_r(t) + E_s(t) \ , \tag{3.14}$$
$$E_{tot} = E_{r,0} \cdot \exp\left[i(2\pi(f + f_B)t - \varphi_s)\right] + E_{s,0} \cdot \exp\left[i(2\pi(f + f_D)t - \varphi_r)\right] \ . \tag{3.15}$$

The output current of the photodiode is proportional to the absolute square of the total electric field:

$$i(t) \propto |E_{tot}|^2 \ , \tag{3.16}$$
$$\propto E_{r,0}^2 + E_{s,0}^2 + 2E_{r,0}E_{s,0}\cos(2\pi(f_B + f_D)t + \varphi_s - \varphi_r) \ . \tag{3.17}$$

More arithmetic steps can be found in the appendix Section A.2. The key aspect is that the optical frequency f disappears in this expression. As aforementioned, the photodetector cannot follow the optical frequencies directly. Consequently, this also holds true for the sum frequency and the detector acts as a low-pass filter giving rise to a constant (DC) output of $E_{r,0}^2 + E_{s,0}^2$. The latter is either removed by balanced detection using two detectors or alternate-current (AC) coupling of a single detector.

With Equation 3.17, a key benefit of heterodyning becomes apparent. Recalling Equation 3.10, states that the frequency shift is proportional to the velocity v. Since the signal is spectrally centered around f_B, the sign of the Doppler shift encodes the direction of movement which can be extracted as well.

Movement towards observer, $v > 0, \quad f_{\text{Signal}} = f_{\text{B}} + f_{\text{D}}$.

Movement away from observer, $v < 0, \quad f_{\text{Signal}} = f_{\text{B}} - f_{\text{D}}$.

The audible sound of a passing ambulance siren follows the exact same logic, where the frequency of the siren is the equivalent to the carrier frequency of the vibrometer signal. For an approaching ambulance, the pitch of the siren will increase while for a departing ambulance, the pitch will lower.

Detector Signal for a Vibrating Mirror

Strictly speaking, only a mirror or sample moving at a constant speed has been discussed so far. In the typical application of a LDV, the mirror i.e. the sample is vibrating. Therefore, an important modification to Equation 3.17 must be made, which is seldom elaborated in great detail within textbooks. A more general form of the detector current induced by the interference term reads:

$$i(t) \propto 2E_{\text{r},0}E_{\text{s},0}\cos\left(2\pi\int_{t_0}^{t} f_{\text{I}}(t')\,\mathrm{d}t'\right) , \tag{3.18}$$

in which $f_{\text{I}}(t)$ is the instantaneous frequency of the oscillation. Since a trigonometric function evaluates a phase, the integration has to be performed first, in order to get the instantaneous phase φ_{I} at a point in time t. A time-harmonic oscillation at frequency f_{m} can be expressed by:

$$v(t) = v_0 \cdot \cos(2\pi f_{\text{m}} t) . \tag{3.19}$$

Using Equation 3.10, the instantaneous phase (normalized to 2π) is found:

$$\varphi_{\text{I}}/(2\pi) = \int_{t_0}^{t} f_{\text{I}}(t')\,\mathrm{d}t' = \int_{t_0}^{t} \left(f_{\text{B}} + f_{\text{D}}(t')\right)\,\mathrm{d}t' \tag{3.20}$$

$$= \int_{t_0}^{t} \left(f_{\text{B}} + 2\frac{f}{c}v(t')\right)\,\mathrm{d}t' = \int_{t_0}^{t} \left(f_{\text{B}} + 2\frac{f}{c}v_0 \cdot \cos(2\pi f_{\text{m}} t')\right)\,\mathrm{d}t' , \tag{3.21}$$

$$= f_{\text{B}} \cdot (t - t_0) + 2\frac{f}{c} \cdot \frac{v_0}{2\pi f_{\text{m}}} \cdot (\sin(2\pi f_{\text{m}} t) - \sin(2\pi f_{\text{m}} t_0)) . \tag{3.22}$$

This equation can be simplified when introducing the laser wavelength $\lambda = c/f$, and recalling that the spatial amplitude s_0 is linked to velocity amplitude with

$v_0 = s_0 \cdot 2\pi f_\mathrm{m}$. Additionally, absorbing constant terms (not dependant on t) into φ_0 yields:

$$\varphi_\mathrm{I}/(2\pi) = f_\mathrm{B} \cdot t + \frac{2s_0}{\lambda} \cdot \sin(2\pi f_\mathrm{m} t) + \varphi_0/(2\pi) \; . \tag{3.23}$$

Finally, the detector signal for a vibrating sample follows:

$$i(t) \propto 2E_{\mathrm{r},0}E_{\mathrm{s},0} \cdot \cos\left(2\pi f_\mathrm{B} t + \frac{4\pi s_0}{\lambda} \cdot \sin(2\pi f_\mathrm{m} t) + \varphi_0\right) \; . \tag{3.24}$$

A convenient observation here is to notice that the phase of the $i(t)$-oscillation is directly linked to the displacement of the sample. Therefore, phase-demodulation (PM) techniques can directly provide the information about the movement of the sample along the direction of the laser beam.

Furthermore, the frequency spectrum of such signal can be expressed in Bessel functions of the first kind and first order, when using the Jacobi-Anger expansion [90]. What follows is, a central peak at the Bragg- i.e. carrier frequency f_B with several side-lobes, the number and magnitudes of which depend on the modulation parameters v_0, or s_0 and f_m. An example of a simulated signal $u(t)$ and its spectrum are shown in Figure 3.5. It is possible to link the displacement-resolution limit of the vibrometer to the number of detectable side-lobes.

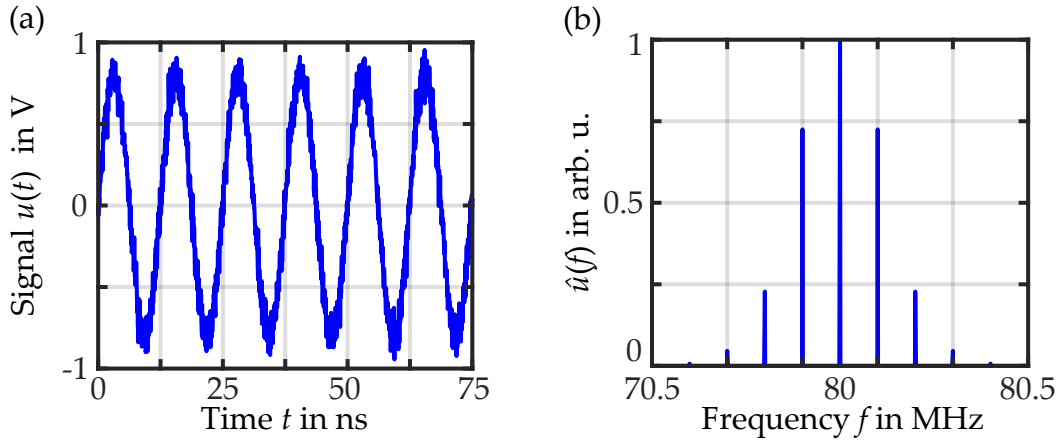

Figure 3.5: Simulated signal for a heterodyne LDV. (a) Amplified voltage signal $u(t)$ at carrier frequency $f_\mathrm{B} = 80\,\mathrm{MHz}$ detected by a photodetector. The sample is oscillating at $f_\mathrm{m} = 100\,\mathrm{kHz}$ and a displacement amplitude of 50 nm. (b) Spectrum obtained through Fourier transformation of $u(t)$, showing side-lobes with the central peak at the carrier frequency f_B. The spacing of the lobes is equal to the modulation frequency f_m.

Resolution limit

The displacement information of the sample is encoded in the instantaneous phase of the detector signal. To deduce the amplitude resolution limit of a LDV, the occurring noise sources on that signal have to be compared. In general, there is thermal (Johnson) noise, quantization noise in the digitization of the signal and optical shot noise [81]. The latter poses the fundamental physical limit due to the quantum nature of light. A peculiarity of a heterodyne system is that shot-noise limited acquisition can be achieved relatively straight forward. This becomes clear when comparing the scaling of the noise sources with power. The exception to this is quantization noise, which can be minimized by using the full range of the subsequent analog-digital converter. As it is common, noise budget discussions are performed in terms of power, which is why mean-squared quantities over the time constant of the photodetector are considered.

For thermal noise of a detector with load resistor R, the mean-square noise contribution to the detector signal computes to:

$$\overline{i_{\mathrm{th}}^2} = \frac{4k_{\mathrm{B}} \cdot T \cdot B}{R} \,, \tag{3.25}$$

with Boltzmann's constant k_{B}, temperature T and detector bandwidth B. Notably, this quantity is independent of the signal power, i.e. the electric field amplitudes. The mean-square shot noise current of the detector is given according to [81] by

$$\overline{i_{\mathrm{sh}}^2} = 2 \cdot K \cdot q \cdot B \cdot (P_{\mathrm{s}} + P_{\mathrm{r}}) \,. \tag{3.26}$$

In this equation $K = \eta q / hf$ is the sensitivity of the photodiode, h is Planck's constant, η the quantum efficiency and q the elemental charge. The electric fields at the detector have furthermore been converted into signal powers over the sensitive detector area with using the vacuum impedance $Z_0 = \sqrt{\mu_0/\varepsilon_0}$. With

$$\varphi_{\mathrm{sig}}(t) = 2\pi f_{\mathrm{B}} \cdot t + \frac{4\pi s_0}{\lambda} \cdot \sin(2\pi f_{\mathrm{m}} t) + \varphi_0 \,, \tag{3.27}$$

the complete detector current with AC and DC component can be rewritten as:

$$i(t) = K \cdot \left(P_{\mathrm{r}} + P_{\mathrm{s}} + 2\kappa \sqrt{P_{\mathrm{r}} P_{\mathrm{s}}} \cdot \sin\left(\varphi_{\mathrm{sig}}(t)\right) \right) \,, \tag{3.28}$$

where κ is the heterodyning efficiency which lies between 0 and 1 to accommodate for aberrations or residual misalignment in the system. The only two quantities scaling with the optical powers P are the shot noise and the signal itself. Calculating the signal-to-noise (SNR) ratio of Equation 3.26 and Equation 3.28 yields:

$$\mathrm{SNR} = \overline{i^2} \,/\, \overline{i_{\mathrm{sh}}^2} = \frac{\eta \cdot \kappa^2 \cdot P_{\mathrm{r}} \cdot P_{\mathrm{s}}}{h \cdot f \cdot B \cdot (P_{\mathrm{r}} + P_{\mathrm{s}})}. \tag{3.29}$$

Several important conclusions can be drawn from this. Both the signal power and the shot-noise power depend linearly on P_R. When increasing the reference beam power such that $P_r \gg P_s$, Equation 3.29, will reduce to:

$$\text{SNR} \propto \frac{P_s \cdot P_r}{P_s + P_r} \quad \rightarrow \quad SNR \propto P_s \, . \tag{3.30}$$

Consequently, the SNR becomes independent of the reference beam power P_r and no increase in SNR can be achieved for larger P_r. However, the SNR will lay well above any thermal noise contributions, creating a shot-noise limited system [81].

At this point, a consideration about the influence of quantization noise should be made. Usually, the photocurrent is converted into a voltage signal using one or more transimpedance amplifiers with feedback resistance R_{TIA}. Let's consider that this voltage signal is directly digitized by an analog-digital-converter (ADC) with full scale input range U_r. For ideal performance, it is wise to chose R_{TIA} so the amplified signal matches the ADC input range, hence $U_r = 4R_{TIA}K\kappa\sqrt{P_s P_r}$. The quantization noise on that signal for an ADC with n_b bits and a sampling rate f_{ADC} following [83] is:

$$\overline{u_{qn}^2} = \frac{1}{12}\left(\frac{U_r}{2^{n_b-1}}\right)^2 \frac{2B}{f_{ADC}} = \frac{4(R_{TIA} \cdot K \cdot \kappa)^2 \cdot P_s P_r}{3 \cdot 2^{2n_b-1}} \frac{2B}{f_{ADC}} \, . \tag{3.31}$$

To maintain shot-noise limited acquisition, a high enough sampling rate and number of bits have to be chosen. In other words, when calculating a SNR_{qn} from Equation 3.28 and Equation 3.31, the value of SNR_{qn} should always exceed the SNR calculated with Equation 3.29.

In closing, it is crucial to understand that the limiting factor on the SNR is the reflectivity of the sample under investigation

$$SNR \propto P_s = P_0 \cdot r^2,$$

with P_0 as laser power emitted into the sample arm and r as the Fresnel coefficient of reflection [61] of the sample. This explains why in the application, surfaces that offer a high back-scattering of the optical radiation are preferred or intentionally generated with the use of reflective tape, such that $r \approx 1$. In the case of mechanical metamaterials, fabricated with a polymer constituent, the reflectivity is much lower. The commercial photoresist IP-S (Nanoscribe) has a refractive index of ≈ 1.5 [91]. Hence, the reflectivity is on the order of only 4 % for perpendicular incidence of the laser beam on the air-polymer interface. This detriment of small r carries over to the discussion of the smallest displacement-amplitude a LDV can detect.

Revisiting the spectrum of a Doppler-signal in Figure 3.5(b), for extremely small displacements on the order of a fraction of the laser wavelength, the amplitude of the side-lobes reduces. While in theory there is an infinite number of side-lobes, in practice the detection limit lies at the point where the closest side-lobes to the central peak are equal to the noise floor of the system. Thereby, only the central peak with amplitude J_0 centered at f_B and the first pair of side-lobes with amplitudes J_1 centered at $f_B \pm f_m$ are present. A good approximation is made with $J_0 = 1$ and $J_1 = 0.5\Delta\varphi$ [81]. This condition corresponds to setting SNR $= 1/\sqrt{2}$ in Equation 3.29, since two side-lobes with uncorrelated noise contribute. For phase modulated signals, it can be shown that the phase noise $\Delta\varphi$ of the Doppler-signal relates to the SNR for small displacements of the sample as:

$$\Delta\varphi = \frac{4\pi}{\lambda} \cdot \Delta s \approx \frac{2}{\sqrt{\mathrm{SNR}}} \,. \tag{3.32}$$

Solving for Δs yields the smallest detectable displacement amplitude. It is common practice to normalize this Δs_{min} over the square-root of the detection bandwidth B. This eases the comparison between different LDV. Using common parameters for a LDV with $\lambda = 633\,\mathrm{nm}$, $\eta = 0.8$, $\kappa = 0.8$, $P_R = 1\,\mathrm{mW}$, $P_S = 0.1\,\mathrm{mW}$ a displacement per square-root bandwidth of

$$\Delta s' = 4.024 \cdot 10^{-15}\,\mathrm{m}/\sqrt{\mathrm{Hz}}$$

can be measured. For a detector with a bandwidth $B = 100\,\mathrm{MHz}$, a displacement resolution of $\Delta s_{\mathrm{min}} = 40\,\mathrm{pm}$ is viable in theory. However, the consideration so far does not attribute further electronic noise sources such as electronic cross talk and spurious noise peaks, as well as the already mentioned low reflectivity of the metamaterial samples. The latter has the most dramatic influence and may deteriorate the resolution to $\Delta s_{\mathrm{min}} = 0.2\,\mathrm{nm}$. Countermeasures are either averaging the signal when observing time-periodic processes, or limitation of the detection bandwidth. Nonetheless, the sub-nanometer displacement resolution is comparable with the resolution provided by DIC. Consequently, an LDV is a adequate tool, to extract the out-of-plane displacement and as such can complete the 3D displacement-field measurement on mechanical metamaterials.

3.3.4 Signal Demodulation

As mentioned before, the detector current is usually converted into a voltage by a transimpedance amplifier. From Equation 3.28 follows:

$$u(t) = R_{\mathrm{TIA}} \cdot i(t) \,. \tag{3.33}$$

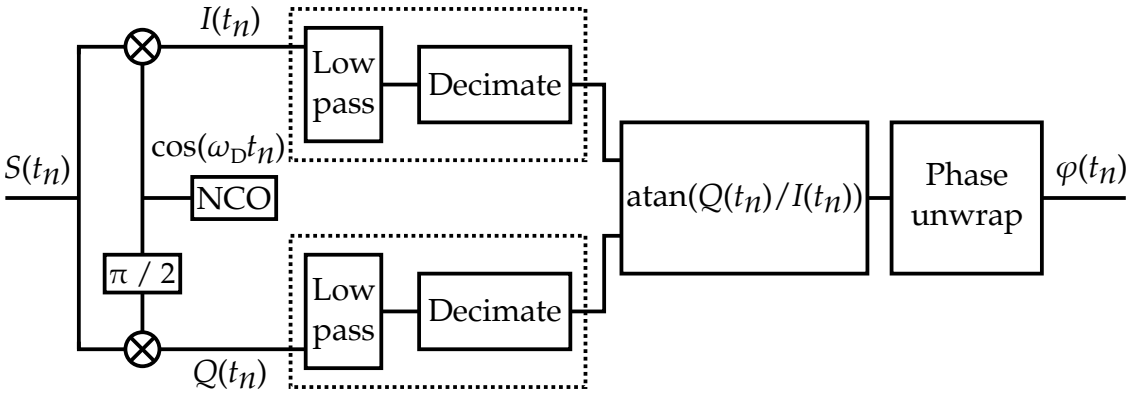

Figure 3.6: Block diagram of an in-phase and quadrature (IQ) demodulator for a digitized Doppler-signal $S(t_n)$ at sample points t_n. The signal mixers are drawn as circles with crosses. A local oscillator (LO) provides the reference for demodulation with angular frequency $\omega_D = 2\pi f_D$. The low-pass and data decimation stages are enclosed by dashed boxes. The output of the demodulator is the phase $\varphi(t_n)$ which can be converted into a displacement by the factor $\lambda/(4\pi)$. Figure from supporting material of [92] and adapted under (CC BY 4.0)

It is the phase of this this voltage signal $u(t)$ that encodes the displacement information of the sample. This retrieval process is called decoding or demodulation. Historically in the 20th century, analog demodulation schemes with phase-lock-loops or lock-in techniques were used [93]. These analog demodulators offer the largest velocity ranges and fastest DC response. A downside to analog technology is the susceptibility to device degradation, thermal drifting and nonlinearities. Digital demodulation schemes do not suffer from this issue and offer a flexible way to integrate sophisticated data processing and filtering. To the date of this thesis, digital demodulation is the new standard for LDV [81]. A common type of digital demodulation is the digital counterpart to a lock-in amplifier and also known as in-phase quadrature (IQ) demodulation. The block diagram of this procedure is printed in Figure 3.6. The continuous analog voltage signal $u(t)$ is digitized by an ADC with sample rate f_{sam} and converted into the discrete time-series $S(t_n)$ at sample time points t_n. Moving through the block-diagramm, the time series is multiplied with a numerically generated sine and a cosine (NCO), the frequency of which is chosen to match the carrier- i.e. Bragg-frequency of the AOM.[2]

From this point on, two signals are considered, the in-phase $I(t_n)$ and the quadrature $Q(t_n)$ component. The mixing generates sum and difference frequencies. Since the signal features the same center frequency as the sine and cosine used for mixing, the signal is down-converted into the baseband for $f_D - f_D = 0$.

[2] In analog technology, the sine and cosine are provided by a local oscillator (LO) and a $\pi/2$ phase shifter. For digital demodulation, the representation can be calculated in advance.

Additionally, a higher harmonic with $2f_D$ will arise numerically. The mathematics look somewhat similar to the mixing of two electric fields from Equation 3.17 or appendix Section A.2. The high frequency components are subsequently removed from I and Q by low-pass filtering and data-decimation. Specifically for this process, moving average filters are applied to I and Q. For a moving average window of N sample points, only every N-th data point carries new information. The other data points can be decimated, conveniently reducing the data size at the same time. This process is also known as digital down conversion (DDC). The phase of the signal $S(t_n)$ is finally recovered by computing the arctangent (atan, cf. Figure 3.6) of I and Q. A peculiarity to digital demodulation is that the underlying phase of the carrier signal, onto which the displacement information is encoded, is not known right away. Depending on the instantaneous phase difference between NCO and signal for $t_0 = 0$, the amplitude of Q and I will vary. Therefore, phase unwrapping is needed to reconstruct the correct signal phase:

$$\varphi(t_n) = \arctan \frac{Q(t_n)}{I(t_n)} + m\pi, \quad \text{with} \quad m = 0, 1, 2, 3, \ ... \tag{3.34}$$

This step eliminates the original amplitude of the signal $u(t)$ or $S(t_n)$ in which lies major benefit of the phase (or frequency) modulating properties of laser-Doppler vibrometry. The procedure is sensitive to phase (or frequency) and not to a absolute amplitude. The displacement data is finally obtained by rescaling $\varphi(t_n)$:

$$s(t_n) = \frac{\lambda}{4\pi}\varphi(t_n) \ . \tag{3.35}$$

For the sake of integrity, a possible artefact should be mentioned. After the signal demodulation, it may be possible that the displacement raw data shows a drift with a constant velocity. The cause of this artefact is a small mismatch between the AOM frequency f_B and the assumed 80 MHz of ≈ 100 Hz, thus on the order of 1.25 ppm only. The drift can be removed by least-square fitting a linear slope to the data and subtracting the result. As aforementioned, the cause of this artefact lies in the unmeasured frequency of the AOM. If the AOM frequency and phase were known exactly, the NCO could be set accordingly and both the phase-unwrapping as well as the drift-subtraction are unnecessary. However, measuring the AOM frequency is not always possible[3] (for some devices) or at least occupies another channel of the data acquisition unit which adds complexity to the system. Anyways, the artefact can be compensated for as mentioned by numerical means.

[3] Some commercial AOM drivers simply don't offer a built-in frequency readout and would require custom modifications.

Summary

A LDV measures the displacement component parallel to the laser beam of a moving surface. Commercial LDV are build in a Mach-Zehnder layout. Heterodyning is used, to lift the sign ambiguity of the surface (sample) velocity. Thereby, the direction of movement relative to the incident beam is extracted. The displacement-extraction from the acquired Doppler-signal is most commonly performed in the digital domain using an IQ demodulation technique. For sufficiently large optical powers, shot-noise limited reception can be achieved. However, the displacement resolution of the LDV depends on the amount of back-scattered light from the sample surface. For metamaterial surfaces with a reflectivity of 4 %, sub-nanometer resolution is possible which is on par with DIC analysis. Conclusively, a LDV is a suitable device to track elastic waves in mechanical metamaterials.

Chapter 4

4 Setup for Time-Resolved Tracking of Elastic Waves

I dedicate this Chapter to the description and demonstration of the self-built experimental setup I realized during this thesis, in order to perform experiments on mechanical metamaterials. The core functionality of the setup is the time-resolved three-dimensional measurement of the displacement vector at a local position. Automation of the measurement procedure allows to track elastic waves along metamaterial samples by sampling their displacement-vector field at multiple, deliberately chosen regions of interest. Therefore, the setup features a confocal-microscopy branch and a laser-Doppler-vibrometry branch. I will start the description by addressing the confocal-microscopy branch first, and what has to be heeded when applying digital-image cross-correlation analysis to images acquired with a sectioning imaging system. Subsequently, I report the addition of the laser-Doppler-vibrometry branch and describe the necessity of calibration for vibrometers integrated into microscopes. The Chapter closes with a demonstration of displacement-measurement performance in three dimensions.

4.1 The Confocal Microscopy Setup

The section begins with a detailed description of the setup layout and components of the confocal-microscopy branch. Historically, this is the configuration in which the setup was first used to perform experiments on metamaterial samples. Considering the imaging, the arguably full-fledged name for the setup in this state is a confocal optical laser-scanning back-scattering microscope. The assembly and programming of the microscope was performed in cooperation with my former student Jannis Weinacker during his masters thesis, whose contribution I want to acknowledge at this point. A description of the setup has been published before by myself and co-authors in the supporting information of [94], and will follow those lines. Additionally, the implemented imaging i.e. measurement modes are listed afterwards, and the calibration of the field of view is reported. Subsequently, the influence of optical sectioning on displacement data recovered by digital-image cross-correlation (DIC) analysis is discussed quantitatively.

4.1.1 Design of the optical beam path

The beam path for the setup was designed and modeled in Matlab using Gaussian beam propagation. Additionally, the design was cross-checked with ray-tracing simulations performed in Zemax OpticStudio. The resulting schematic of the beam path and components of the confocal back-scattering microscope is depicted in Figure 4.1. A detailed component table is provided in Appendix B, which lists the corresponding component models and manufacturers. For the illumination of the sample, a highly stable, air-fan cooled single-longitudinal mode, frequency doubled diode-pumped solid-state laser with emission wavelength of 532.3 nm is used. To maintain the stability of the laser emission, a Faraday isolator is positioned in front of the laser to block back-reflections, which are inevitable in any confocal microscopy setup. The laser is emitting linearly polarized light at 200 mW, which is the most stable operation point according to the manufacturer. To reduce the laser power externally, a half-wave plate (R1) and a polarizing beam splitter cube (PBS) are used. A second half-wave plate (R2) allows to rotate the laser beam polarization if required. A clean-up filter for the laser emission wavelength blocks any potential background laser emission (e.g. at 1064 nm).

The beam path is separated into the illumination path and the detection path (cf. confocal principle Figure 3.1) by a thin-film beam splitter (TFBS). Per design, the laser is emitting a beam with Gaussian beam diameter of 0.7 mm. In order to illuminate the back aperture of the objective lens (OL) with diameter 4.8 mm, and to compensate the divergence of the laser beam, three $4f$ telescopes (TEL1-TEL3) are used between the laser and the galvanometric scanner.

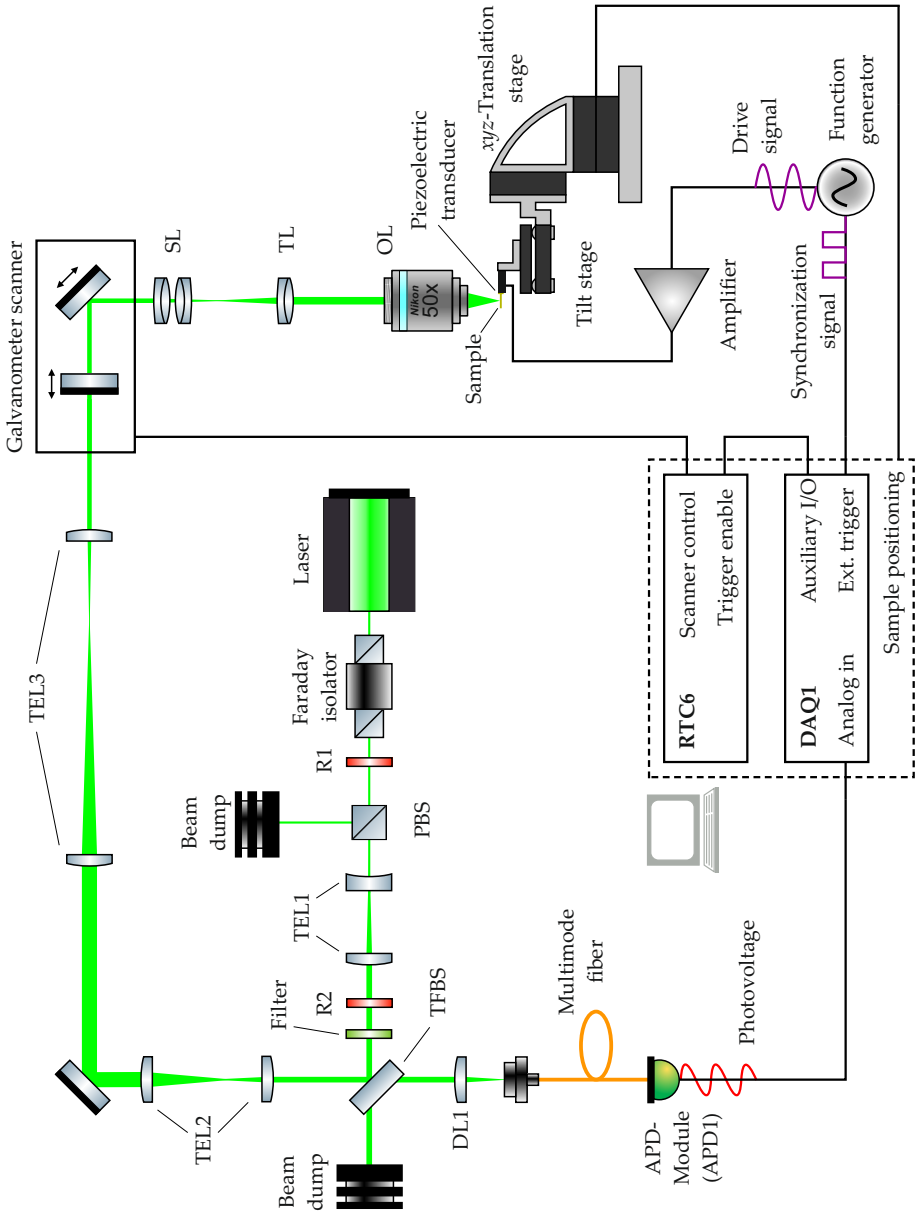

Figure 4.1: Schematic of the confocal optical back-scattering microscopy setup. The beam path of the laser radiation is tinted green. Telescopic lens-pairs are labeled (TEL1-TEL3). Polarizing beam splitter cube (PBS), and thin film beam splitter (TFBS). Half-wave retarder plates (R1,R2). Scan lens(SL), tube lens (TL), and objective lens (OL). Detection lens (DL1). Personal computer (PC) components are enclosed in the dashed box: data acquisition unit (DAQ1), galanometer scanner control card (RTC6). Electrical wiring is sketched as black lines. The detailed description is given in the text. Figure and caption taken from [94] and adapted under (CC BY 4.0), published by Science Advances 2021.

TEL1 forms a compact Galilei telescope with $f_1 = -75\,\text{mm}$ and $f_2 = 200\,\text{mm}$. TEL2 is a Keppler telescope with $f_3 = 75\,\text{mm}$ and $f_4 = 200\,\text{mm}$, as well as TEL3 with $f_5 = 300\,\text{mm}$ and $f_6 = 175\,\text{mm}$.

The scan lens (SL) of the setup is comprised of two achromatic lenses with respective focal lengths of 250 mm. Arrangement in a Plössl-configuration, following the suggestions made in [95], yields an effective focal length of $f_{\text{SL}} = 125\,\text{mm}$. The focal point of the SL is chosen to lie exactly in between the two mirrors of the galvanometric scanner. This minimizes wobble[1] of the laser beam when scanning, since the mirrors are not imaged onto each other. Lastly, the tube lens (TL) is an achromatic lens with $f_{\text{TL}} = 200\,\text{mm}$. The telescopes, the scan lens and the tube lens magnify the beam diameter from 0.7 mm to 4.6 mm. The residual under-illumination of the OL back-aperture is accepted to account for the aforementioned beam wobble.

The back-scattered light from the sample is propagating backwards along the illumination path and enters the detection path at the TFBS. The light is collected by an achromatic lens of $f = 40\,\text{mm}$. The achromat forms the detection lens (DL1) and focuses the light onto a multimode fiber with 200 µm core diameter, acting as the pinhole. To the experienced user of a confocal microscope, this may seem relatively large - and rightfully so. The reason for this relatively large pinhole of about 10 AU (cf. Equation 3.1) is elaborated in Section 4.1.3.

The choice of optics results in a total magnification of $M = 24.9$. The multimode fiber is coupled to an avalanche photodiode module (APD1), which provides an output photovoltage singal, the magnitude of which is proportional to the incident light intensity. This photovoltage signal is measured by the data acquistion unit (DAQ1), which is an peripheral component interconnect express (PCIe) card within the personal computer (PC).

Scanning of the laser beam is performed by the galvanometric scanner. The latter is controlled by a real-time controller (RTC6), also installed within the PC as an PCIe card. The RTC6 card provides a trigger to the auxiliary I/O of DAQ1 and thus performs the position measurement of the image pixels.

In order to align the sample surface parallel to the image plane of the objective lens[2] a three axis manual tilt-stage is provided. The tilt-stage is mounted to a three axis xyz-translation stage. The latter is assembled out of three linear stages with piezo-inertia drives. These linear stages have a travel range of 13 mm, which is required since the metamaterial samples, for which the setup is intended, exceed the optical field of view.

[1] The wobble is a shift of the beam which depends on the angle of deflection by the galvanometric mirrors, when they are not imaged onto each other.

[2] A detail whose importance will be stressed in Section 4.1.3.

The excitation of elastic waves is realized by a piezoelectric transducer that is driven with a time-harmonic amplified voltage (drive signal). The drive signal is synthesized by a function generator and an amplifier. The function generator also provides a synchronization signal, whose relevance will be made clear in the Section 4.3 on the excitation and tracking of elastic waves.

4.1.2 *Imaging Modes and Field of View Calibration*

The scanning of the laser beam is implemented with a off-the-shelf galvanometric-mirror scan system. The system consists of the scan head (IntelliScan 10, Scanlab) and a digital position encoder realized in the real-time controller (RTC6, Scanlab) card. Scanning is performed by supplying a coordinate list for the laser focus to the RTC6 card and executing the list by software control. For this thesis, three different imaging modes were implemented.

The scan system is originally intended for material processing and used with off-the-shelf scan objective lenses. If different, or in this case home-built, scan optics are used, a calibration of the field of view is required to determine correct absolute displacement measurements. Especially when comparing in-plane displacement data from images with out-of-plane displacement data obtained via laser-Doppler vibrometry, calibration is indispensable.

Imaging Modes

The microscope is programmed as such that the user provides a number of pixels n_p in one direction and a intended pixel size p. The software generates a coordinate list for the scanning of the laser beam and calculates the largest possible scan speed for the laser focus.

FAST MODE provides the quickest way to obtain images. A linewise or column-wise scanning is available. Once the RTC6 card verifies that the laser focus has reached the beginning of a line (or column), a trigger signal is send to the DAQ1. Thereby, movement of the laser focus along a line (or column) and acquisition of a photovoltage time-series by DAQ1 start simultaneously. The scan speed for the laser focus in this imaging mode is calculated considering the sample rate f_ADC of DAQ1. The scan speed is set such that the time difference $1/f_\mathrm{ADC}$ between data points of the time-series results in a sample-point spacing of the pixel size p. Once all n_p lines (or columns) are measured, the image is assembled. This fast mode is useful when overview images are required, for example during sample manipulation with the xyz-translation stage.

SLOW MODE is a pixelwise mode. Each pixel of the image is addressed individually. Once the RTC6 card verifies that the laser focus is at the designated pixel coordinates, a trigger is sent to DAQ1 and time-series of the photovoltage is acquired for that pixel. This enables pixel-wise averaging of the photovoltage. Once all $n_p \times n_p$ pixels are measured, the image is assembled. This mode is significantly slower than the fast mode[3]. However, it provides the highest accuracy the scan system can provide for the laser focus and thus the position measurement of the pixels (data sheet of intelliSCAN se 10, [96]). Images acquired with this mode are ideal for subsequent DIC analysis.

DYNAMIC MODE is the mode for the time-resolved elastic-wave tracking. It resembles the slow mode. The important distinction is the triggering of the data acquisition. The latter is synchronised to the drive signal of the piezoelectric transducer. The mode and the data structure are explained in more detail in Section 4.3.

Field Of View Calibration

The encoder of the RTC6 card has a 20-bit resolution for the angle of the mirrors which translates into a defined position-resolution in the focal plane of a corresponding off-the-shelf scan-objective lens. However for this work, self-build scan optics and a microscopy objective lens are used. To achieve accurate absolute length and displacement measurements, a calibration of the field of view is necessary, since the effective focal length of the scan lens[4] is only estimated by the inverse sum of it's two constituent achromatic lenses. Technically, if only relative lengths are of interest, this procedure can be neglected. As aforementioned, a meaningful comparison between in-plane and out-of-plane displacements, which are measured using vastly different techniques, is only possible when the field of view is calibrated. Naturally, if different objective lenses that are designed for different tube lenses are used, a calibration is advisable as well as long as the correct tube lens focal width isn't known. As mentioned above, the digital encoder divides the field of view by 20 bits i.e. 2^{20} bit-levels along each image axis. The goal of the calibration is to determine how many bit levels correspond to the width of a pixel p. To obtain this conversion factor, a commercially available USAF 1951 resolution test target (R1DS1N, Thorlabs) is used. For the calibration, images using the slow mode with $p = 500\,\text{nm}$ of group 6, elements 4 and 3 are acquired. These distance of the line-pairs, depicted in Figure 4.2, are measured using the open source software ImageJ or Fiji. Comparing the measured line pairs per millimeter with the listed values for the imaged elements determines the correct conversion

[3] Depending on the chosen number of pixels, the slow mode may be more than ten times slower.
[4] The scan lens is comprised of two achromatic lenses in Plössl configuration.

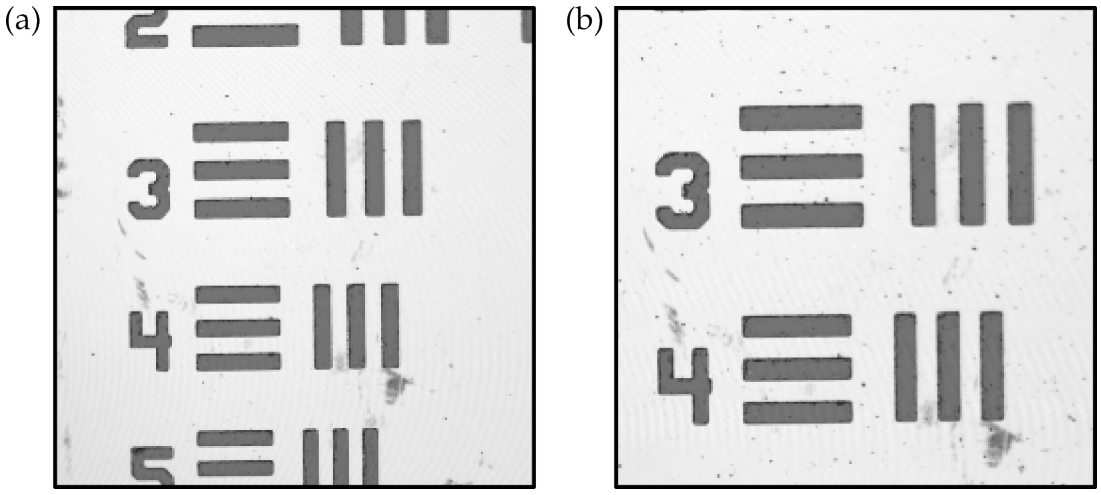

Figure 4.2: Line pairs of group 6, elements 4 and 3 of USAF 1951 resolution test target acquired with the slow mode. For element 4 of group 6, the number of line pairs per millimeter is 80.6 mm^{-1}. Image (a) before calibration and (b) after calibration for a Wetzlar PLAN L 50x/0.6 objective lens. Both images are acquired with an intended pixelsize of $p = 500\,\mathrm{nm}$ and a field of view of 120 µm. For (a), the calibration factor is too large, resulting in a wider than intended area scanned by the laser beam.

of length to number of bit-levels. For the originally used objective lens (50x CFI60 TU Plan Epi ELWD, Nikon), the conversion is 1 µm $\longleftrightarrow$ 600 bit-levels.

For a different objective lens (PLAN L 50x/0.6, Wetzlar), which is used after the addition of the vibrometry branch, a different conversion of 1 µm $\longleftrightarrow$ 460 bit-levels must be used. The Wetzlar objective lens is designed for a tube lens of different focal length, compared to the Nikon objective lens, hence the difference. The conversion for several objective lenses is supplemented in tabular form within Appendix B.

4.1.3 Peculiarity of DIC analysis on confocal image data

When applying DIC analysis to images acquired with an optical sectioning technique, care must be taken when interpreting the in-plane (x, y) displacement data. The optical sectioning of the confocal microscope together with DIC analysis can cause a out-of-plane (z) displacement of the object under investigation to be mistaken for an in-plane displacement, leading to false displacement measurements. This artefact is discussed in the following text since it places a limitation on the pinhole diameter d_{Ph}, as well as the choice of a ROI and kernel for DIC. Additionally, a quantitative theoretical analysis is presented.

DIC analysis operates on 2D images and is sensitive to contrast, i.e. the difference in value of neighbouring pixels. Albeit, the technique is oblivious to how this contrast is created or changed, for example with time in an image series when tracking a moving object. Using images acquired with optical wide-field imaging techniques, and for simplicity assuming a rigid object under investigation that only shows translations and no deformations within the region of interest, DIC analysis can be used to track the movement of the object within the image plane. Displacing the sample out of focus along the optical z-axis, will cause the images to become blurred, if no telecentric imaging is applied. The blurring may increase the noise level of the DIC analysis but is not expected to introduce artificial displacements within the image plane. Obviously, this will depend to some extend on the object size and shape as well as the magnitude of the displacement. However, for most practical purposes such as the investigation of metamaterials done by J. Köpfler and T. Frenzel, this held true.

When using optical images acquired with a confocal back-scattering microscope, one has to take additional care when tracking tilted surfaces or sample features. An experienced user may recall that when acquiring a z-stack of images from a tilted surface in a confocal microscope, one can observe a bright fringe passing through the image plane. This is a direct consequence of the optical sectioning in which light that is back-scattered within the focal plane is focused directly onto the detector while light back-scattered from higher or lower planes is diminished. It is exactly this movement of the fringe that may be picked-up by DIC analysis and misinterpreted as a lateral movement, even though no displacement in the lateral direction occured at all. In order to grasp the severity of this artefact, intensity patterns (showing such a fringe) generated from a tilted plane for several shifts Δz along the optical axis are investigated. Due to the tilt, the intensity pattern show exactly such a fringe which is moving as a function of Δz.

Rigorously, the movement of the fringe has to be calculated by computing the convolution of the microscopes point-spread function [62] (PSF) with the height profile of a tilted plane for different axial displacements Δz. For this consideration, the process can be simplified significantly. A suitable substitute for the PSF along the axial direction is to investigate the signal response when scanning a glass-air interface through the object lens focal plane [97]. This response is depicted in Figure 4.3 for two different pinhole diameters.

The intensity patterns of a tilted plane for different Δz can now directly be calculated using a fit to the data shown in Figure 4.3 instead of using a convolution. The height profile of the tilted plane is simply converted point-wise[5] into a intensity using the fit result.

[5] Conversion is performed point-wise for each pixel of the image.

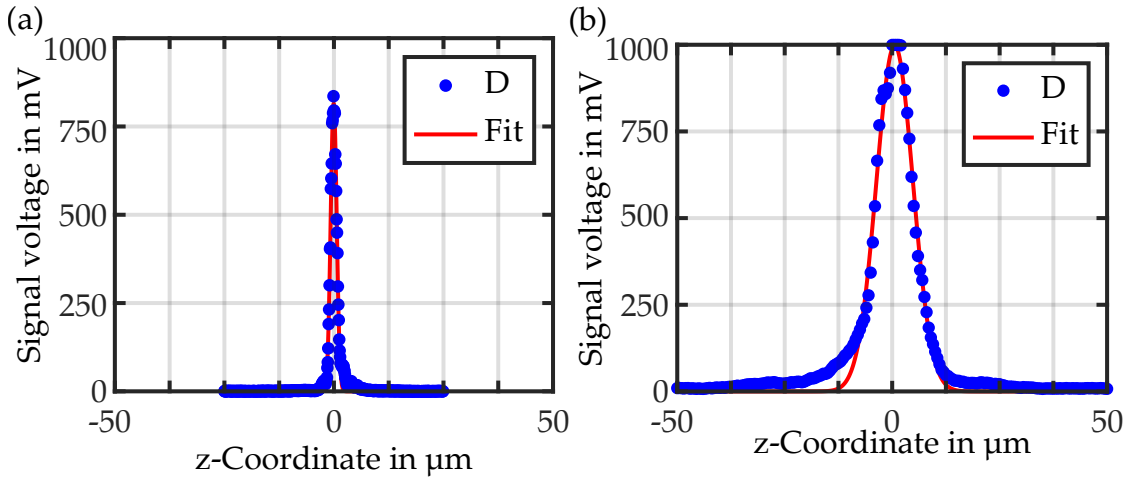

Figure 4.3: (a) Measured signal response when scanning a glass-air interface axially through the focal plane of the objective lens. A Gaussian fit (red) was performed on the data points D (blue). The pinhole (fiber core) diameter used in the microscope was $d_{\mathrm{Ph}} = 20\,\mu\mathrm{m} \approx 1\mathrm{AU}$). The full width at half maximum computes to about FWHM $\approx 2\,\mu\mathrm{m}$. (b) Equivalent to (a) but for a ten times larger pinhole diameter of $d_{\mathrm{Ph}} = 200\,\mu\mathrm{m}$, resulting in FWHM $\approx 10\,\mu\mathrm{m}$.

Three computer generated example images i.e. intensity distributions for three different axial displacements are shown in Figure 4.4, using the axial response from Figure 4.3(a). DIC analysis of those images with a kernel taken from the image center of one of the three images will result in a displacement along the x-axis, even though the plane was not moved along this direction at all. Therefore, the otherwise beneficial properties of the optical sectioning can introduce severe artifacts in the displacement determination using DIC analysis.

However, in Figure 4.4, the axial displacement as well as the tilt angle ϕ were exaggerated for illustration purposes. An axial displacement comparable to the FWHM of the axial response depicted in Figure 4.3(a) was chosen. In the experiments conducted in this work, the magnitude of the displacement-vector field of a metamaterial sample is on the order of $10\,\mathrm{nm} \ll 2\,\mu\mathrm{m}$. Furthermore, the sample surface under investigation is aligned as parallel as possible to the microscope focal plane. Realistic residual angles ϕ are on the order of a few degrees only. Nonetheless, this can still introduce an artifact displacement along the x-axis similar in magnitude to the displacement along the z-axis. This effect is presented in Figure 4.5. An in-plane displacement of almost the same magnitude as the out-of-plane excitation is detected as an artefact by the DIC analysis. To suppress this effect, a coarser axial sectioning has to be chosen.

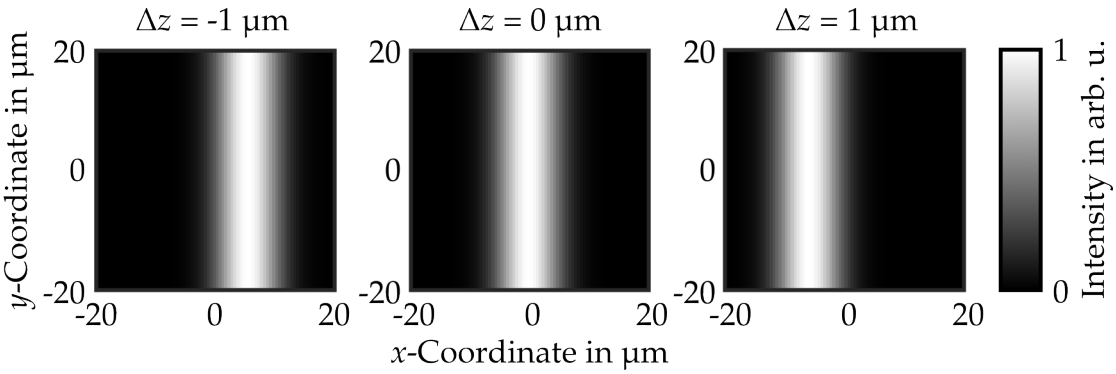

Figure 4.4: Simulated intensity distribution created by a reflective and tilted plane P with respect to the microscope focal plane. A tilt angle of $\phi = 10°$ around the y-axis is chosen. Due to optical sectioning, only a single bright fringe is visible. (left) The plane is displaced by $\Delta z = -1\,\mu m$, (middle) $\Delta z = 0\,\mu m$ and (right) $\Delta z = 1\,\mu m$ along the optical (z) axis of the microscope. The intensity distributions were created by multiplying the height profile of P for three different shifts along the z-axis with a measured (axial) response of the confocal microscope. The bright fringe is moving along the x-axis, even though the displacement of the plane along this direction is zero.

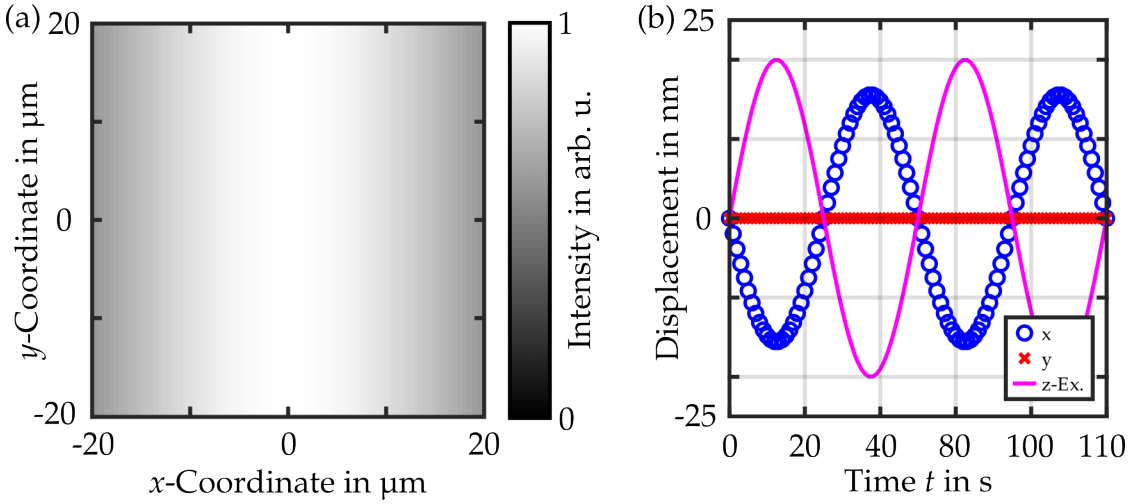

Figure 4.5: (a) Simulated intensity distribution for a tilt of $\phi = 2°$ between sample plane and focal plane using a pinhole diameter of $d_{Ph} = 20\,\mu m$. The edges appear darker due to the influence of the pinhole. (b) Displacement data when oscillating the plane along the optical z-axis. This excitation is drawn as a solid line for comparison (magenta). A significant displacement along the x-axis is detected by DIC analysis as an artefact (blue circles). No displacement along the y-axis is detected (red crosses).

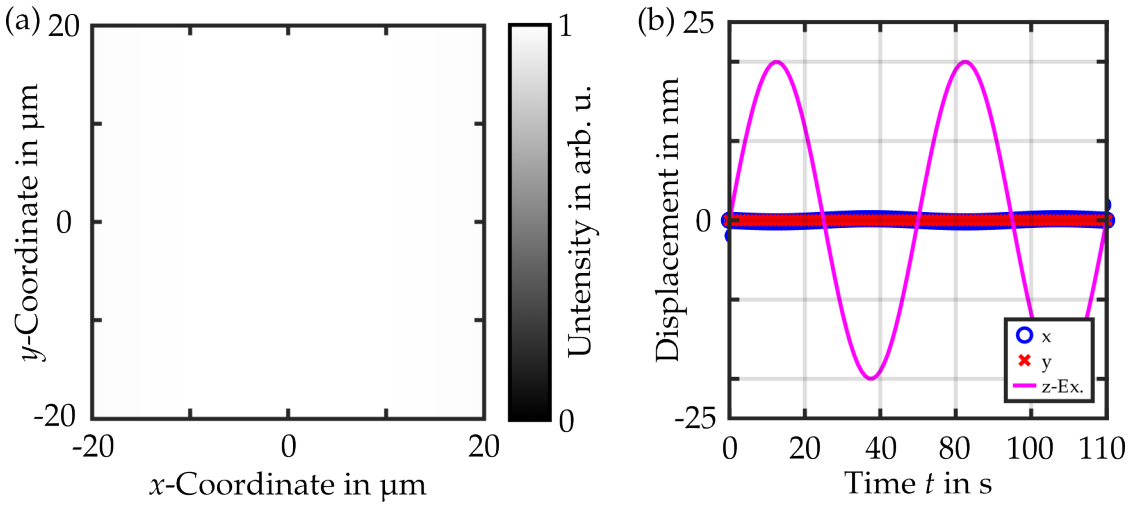

Figure 4.6: (a) Analogy to Figure 4.5, but for a pinhole diameter of $d_{\mathrm{Ph}} = 200\,\mu\mathrm{m}$. The intensity distribution now appears uniform. (b) Displacement data when oscillating the plane along the optical z-axis. This excitation is drawn as a solid line for comparison (magenta). Almost no displacement along the x-direction (blue circles) is detected by DIC analysis anymore, due to the now much coarser axial sectioning.

This is achieved by increasing the pinhole diameter from $d_{\mathrm{Ph}} = 20\,\mu\mathrm{m}$ to $200\,\mu\mathrm{m}$. The resulting behavior is given in Figure 4.6. The axial sectioning is now much coarser with a FWHM of $10\,\mu\mathrm{m}$ of the axial response (cf. Figure 4.3(b)). This value is significantly larger than the expected displacements and arguably large for typical confocal microscopes. However, it is still about an order of magnitude smaller than the lattice constant of the metamaterial samples under investigation in this thesis. Therefore, this choice is considered a useful trade-off between axial sectioning capabilities of the microscope and robustness against displacement artefacts.

Summary

When applying DIC analysis to images acquired with an optical sectioning technique, only features on flat surfaces parallel to the focal plane should be tracked. Thus, it is unwise to place the kernel for DIC onto a tilted or sloped object, as axial movement of the latter will translate into an in-plane movement as an artefact. The problem can further be mitigated by choice of coarser axial sectioning using a larger pinhole diameter. As a rule of thumb, the FWHM of the axial response should be orders of magnitude larger than the expected displacement in the experiments.

4.2 Addition of the Laser-Doppler Vibrometry

Following the description of the confocal-imaging branch reported above, the implementation of the laser-Doppler-vibrometry branch is described in this section. The addition of the vibrometry branch completes the 3D displacement-measurement capability of the setup. The section starts with the description of the additional beam path that makes up the Mach-Zehnder interferometer. The complete setup with confocal-microscopy branch and laser-Doppler-vibrometry branch was already published in the supporting information of [92]. Subsequently, the alignment of the vibrometry measurement point onto the center of the field of view of the confocal-microscopy branch is accounted for. Lastly, an important calibration procedure for a vibrometer integrated into a confocal (or any optical) microscopy setup is discussed.

4.2.1 Design of the optical beam path

The description of the beam path for the laser-Doppler-vibrometry branch focuses on the components that are added to the already existing confocal-microscopy branch. The expanded schematic of the setup is illustrated in Figure 4.7. In the explanation, the distinction is made between the interferometer reference arm with the reference beam, and the sample arm entailing the sample beam.

The reference arm of the interferometer starts at the thin film beam splitter (TFBS) and proceeds towards the acousto-optic modulator (AOM). The beam diameter at the TFBS is 1.87 mm. In order to match the entrance aperture of the AOM, the reference beam is down-sized by a telescope with $f_7 = 100\,\text{mm}$ and $f_8 = 50\,\text{mm}$ to 0.93 mm. The angle of incidence onto the AOM is chosen such that the maximum intensity is diffracted into the first diffraction order. Other diffraction orders are blocked by an iris diaphragm.

The optical frequency of the transmitted reference beam is shifted by the phonon frequency of $f_B = 80\,\text{MHz}$, which forms the baseline for the heterodyning. The intensity of this first-order diffracted beam can be modulated by a voltage supplied to the AOM. This sets the heterodyne amplification by adjusting the power of the reference beam P_R and can be used to achieve shot-noise limited acquisition (cf. Equation 3.29, Equation 3.30).

Subsequently, the reference beam diameter is resized by another telescope (TEL5) to match the beam diameter of the sample beam, which is back-reflected from the sample and arrives at the TFBS. The focal lengths of TEL5 are $f_9 = 50\,\text{mm}$ and $f_{10} = 100\,\text{mm}$. Matching the beam diameter of the reference beam and sample beam allows to maximize their spatial overlap when overlaying both beams with detection lens DL2 onto the tip of a multimode fiber.

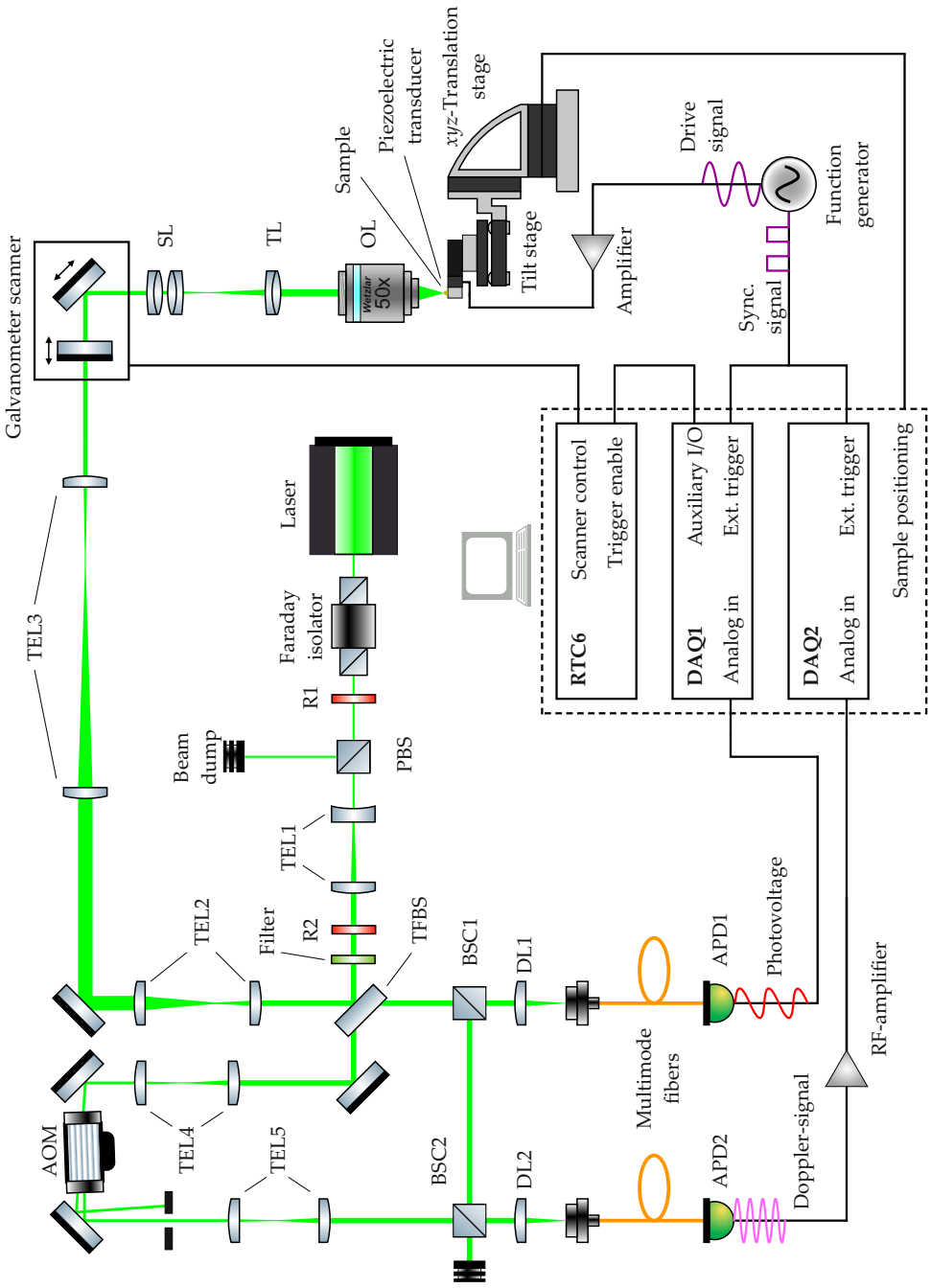

Figure 4.7: Schematic of the experimental setup expanded by a laser-Doppler vibrometer. Similar to Figure 4.1 but with additional components that make up the vibrometry branch. Two telescopes (TEL4-TEL5) and beam splitter cubes (BSC1-BSC2). Acousto-optic modulator (AOM). Additional second detection lens (DL2) and second data acquisition unit (DAQ2). Figure and caption taken from [92] and reproduced under (CC BY 4.0), published by Adv. Mat. 2023.

Doing so results in a minimal DC component of the electric-field interference pattern (cf. Equation 3.17).

The sample arm of the vibrometer starts from the TFBS and leads towards the sample in the focal plane of the objective lens. Logically, the beam path is simultaneously the illumination path for confocal imaging described in Section 4.1.1. The detection path for the vibrometry branch starts behind the TFBS, at the first beam-splitter cube (BSC1). This cube splits the beam which is back-reflected from the sample by a ratio of 50 : 50 with respect to power. The transmitted beam is used for confocal imaging as described before (see Section 4.1.1). The reflected beam from BSC1 is the sample beam and overlayed with the reference beam to create the interference pattern and thus the laser-Doppler vibrometry signal. For this purpose, a second beam-splitter cube (BSC2) is utilized. Recalling Equation 3.32 states that the resolution of the vibrometer is limited by the power P_S of the sample beam. Consequently, a 90:10 ratio is used for BSC2 such that 90 % of the valuable sample beam power is available as contribution to the laser-Doppler signal at the detector[6].

The intensity of the interference pattern is recorded by the second avalanche photodiode module (APD2). The avalanche photodiode is AC coupled, such that the analog output voltage signal of the module only follows the time-varying oscillation of the interference pattern intensity. Subsequently, the (Doppler) voltage signal is amplified by a radio-frequency (RF) amplifier to better match the input range of the following data acquisition unit (DAQ2). The latter digitizes the signal for IQ-demodulation (as described in Section 3.3.4), which is implemented in software on the personal computer (PC).

Overlaying the Vibrometry and Imaging Branches

It goes without saying that for a sensible measurement of a displacement in three dimensions, it must be ensured that the displacement data is taken from the same area on the sample under investigation. For the experimental setup, this translates that the focal points of the two detection lenses DL1 and DL2 are equivalent to each other. An axial mismatch on the order of the metamaterial feature size (several micrometers) could result that an out-of-plane displacement-vector component is measured by vibrometry from a different plane than the in-plane displacement-vector components extracted with DIC analysis. Obviously, this can lead to nonsensical results for the tracking of elastic waves in the metamaterials. Equivalently, if there is an in-plane shift between the two focal points, the out-of-plane displacement may be taken from a region where the displacement field

[6] Since the beam of the reference arm is not diminished in power compared to the beam of the sample arm which is reflected upon a low reflectivity polymer surface, the reference beam power is usually abundant.

already differs considerably. For thin sample features, it may even be the case that no sample surface is hit by the laser beam. Such an in-plane shift between the focal points can be caused by residual (different) tilted incident of the back-reflected beam into DL1 and DL2.

The equivalence can be verified by two straightforward experiments using the confocal imaging of the setup, i.e. APD1 and DAQ1. Since the detection of back-reflected light is fiber coupled, the multimode fiber with its tip in the focal plane of DL1 can simply be switched over to DL2 when needed. For these experiments, the reference beam path was blocked in order to not saturate APD1 with a DC-background.

For the out-of plane (z) direction, i.e. the axial equivalence, a glass-air interface is scanned through the focal plane of the objective lens and the back-reflected intensity is recorded at DL1 and DL2. The corresponding data is shown in Figure 4.8(a). By comparison, it can be seen that the overlap of both peaks is high and the maxima are within 1 µm of each other. Therefore it is ensured that the vibrometry branch yields displacement data from the same plane as the DIC analysis.

For verification of the in-plane equivalence, a USAF 1951 resolution test target

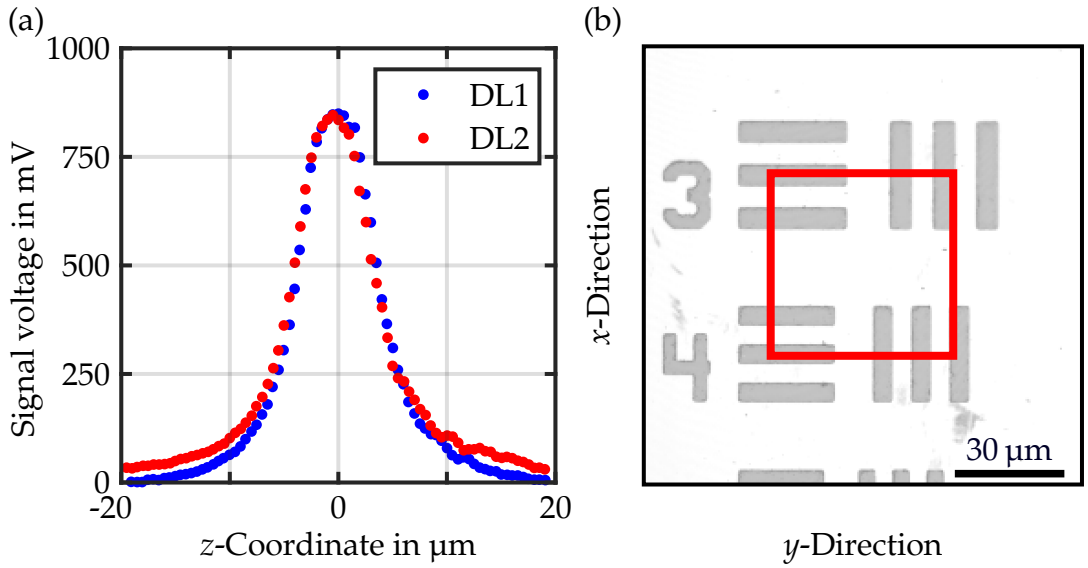

Figure 4.8: Data for the alignment of the vibrometry and imaging branches. (a) Comparison of signal response when axially scanning a glass-air interface through the focal plane of the objective lens. The light collected by the first detection lens (DL1, blue dots) and the second detection lens (DL2, red dots) is used to generate the voltage signal. (b) Image acquired with the confocal-imaging branch of group 6 elements 3 and 4 from an USAF 1951 resolution test target. The red box encloses the kernel of 100×100 pixels which is chosen in this instance for digital-image cross-correlation analysis. The image was rotated counter-clockwise by 90° for readability.

is used. An image of the group 6 elements 3 and 4 is acquired with the multimode fiber tip in the focal plane of DL1, as shown in Figure 4.8(b). Subsequently, the fiber is switched over to DL2 and another image is acquired. Finally, a kernel is selected from the image taken with DL1 and DIC analysis is performed on the image taken with DL2. In the following Chapters, the size of the kernel in the DIC analysis spans 40×40 pixels with a pixel size of $p = 500\,\mathrm{nm}$ unless stated otherwise. A lateral shift should thus be well below the kernel size for both the x- and the y direction. The DIC analysis yields an in-plane shift of $\Delta x = -6\,\mathrm{nm}$ and $\Delta y = 723\,\mathrm{nm}$. This is on the order of the pixel size, well below the size of the kernel, and therefore within acceptable limits[7].

4.2.2 *Amplitude Calibration for Laser-Doppler Microscopes*

It is established that laser-Doppler vibrometry is amongst the most accurate measurement technologies available [81]. The origin lies in usually precisely known wavelength of the laser, which serves as the reference for the displacement measurement. Therefore, laser-Doppler vibrometers (LDV) are used by national metrology institutes as primary reference measurement standards[8] [98]. The situation becomes however more complicated, when integrating a LDV into a (confocal) microscope[9] with a high numerical aperture. As mentioned above, the construction of the setup followed the example of Christian Rembe et al. [100]. Therein, it is derived, how an NA-dependent scaling factor has to be employed, to retrieve the correct absolute displacement amplitude of the sample. The authors of [100] attribute this to the Gouy phase shift of a Gaussian beam [101]. The shift describes the change in phase of the electric field, when passing along the optical z-axis through the focal plane at $z = 0$. The Gouy phase shift $\zeta(z)$ is usually calculated in units of the Rayleigh range z_R and Gaussian beam radius ω_0 in the focal plane:

$$z_\mathrm{R} = \frac{\pi\omega_0^2}{\lambda}\,, \tag{4.1}$$

$$\zeta(z) = \arctan\left(\frac{z}{z_\mathrm{R}}\right)\,. \tag{4.2}$$

With Gaussian beam propagation it can be shown that the phase of the Doppler interference signal depends not only on the time-dependent displacement $z(t)$, but also on the Gouy phase shift. Therefore, Equation 3.27 is modified to:

$$\varphi_\mathrm{D}(t) = \frac{4\pi}{\lambda}\cdot z(t) - 2\arctan\left(\frac{z(t)}{z_\mathrm{R}}\right)\,. \tag{4.3}$$

The contribution of the arctan is most significant for a small Rayleigh range.

[7] Naturally, for large discrepancies ($\gg p$) more careful alignment is necessary.
[8] For traceable calibration, ISO 16063-41 standards are defined.
[9] The first integration of a LDV into a microscope was performed in 1974 [99].

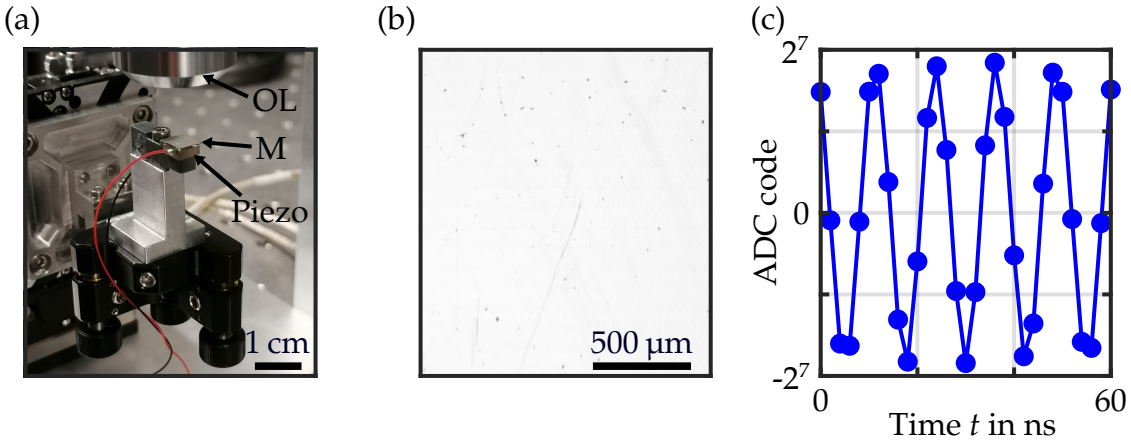

Figure 4.9: Setup and sample to calibrate the vibrometer branch. (a) Photograph of the reflective reference sample, which is an aluminum-oxide coated glass substrate (M), glued onto a piezoelectric transducer (PL055, Physik Instrumente). The transducer main axis is aligned with the optical axis using the tilt stage shown below. The objective lens (OL) can be seen an the top (PL8x/0.18, Wetzlar). (b) Image acquired from the mirror surface. The uniform illumination is a indicator for good parallel alignment between optical axis and surface normal. (c) Raw Doppler-signal digitized by the ADC. Due to the high reflectivity, the full scale of the 14-bit ADC can be used. The lines connecting points serve visualization only.

Since the Rayleigh range is defined as the distance over which the beam diameter doubles in area, it is intuitive to understand that the effect is especially pronounced for strongly focusing objective lenses with large NA. For LDV with stand-off distances[10] in the range of meters, mostly low-NA objectives with NA $= 0.01$ are used and the influence of the Gouy phase shift becomes negligible. This is different for a confocal microscope. The NA of the objective lens used in the setup of this work is equal to 0.6. At a wavelength of 532.3 nm, a Rayleigh range of about $z_\mathrm{R} \approx 500\,\mathrm{nm}$ results. This is approaching the order of the displacement amplitudes observed in this thesis and cannot be neglected completely. Albeit, for small enough time-dependent displacements $z(t)$, a first order approximation can be made:

$$\varphi(t) \overset{(z \ll z_\mathrm{R})}{\approx} \frac{4\pi}{\lambda} \cdot z(t) - 2\frac{z(t)}{z_\mathrm{R}} = \left(\frac{4\pi}{\lambda} - \frac{2}{z_\mathrm{R}}\right) \cdot z(t)\ . \tag{4.4}$$

This imparts the impression that the error can be removed when the Rayleigh range is known. Rembe et al. tried to verify their model accordingly. To do so, several objective lenses of different numerical aperture and magnifications were tested on a reference actuator with well known displacement. They observed vast differences between the error predicted by theory and the error measured in the experiment. They speculate that Abbe's sine-condition [102] was not taken into account in

[10] Distance between LDV and sample.

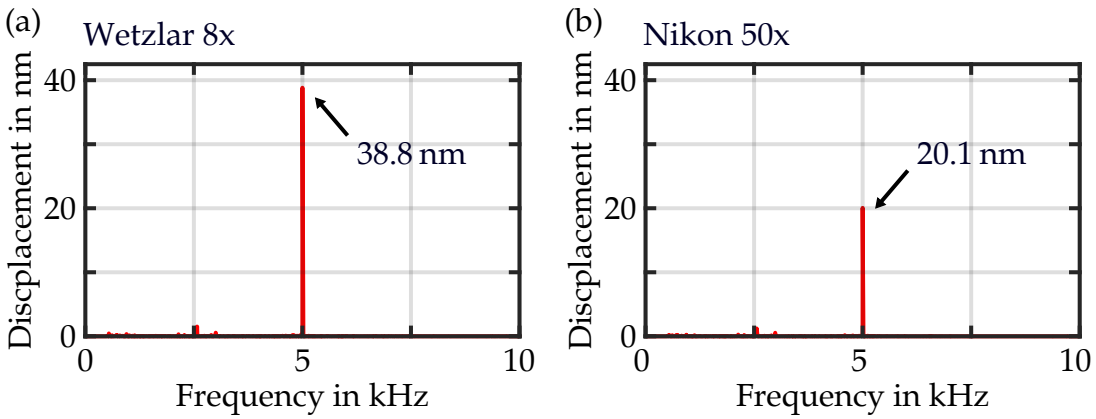

Figure 4.10: Comparison of the demodulated displacement signal spectra for (a) the low NA objective lens (PL8x/0.18, Wetzlar) and (b) the high NA objective lens (50x CFI60 TU Plan Epi ELWD, Nikon). The spectra were calculated using fast Fourier transformation (FFT) of $z(t)$ with a spectral resolution of 0.2 Hz. The displacement is generated in both cases by harmonically driving the piezoelectric transducer at 5 kHz with a peak-peak voltage of $U_{\mathrm{pp}} = 4\,\mathrm{V}$.

their calculations, which may be the cause of that deviation. Gaussian beams are a paraxial approximation and become inaccurate for high NA systems, while Abbe's condition has to be satisfied in non-paraxial cases as well. However, as a solution they suggest that a calibration should be done for a LDV integrated into a confocal microscope. In this calibration, a fixed displacement amplitude has to be measured with a low NA objective lens and subsequently with a high NA objective lens. Assuming that the displacement amplitude of a piezoelectric transducer is reproducible within a few percent, one can determine the scaling factor to retrieve the correct displacement amplitude. One way to avoid this dilemma alltogether is to only concern oneself with relative displacements, which is mostly possible for the investigation of mechanical metamaterials. However, when absolute displacements have to be considered, the calibration is indispensable, equivalently to the calibration of the microscope field of view (FOV). Otherwise, displacement amplitudes along the in-plane (x, y) and out-of-plane (z) directions cannot be compared.

For the sake of integrity, I performed corresponding calibration measurements of the LDV branch. The piezoelectric transducer is shown in Figure 4.9(a). To increase the laser-Doppler signal, a glass substrate coated with aluminum oxide is glued onto the transducer. This self-made mirror serves as calibration target for the LDV branch. For any calibration procedure with an LDV, it is vital to align the calibration target surface (air-metal interface) perpendicular to the incident laser beam. Laser-Doppler vibrometry can only determine the displacement component along the laser beam axis. As a metric for the alignment, the interface position

when scanning the target along the z-axis and determining the tilt from their respective heights. The position measurement is performed by the z-stage of the setup. To visualize the alignment, it is possible to acquire an image of the target. For good alignment, the intensity distribution of the back-reflected light over the FOV should be uniform or at least rotationaly symmetric with respect to the optical axis, cf. Figure 4.9(b). Using the full scale of the ADC, guarantees the best possible displacement resolution in the experiment. To calibrate the displacement measurement, the transducer is driven with a time-harmonic voltage at 5 kHz and peak-peak amplitude of 4 V. The measurement time per run is 2 seconds, resulting in a spectral resolution of 0.5 Hz. This ensures that no amplitude error due to spectral leakage occurs in the subsequent Fourier analysis of the displacement data. For the low NA case, the PL8x (Wetzlar) with NA = 0.18 is used. However, the microscope system was designed for an objective lens with a back-aperture diameter of 4.8 mm. The PL8x features a much larger diameter of 7.2 mm, thus the effective numerical aperture is NA $= 0.12$, thus well below the limit of 0.25 proposed by Rembe et al. The high NA lens is the 50x CFI60 TU Plan Epi ELWD from Nikon with NA $= 0.6$. The spectra of the displacement data measured with both lenses is plotted in Figure 4.10. In conclusion, a scaling of 1.93 must be applied to any displacement amplitudes determined with the Nikon objective lens. A table with the scaling data for additional objective lenses is included in Appendix B.

4.3 Tracking Elastic Waves at Ultrasound Frequencies

This section elaborates and demonstrates how the displacement field of elastic waves is measured in a time-resolved manor. At first, I want to clarify some terminology. The time-dependent displacement-field [11]

$$\mathbf{u}(\mathbf{r}, t) \ ,$$

is a continuous function of spatial coordinates $\mathbf{r}$ on a body or sample. Moving on from here, I will continue to address this field that describes the entire displacements of a sample as displacement field. When speaking about a localized displacement, for example in a region of interest (ROI) at spatial coordinates $\mathbf{r}_{\mathrm{ROI}}$ i.e. where a displacement measurement is conducted, I will speak of the displacement vector $\mathbf{u}\left(\mathbf{r}_{\mathrm{ROI}}, t\right)$ with its three time-dependent displacement-vector components:

$$\mathbf{u}\left(\mathbf{r}_{\mathrm{ROI}}, t\right) = \left(u_x(\mathbf{r}_{\mathrm{ROI}}, t), u_y(\mathbf{r}_{\mathrm{ROI}}, t), u_z(\mathbf{r}_{\mathrm{ROI}}, t)\right)^{\mathrm{T}} \ . \tag{4.5}$$

I find this linguistic separation necessary. Strictly speaking, measurement of the entire displacement field $\mathbf{u}(\mathbf{r}, t)$ of a sample is extremely time-consuming, data-

[11] as defined in Chapter 2 Equation 2.14.

intensive and sometimes outright not possible, since displacement measurements in a material volume may be extremely challenging. Overlying material layers block or scatter the incident illumination and thus lead to poor image quality through the loss of signal. Nonetheless, the sampling of the displacement field on surfaces at deliberately chosen regions of interests is nicely possible with the experimental setup described in this Chapter.

The following section starts with a description on how elastic waves are excited and how they can be coupled into metamaterial samples. Due to the microscale of the metamaterials and the elastic properties (Young's modulus) of the constituent material, the elastic-wave temporal frequencies lie in the ultrasound regime. Therefore, the measurement technique is described, with which the bandwidth of the photodiode and synchronization of the data acquisition allow to capture the time-resolved displacement-vector components at those frequencies. Lastly, a demonstration is provided, where the displacement vector on a metamaterial-beam sample is measured and plotted for several ROIs along the beam axis.

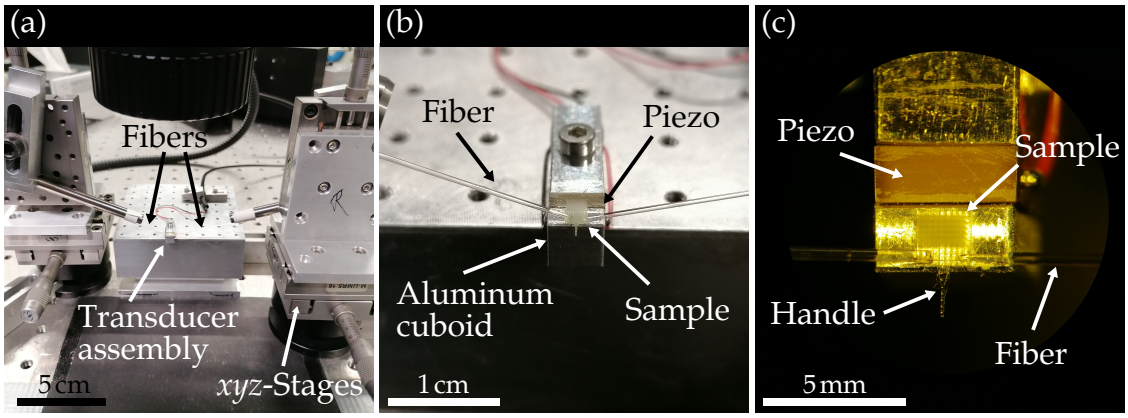

Figure 4.11: Photographs to illustrate the coupling of a metamaterial sample to a piezoelectric transducer. (a) Setup for gluing the metamaterial sample onto a (piezoelectric) transducer assembly. Manual *xyz*-translation stages allow to manipulate glass fibers to move or fixate a metamaterial sample. (b) Closer-view of the transducer assembly, where both the sample and the transducer (piezo) can be seen. An aluminum cuboid serves as an elbow piece. (c) View from the top through a binocular microscope under yellow-light illumination. The visible sample was printed in one piece onto a bottom plate with a small handle. The latter can be seen sticking out from the aluminum cuboid. Figure taken from [92] and adapted under (CC BY 4.0), published by Adv. Mat. 2023.

4.3.1 *Excitation of Elastic Waves*

For the excitation of elastic waves in the ultrasound frequency range, a fast and controllable source of mechanical displacements is required. Naturally, this can be best achieved with piezoelectric crystals. Piezoelectric transducers are commercially available as off-the-shelf products. For this work, longitudinal multilayer transducers are chosen (PL055.31 PICMA®, Physik Instrumente), with a dimension of $5 \times 5 \times 2\,\mathrm{mm}^3$. In principle, these transducers react with a displacement which is proportional to the (not too large[12]) voltage applied to the device and oriented along the electric field between the layers. When driving the transducer with a time-harmonic voltage, the main mode of displacement-oscillation is a so-called thickness mode along the smallest physical dimension [103]. This direction is called the transducer axis throughout this work.

To transfer the piezo-electrically induced displacements onto a metamaterial sample, mechanical coupling is required. This can be achieved by gluing the sample onto the actuator directly. However in the scope of this thesis, it turned out to be beneficial to introduce an additional layer such as a glass substrate or an aluminum cuboid as mediator. Such mediators average the displacement of the transducer to a certain degree over its cross-section. The displacement over the transducer cross-section can be non-uniform for several reasons. The transducer has a dead-zone at two sides due to the contacting of the electrodes. Those break the symmetry of the transducer. Furthermore, mounting of the transducer by gluing may not be perfectly uniform. These asymmetries can cause the actuator to also show significant displacements along different directions than its main axis. The same holds true for the mass-loading of the transducer which is introduced by these mediators. Therefore, the substrates and cuboids are cut to the size of the transducer cross-section, to ensure mostly symmetric mass loading.

An example for a transducer assembly with a metamaterial sample is shown in Figure 4.11. Additionally, the setup which is used for gluing the metamaterial sample to the transducer assembly is depicted. The metamaterial samples in this work are printed onto a bottom plate with a small handle. This handle can be grabbed with tweezers to coarsely position the sample onto the aluminum cuboid of the transducer assembly. More precise positioning is achieved with two glass fibers which can be manipulated by manual xyz-translation stages. For gluing, the fibers push onto the bottom plate and fix the sample in place.

A drop of glue (UHU, Plast Spezial) is applied next to the sample by a syringe. The bottom plate features a channel system which sucks in the glue through capillary action. During the gluing, the process can be monitored through a binocular microscope.

[12] For too-large voltage, the linear regime of the piezoelectric effect is exceeded.

Thereby, it can be assessed if the gluing and thus the coupling between the metamaterial sample and the transducer assembly is successful. Insufficient amounts of glue or non-uniform distribution of glue between bottom plate and transducer assembly may lead to poor coupling. Consequently, small displacements of the elastic waves in the metamaterial may result, which lie even below the sensitivity limit of the experimental setup. In truth, there is no quantitative metric to judge the success of this process or the efficiency of the coupling and one has to rely on the experience of the experimentalist.

4.3.2 Displacement Extraction at Ultrasound Frequencies

To capture or track the displacement field of elastic waves at ultrasound frequencies above 20 kHz, it is clear that any measurement setup must provide a sample rate of at least twice the highest frequency under observation [68]. For an imaging setup, this calls for a frame-rate only achievable with high-speed cameras. However, there are other methods to circumvent such expensive devices. A common practice in the context of metamaterials is stroboscopic illumination, which down-mixes the fast mechanical oscillations into a frequency range compatible with conventional cameras operating at several tens of frames per seconds. This has been used extensively by my collegueas Tobias Frenzel and Julian Köpfler. However, in their work, they used wide-field microscopy setups.

For a confocal microscope, the situation is different. The limit on the frame-rate is imposed first and foremost by the velocity with which the laser focus can be scanned over the sample surface. As an order of magnitude, only a few frames per second are achievable. However, as has been mentioned in Chapter 3 and Section 4.1.1, confocal microscopes feature fast single-pixel detectors like avalanche photodiodes with high analog bandwidths of around 10 MHz [59]. Combining such detectors with appropriately synchronized data acquisition, allows to avoid both stroboscopic illumination and high framerates altogether. A essential premise is that the displacement field is time-periodic, which is the case for the experiments performed for this thesis.

The procedure to obtain the in-plane displacement-vector components at a single region of interest (ROI) was already published in [94] and is recapitulated here with minor changes to resemble the state of the setup at the time of writing. Elastic waves are excited in the metamaterial sample by a piezoelectric transducer which is actuated by an amplified time-harmonic voltage at frequency f_m, called the drive signal. The laser focus is moved to the first pixel of the ROI by the galvanometric scanner. Once the RTC6 card confirms the position of the laser beam, it arms the DAQ1 by enabling its trigger through its auxiliary I/O port.

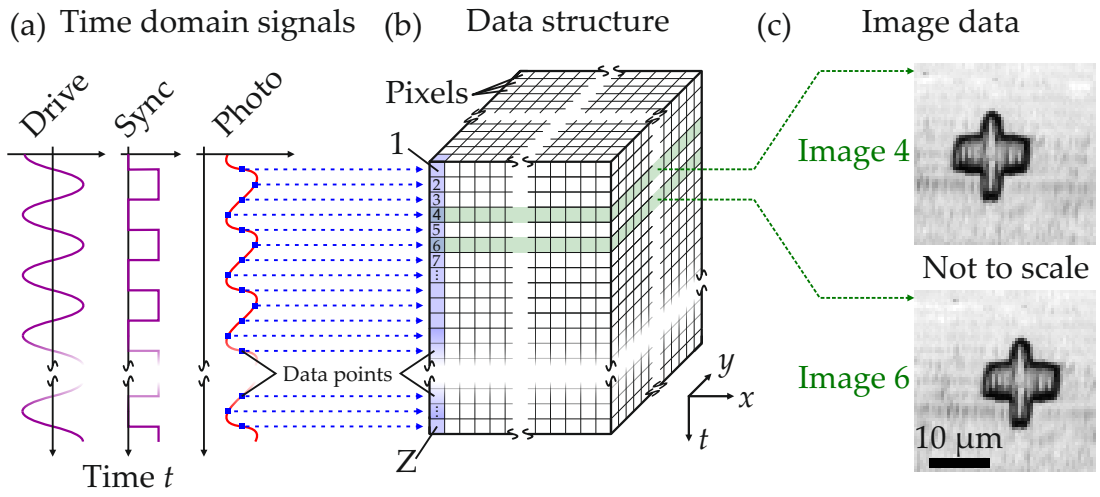

Figure 4.12: Illustration of the data structure for image generation to extract the in-plane displacement-vector components for a single region of interest. (a) Time-domain signals governing the experiment. Elastic waves are induced by a piezoelectric transducer (not shown) which is driven by the time-harmonic drive signal. The latter is synchronised to the synchronization (sync) signal, which also serves as a trigger for the data acquisition unit digitizing the photovoltage (red). The data points of the resulting time-series are depicted as blue squares and belong to a single pixel in real-space. (b) Illustration of a dataset for one ROI at one excitation frequency. The data structure can be thought of as a cuboid. The lateral x- and y-directions indicated by the tripod are the real-space pixel coordinates of the image plane. The third direction is the time axis t. The numbered (from 1 to Z) and blue-shaded front left column of the cuboid represents the time-series data points acquired for the corresponding pixel. When arranging the time-series for every pixel in such a manner, image data for DIC analysis is reconstructed by taking slices through the cuboid, as highlighted by the green shading. (c) Two exemplary slices are shown, consisting of every 4th and 6th data point of the time-series. The depicted displacement of a cross-shaped marker is exaggerated for the purpose of visualization. Figure taken from [94] and adapted under (CC BY 4.0), published by Science Advances 2021.

For triggering, a rectangular voltage signal is used, also called the synchronization (sync) signal. It is generated by the same frequency generator that provides the drive signal for the transducer. Both signals share the same frequency f_m and thus have a fixed temporal phase relation to each other - a vital requirement for the following reconstruction of images discussed below. The photovoltage acquisition by DAQ1 starts on a falling edge[13] of the sync signal.

[13] Originally in [94], rising edges were used. However, it was necessary to employ a temporal gate to the trigger signal, which renders the rising edge of the gated sync signal unstable. Thus, a transition to falling edges was made.

When measuring the photovoltage, the high analog bandwidth of the APD1 together with the $10\,\mathrm{MS\,s^{-1}}$ rate of DAQ1 ensure that the oscillation-induced variations in the photovoltage are captured in the acquired time-series. The sampling theorem [68] is satisfied. Herein lies the key aspect that renders high frame-rates or stroboscopic illumination unnecessary in this confocal imaging setup.

In total, a time-series of Z data points is acquired for the currently illuminated pixel[14]. As soons as the acquisition is complete, the laser beam is shifted to the next pixel of the ROI and the process repeats until equivalent time-series for each pixel of the ROI are recorded.

The next step is to reconstruct images out of the set of time-series. For the sake of comprehensibility, the data structure can be imagined as a cuboid. This concept is depicted in Figure 4.12. Such reasoning is meaningful, since the synchronization of the data acquisition to the drive signal guarantees that all time-series are triggered at an equivalent overall temporal phase in the mechanical oscillation of the sample. In other words, the synchronization signal serves as a global phase reference for the experiment. The lateral dimensions of the cuboid represent pixel coordinates, while the third dimension incorporates the time axis. Taking slices (orthogonal to the t-axis) out of this cuboid reconstructs images of the ROI at a defined time-point in the mechanical oscillation. From this image data, the time-resolve in-plane displacement-vector components can be extracted using DIC analysis. Naturally, the number of images is identical with the number of data points Z of a time-series.

For the analysis in the experiments, a ROI size of 60×60 pixels, a kernel size of 40×40 pixels and a pixel size of $p = 500\,\mathrm{nm}$ is chosen. This concludes the measurement of the in-plane displacement-vector components.

The remaining out-of-plane displacement-vector component is measured with the laser-Doppler-vibrometry branch described previously. The procedure for this setup was also published in [92]. The measurement point is in the center of each ROI. Equivalently to the measurement of the photovoltage, DAQ2 is triggered by the same synchronization-signal edge to preserve the temporal phase information of the displacement data when sampling the Doppler-signal from APD2.

Digital signal processing of the Doppler-signal is implemented in software (MATLAB) using an IQ-demodulation approach discussed in Chapter 3 and visualized in Figure 3.6. The sample rate of DAQ2 is set to $500\,\mathrm{MS\,s^{-1}}$. A time-series of 2^{19} data points is acquired. For the demodulation, a numerical oscillator (NCO) frequency of 80 MHz is set. Low-pass filtering and data-decimation are performed with a moving average with a window-width of 64 data points.

[14] Depending on the experiment, either $Z = 1024$, $Z = 2048$ or $Z = 4200$ is chosen.

This results in an effective sample rate of $7.8125\,\mathrm{MS\,s^{-1}}$, which satisfies the Nyquist-Shannon sampling theorem [68] for the ultrasound mechanical oscillations.

To extract the Displacement-vector-component amplitudes from the raw data, either a least square fit of a sine function or Fourier analysis can be performed on the raw displacement data. The Fourier analysis [104] is performed in MATALB and uses the built-in fast Fourier transform (FFT) algorithm *fft* [105], based on [106]. When performing Fourier analysis, it is recommendable to truncate the length of the time-series in such a way that the FFT resolution equals an integer fraction of the frequency of the drive signal. Doing so minimizes spectral leakage [107] by providing a FFT bin for the frequency f_m.

4.3.3 *Example for Tracking of Elastic Waves in a Metamaterial*

To conclude this Chapter, an example for the measurement capability of the experimental setup is provided. To do so, a cross-shaped marker on the bottom of a metamaterial sample is chosen as a region of interest. The markers provide sharp edges and thus good image-contrast which benefits the DIC analysis (cf. Section 3.2). At the same time, the surface is smooth enough, to provide a specular reflection for the laser-Doppler vibrometry. The sample is coupled to a piezoelectric transducer assembly as explained in Section 4.3.1 and positioned in the focal plane of the microscope objective lens such that the marker is imaged. Figure 4.13(a) shows a raw image of the ROI containing the marker as it is reconstructed from the first (or topmost) slice of the data-structure cuboid introduced in Figure 4.12(b). A kernel is selected as indicated by the red box. This kernel is then used for DIC analysis of the other images (slices) from the dataset. The extracted time-resolved raw data for the in-plane displacement-vector components can be seen in Figure 4.13(b). Additionally, the raw-data for the out-of-plane component provided by vibrometry is included as well. The displacement raw data resembles the real part of the complex ansatz from Equation 2.39, but expanded to three dimensions:

$$u_l(\mathbf{r}_\mathrm{ROI}, t) = U_l' \cdot \exp\left[-\mathrm{i}(\omega t - \mathbf{k}\mathbf{r}_\mathrm{ROI})\right], \quad l \in \{x, y, z\}\ , \tag{4.6}$$

which is to be expected. No filtering is applied to the data up to this point, which emphasizes the high data-quality the experimental setup can provide. To extract the displacement amplitudes for each component, Fourier analysis is employed as mentioned above.

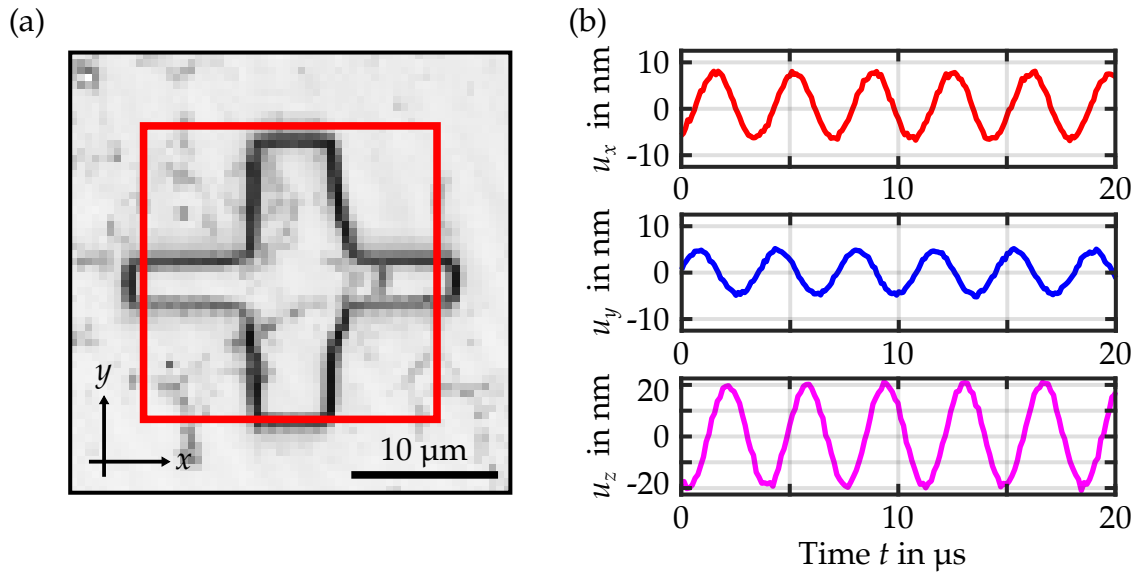

Figure 4.13: Three-dimensional displacement raw data extracted at a single region of interest. (a) Raw image with 60×60 pixels of a single ROI, centered on a cross-shaped marker to enhance image contrast. The red square encloses the 20×20 pixels kernel for the DIC analysis. (b) Time-resolved raw data for the three displacement-vector components u_x, u_y from DIC analysis and u_z from vibrometry. The excitation frequency is set to 275 kHz. All three displacement-vector components are nicely captured by the experimental setup.

Expanding this procedure from a single ROI to several periodically spaced ROI along the axis of a metamaterial-beam sample allows to extract its amplitude envelope for a given excitation frequency. For a metamaterial beam with lattice constant a and its axis parallel to the y-direction, the ROI have to be spaced

$$\mathbf{r}_{\mathrm{ROI}} = (0, ja, 0)^{\mathrm{T}}.$$

Therein, j is an integer designating a mass in the linear chain models from Section 2.2.2, or a unit cell in case of a metamaterial. The amplitude envelope arises in analogy to the discussion on elastic waves in periodic media (see Chapter 2). A standing-wave pattern forms as a superposition of two elastic waves. The first wave is excited by the transducer and propagates "upwards" along the beam, while the second wave originates from the reflection at the end of the finite metamaterial beam and propagates "downwards".

The displacement-vector amplitudes U_l with $l \in \{x, y, z\}$ of this superposition are measured on dedicated ROI along the beam axis. The result is given in Figure 4.14. The amplitudes U_l incorporate the spatial phase factor $(\mathrm{i}\mathbf{k}\mathbf{r}_{\mathrm{ROI}})$ from Equation 4.6 and thus form the amplitude envelope from which the time-dependency can be separated (cf. Equation 2.47).

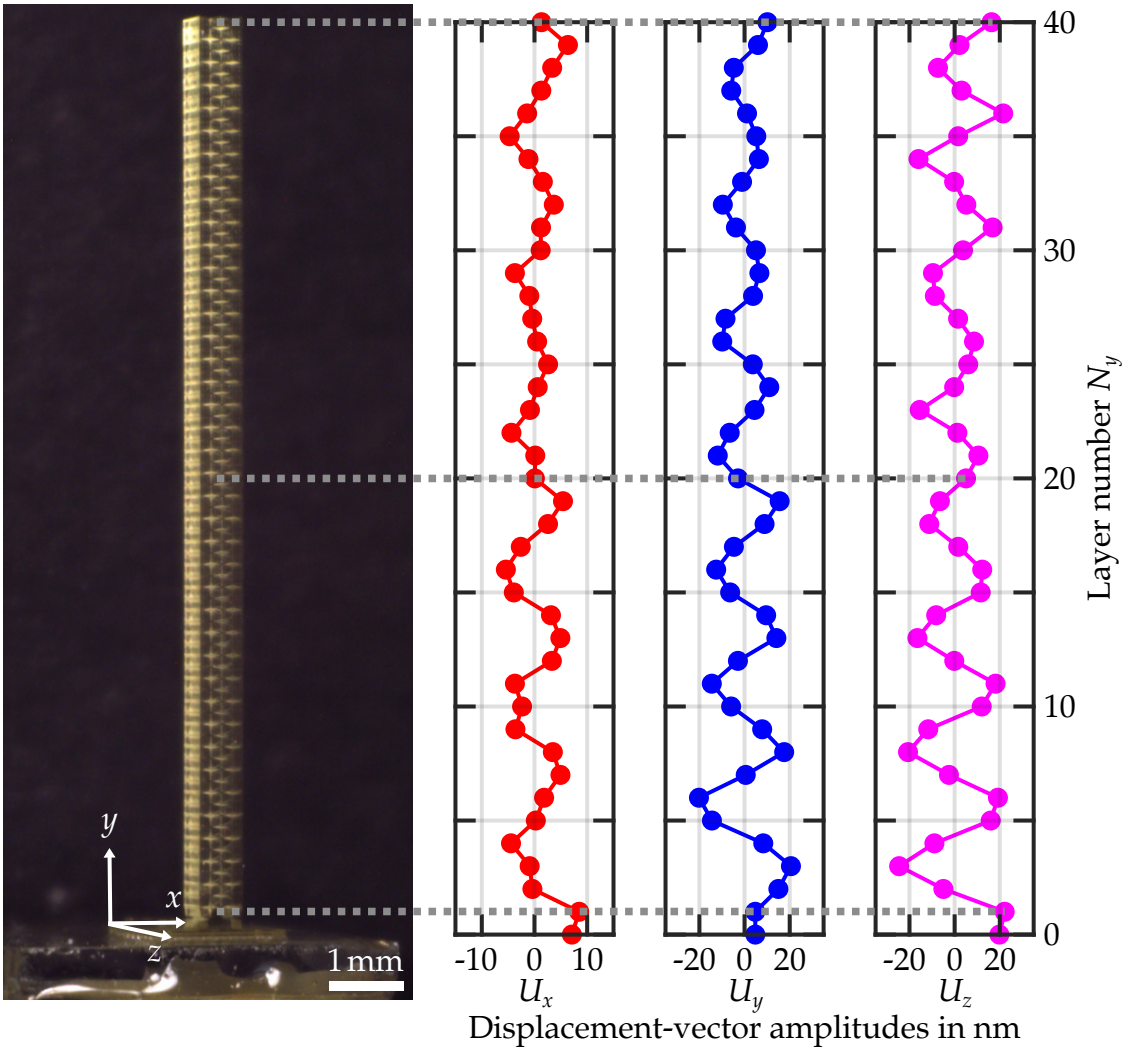

Figure 4.14: Displacement-vector-component amplitudes along the axis of a metamaterial beam. The beam consists of $2 \times 40 \times 1$ unit cells (along x, y, z) and can be seen on the left. The displacement vectors are measured at regions of interest (ROI) which follow in their spacing the $a = 300\,\mu\text{m}$ periodicity of the microstructure along the beam axis. On the right, the amplitudes U_x, U_y and U_z of the displacement-vector components u_x, u_y and u_z are plotted. The displacement amplitudes are extracted by Fourier analysis from the respective displacement-vector component. Consequently, U_x, U_y and U_z are plotted versus unit-cell layer number N_y of the beam. Horizontally dotted lines serve as guides for the eye, connecting the ROI position to the corresponding displacement amplitude data for the 1st, 20th and 40th layer. The ROI for the zeroth layer is situated on the bottom plate (close to the tripod). The excitation frequency in this example is 275 kHz, albeit the time-dependency is separated from the data in analogy to the amplitude envelope, which is derived for a one-dimensional chain in Equation 2.47. It is possible to understand this depiction as a three-dimensional snapshot of the samples amplitude envelope at the aforementioned frequency. The shown metamaterial-beam sample is discussed in more detail in Chapter 6.

It is the real part of this amplitude envelope that is plotted on the right side of Figure 4.14 for all three spatial dimensions. The ROI on the zeroth unit-cell layer of the metamaterial-beam sample corresponds to the position shown in Figure 4.13(a). The correct phase relation between the amplitudes of different layers is ensured by the synchronization of the drive signal to the data acquisition.

Acquiring amplitude envelopes for different temporal frequencies forms the baseline to determine the dispersion relation of elastic waves in the metamaterial samples. Fourier transformation of the amplitude envelope with respect to the spatial coordinate yields information about the present elastic waves. Thus, acquiring amplitude envelopes for different temporal frequencies allows to assemble the underlying elastic-wave dispersion relation or band structure of the metamaterial.

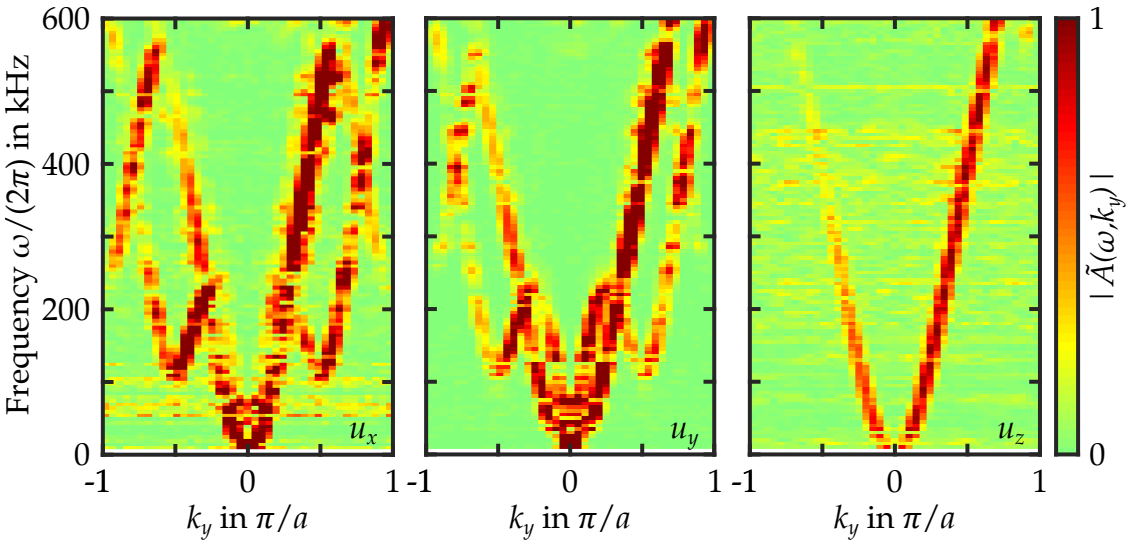

Figure 4.15: Wave dispersion reconstructed via Fourier transformation of the complex displacement-amplitude envelopes and depicted as false-color plot with normalized amplitude $|\tilde{A}(\omega, k_y)|$. From left to right, the displacement-vector components u_x, u_y and u_z were used for frequencies from 10 kHz to 600 kHz in increments of 5 kHz. As discussed in the text, the Fourier transformation with respect to space of amplitude envelopes for different frequencies reveals the dispersion relation for elastic waves. Here, several bands are visible. The details of the individual bands are elaborated on in greater detail in Chapter 6. The distinction with respect to the propagation direction of the elastic waves can be made when comparing the left half of the dispersion relation ($k_y < 0$) to the right half ($k_y > 0$). It is obvious that the bands are more pronounced for $k_y > 0$ as for $k_y < 0$. This means that the displacement amplitude of the waves propagating "upwards" in the beam is larger than the returning waves. This can be explained by damping in the structure.

To mitigate edge-effects, a Hann-windowing [107] is applied to the amplitude envelope before Fourier transformation. Two notable quantities govern the resolution when determining the band structure of such a metamaterial-beam sample. The number of unit cells (and thus number of ROI) govern the wavenumber i.e. k-space resolution of the experiment. Analogously, the frequency step size, i.e. frequency increment Δf of f_m determines the frequency resolution of the band-structure measurement.

Such experiments were conducted on three different types of metamaterials and are discussed in Chapter 5 and Chapter 6. A notable consequence of the fact that all phase information is maintained in the experiment is that the propagation direction of the waves making up the amplitude envelope can be resolved as well. This becomes apparent when Fourier transforming the complex displacement amplitudes (i.e. amplitude envelopes), which is shown in Figure 4.15. For the band-structure measurements conducted for the publications during this thesis, my co-authors and myself usually resorted to Fourier transformation of the real valued displacement data. The reason mainly lies in the nicer visualization of the band-structure results, as Fourier transformation of a real-valued quantity provides a symmetric spectrum. This makes the identification of individual bands and their pathway through k-space easier as they appear more cohesive.

Summary

In this Chapter, I reported the commissioning and characterization of the self-built experimental setup, comprised out of a optical confocal laser-scanning back-scattering microscope and a laser-Doppler vibrometer. A method to align the resulting confocal-microscopy branch and the laser-Doppler-vibrometry branch onto each other was described. Furthermore, I explained calibration procedures for the microscope field of view and the displacement-amplitude obtained with laser-Doppler vibrometry when using high-NA objective lenses due to the Gouy phase shift. Those calibrations are necessary when absolute displacement values are important, or in-plane displacements are to be compared with out-of-plane displacements. Additionally, I quantitatively discussed a cross-talk of out-of-plane displacements into in-plane displacements. The cross-talk can arise, when performing DIC analysis on image data obtained with an optical sectioning technique. To mitigate this effect, a sufficiently coarse sectioning must be chosen with respect to the anticipated displacement magnitude. Lastly, I provided a demonstration of the setup, by showcasing the tracking of elastic waves in a metamaterial-beam sample. All three time-resolved displacement-vector components were measured at designated ROIs. Displacement amplitude envelopes of the sample were reconstructed via Fourier analysis. The dominant elastic wave propagation direction was recovered from these amplitude envelopes for different excitation frequencies.

Chapter 5

5 Roton-like Dispersion in 3D Metamaterials

This Chapter spans the result of two projects [45, 94] on mechanical metamaterials conducted during this thesis. A non-trivial elastic-wave dispersion was achieved for the lowest acoustic bands of the finite metamaterial samples. At one temporal frequency, three propagating acoustic modes can coexist, one of which is a backward wave. Such phenomenon resembles the behavior of sound in superfluid helium or Bose-Einstein condensates at low temperatures and is called a roton dispersion. The metamaterials reported here incorporate two approaches, namely nonlocality and chiral couplings, to achieve a similar, roton-like dispersion relation. The latter is revealed in ultrasound phonon-band-structure measurements conducted with the setup described in the previous Chapter. The experiments on the nonlocal metamaterial were conducted by myself, while for the experiments on the chiral metamaterial, I acted in the role as a supervisor for my former master student Jonathan Schneider.

5.1 History and Properties of Rotons

The term "roton" was first introduced by Landau in 1941. He addressed the most noteworthy dispersion of acoustical longitudinal waves in superfluid helium [22]. He predicted a parabolic relation between wave energy and momentum[1] at simultaneously finite energy and nonzero momentum. A behavior, vastly different from the well-known linear dispersion of vibrational eigenstates (phonons) in gasses, liquids or solids [8]. Experimental evidence for such a roton dispersion relation was provided using inelastic neutron scattering [25], following the suggestions provided by Feynman et al. [23, 24].

The identifying feature for a roton dispersion is a region of negative slope, induced by the mentioned parabolic minimum in at least one of the dispersion bands. Thereby, for a single frequency, three modes of the same polarization but different wavenumbers k coexist simultaneously. Additionally, the negative slope of the band is synonymous with a negative group velocity $v_{\mathrm{gr}} = \mathrm{d}\omega/\,\mathrm{d}k < 0$ at a positive phase velocity $v_{\mathrm{ph}} = \omega/k > 0$ (cf. Equation 2.36, Equation 2.37), turning one of the waves into a backward wave.

Remarkably, backward waves can be connected to a negative index of refraction and raised significant interest at the beginning of the 21st century. Closely tied to the developments in metamaterials, a negative refractive index was experimentally realized in artificial structures for electromagnetic waves on multiple occasions [3, 4, 108].

These efforts follow the ongoing endeavor to tailor the dispersion relation of any sort of waves in metamaterials, which naturally also extends to acoustics and elasticity [109]. Along these lines, two suggestions were made in 2020, to achieve a roton dispersion relation in mechanical metamaterials. Before proceeding, the vastly differing underlying physics of rotons in superfluid helium and rotons in mechanical metamaterials should be attributed. No correlated quantum systems or low temperatures are necessary for metamaterials. To discriminate between both fields while acknowledging the similarities at the same time, the term "roton-like" for the elastic (or acoustic) waves in metamaterials is deemed more appropriate and is henceforth used throughout this thesis. To achieve roton-like dispersion, two proposals were followed upon.

The first proposal by Yi Chen et al. [26] relies on nonlocal couplings of masses, also termed beyond-nearest-neighbor interaction. The latter can be captured by an intuitive toy-model, which in itself is an extension of the previously discussed linear chain of masses (cf. Figure 2.3). Experiments I conducted on fabricated microscale metamaterial samples incorporating this principle of nonlocality are reported in Section 5.2.

[1] Landau received the Nobel prize for his work in 1961.

The second proposal is based on the work of Kishine et al. [27] and exploits chirality to achieve roton-like dispersion. The description of such a material requires an extension of standard Cauchy elasticity, namely micropolar elasticity as established by Eringen et al. in 1964 [110, 111]. Experiments performed on metamaterial samples which feature extreme chiral couplings to achieve roton-like dispersion are addressed in Section 5.3. Those experiments were conducted by my former student (and now valued colleague) Jonathan Schneider during his Masters thesis, which was carried out under my supervision.

5.2 A Nonlocal Approach

The experimental results discussed in this section were already published in [94]. Therein, a roton-like dispersion relation was achieved for waves in two types of metamaterials. On one hand, for elastic transverse waves in a microscale polymer-based metamaterial at ultrasound frequencies. On the other hand, for acoustic pressure waves in a channel-system metamaterial at audible frequencies. Both experiments were conducted at ambient conditions. The author of this thesis performed the experiments on the elastic microscale sample with the setup introduced in the previous Chapter 4. The metamaterial samples were fabricated using 3D laser microprinting by my former colleague Tobias Frenzel. The design of the metamaterial was suggested by my colleagues and co-authors Yi Chen et al. in [26].

In the following, I introduce and summarize the aforementioned toy-model following the lines of the authors of [26], since they offer an intuitive approach into the topic. Additionally, I will quickly outline an effective-medium description, which yields comparable results within certain limits. Subsequently, I present the unit-cell design, before reporting the findings of the experiments I conducted on the microscale polymer samples.

5.2.1 *An Intuitive Toy-Model and Effective-Medium Description*

The toy-model proposed by Yi Chen et al. [26] builds onto the well-known model of an infinite linear chain of masses m, spaced by distance a and coupled by Hooke's springs of constant D_1. The model is introduced in Chapter 2 Figure 2.3. Here, additional Hooke's springs of constant D_N and length Na are introduced, which mediate the N-th nearest-neighbor interaction. For this introduction, a coupling to the third-nearest-neighbor ($N = 3$) is discussed. The model is depicted in Figure 5.1(a). Newton's equation of motion for every j-th mass now also features

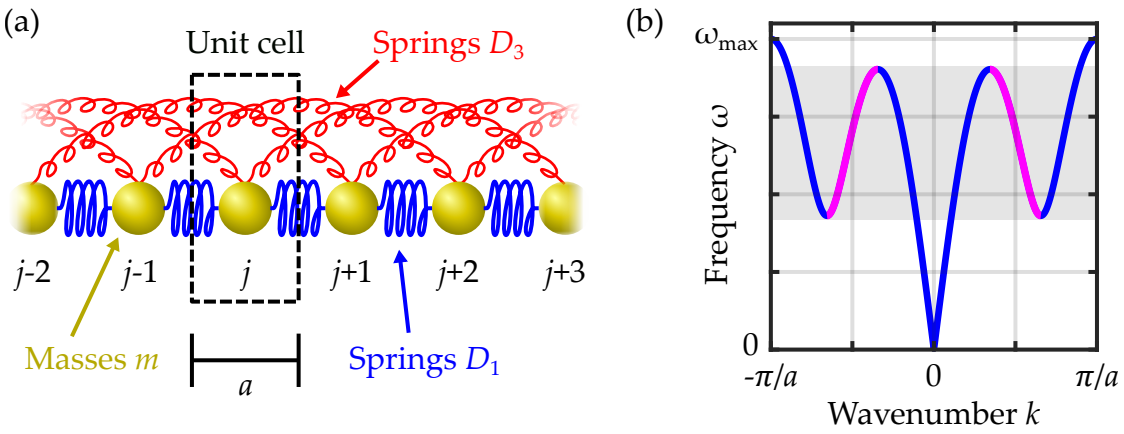

Figure 5.1: One-dimensional toy-model and dispersion relation incorporating third-nearest-neighbor interaction and thus extending the simple model shown in Figure 2.3. (a) The added Hooke's springs (red) of constant D_3 couple every j-th mass to their $(j \pm 3)$-th neighbors, while the lattice periodicity remains strictly a, as indicated by the unit cell. (b) The ensuing dispersion relation for $D_3 = 3D_1$. The frequency range featuring three waves at identical frequency but different wavenumber k is shaded gray. The portion of the band capturing waves with negative group velocity, and thus backward waves, is colored magenta.

additional components with $j \pm 3$ (cf. Equation 2.38):

$$F^{(j)} = m\ddot{u}^{(j)} = D_1 \left(u^{(j+1)} - 2u^{(j)} + u^{(j-1)} \right) + D_3 \left(u^{(j+3)} - 2u^{(j)} + u^{(j-3)} \right) . \quad (5.1)$$

Bloch waves with $u^j(t) = U \exp\left(\mathrm{i}(kja - \omega t)\right)$, as introduced in Equation 2.50 are the solution to the equation of motion. The dispersion relation of this infinite chain of masses unfolds to:

$$\omega(k) = \omega(-k) = 2\sqrt{\frac{D_1}{m} \cdot \sin^2\left(\frac{ka}{2}\right) + \frac{D_3}{m} \cdot \sin^2\left(\frac{3ka}{2}\right)} . \quad (5.2)$$

This dispersion is plotted in Figure 5.1(b). The parabolic minimum at wavenumber $k_{\min} = 2\pi/(Na) = 2\pi/(3a)$ is clearly visible. It needs to be emphasized that as long as $D_1 \neq 0$, the underlying and thus governing periodicity remains a. To check the consistency of Equation 5.2, a gedankenexperiment can be performed:

- Letting $D_3 \to 0$ with $D_1 \neq 0$ directly recovers Equation 2.40 and thus the already known dispersion of a linear chain without nonlocal interaction.
- Letting $D_1 \to 0$ with $D_3 \neq 0$ recovers three overlapping chains exhibiting conceptually the same dispersion, albeit for a larger periodicity of $3a$.

Basically, Equation 5.2 incorporates the usual acoustic dispersion of a 1D-chain (first term) and a faster oscillating part with respect to k (second term), due to

the larger superlattice periodicity $3a$. The latter results in a larger frequency $3/2a > 1/2a$ of the second sinusoid, the amplitude of which depends on the second spring constant D_3, or more precisely the ration D_1/D_3. In principle, following the reasoning of [26], the ensuing roton-like dispersion relation can be understood as the hybridization of two acoustical phonon dispersion relations. The authors of [26] argue that a pronounced roton-like minimum only occurs for a sufficient degree of nonlocality ($N \geq 3$) and a sufficiently strong beyond-nearest-neighbor coupling ($D_N/D_1 > 1/N$), with D_N as the spring constant of the coupling to the N-th nearest neighbor. These criteria were accounted for in their design of a metamaterial unit cell. Especially, $N = 3$ is the degree of nonlocality with arguably minimal complexity (compared to larger N) and therefore chosen in the metamaterial design discussed below.

Effective-Medium Description

As done in [94], an interesting and noteworthy point should be reiterated here for the sake of integrity. In the scope of metamaterials, it is oftentimes desirable to describe the metamaterial as an effective medium. Some may argue that this is even a vital point to separate a mere mechanism from a material altogether [47], an assessment I find very sound. It is shown in [94] that the occurrence of a roton-like dispersion can be captured by a higher-order-gradient effective-medium approximation. In short, the equation of motion is rewritten in the continuum limit for $a_z \to 0$ for the amplitude field $A = A(z,t)$:

$$\frac{\partial^2 A}{\partial t^2} = c_2 \frac{\partial^2 A}{\partial z^2} + c_4 \frac{\partial^4 A}{\partial z^4} + c_6 \frac{\partial^6 A}{\partial z^6} \,. \tag{5.3}$$

Thereof, an analytical approximation of the dispersion relation can be found, which is derived in the supporting information of [94]:

$$\omega(k_z) = \omega(-k_z) = \sqrt{c_2 k_z^2 - c_4 k_z^4 + c_6 k_z^6} \,. \tag{5.4}$$

Since effective-medium descriptions correspond to the limit of $a_z \to 0$, the information about the microstructure is lost to some extend. Thus, the model provides no good description of the material for wavenumbers close to the edge of the first Brillouin zone, where Bragg-reflections occur [8]. Nonetheless, the roton-like behavior can be positively captured by such a model, as will be demonstrated when fitting Equation 5.4 to the data obtained from (numerical) finite-element analysis.

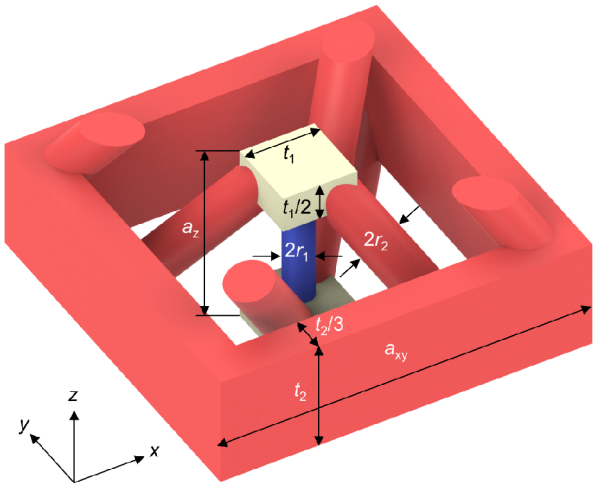

Figure 5.2: Blue print of the unit cell for the nonlocal roton metamaterial designed in [26] by Yi Chen et al. A metamaterial-beam sample comprised of such unit cells shows roton-like dispersion for elastic waves propagating along the z-direction. The blue and red shaded parts represent the nearest-neighbor and the beyond-nearest-neighbor coupling between the yellow masses, respectively. The geometrical parameters are given in in units of the axial lattice constant a_z. The lateral lattice constant is $a_{xy} = 2a_z$. Furthermore, the radii of the coupling rods are $r_1/a_z = 0.08$ and $r_2/a_z = 0.12$. Lastly, $t_1/a_z = 0.4$, $t_2/a_z = 0.6$ with $a_z = 100\,\mu m$. Figure from [94] published by Sci. Adv. 2021, and caption from [26], published by Nat. Commun. 2021. Adapted under (CC BY 4.0), respectively.

5.2.2 *Experimental Observation of Roton-Like Dispersion*

Herein, I start with introducing the metamaterial design envisioned in [26], before reporting the experimental results on fabricated finite samples. Based on their previously introduced toy-model, Yi Chen et al. proposed two metamaterial architectures which translate their 1D consideration into a 3D structure[2]. One of the architectures is a channel-based metamaterial for acoustic pressure waves, the other is a polymer based metamaterial for elastic transverse waves. In principle, those architectures are roughly complements of each other. Experiments on finite samples following those architectures were already published in [94], wherein I performed the experiments on the microscale polymer metamaterial samples. Therefore, I will focus on the polymer samples, the unit cell of which is shown in Figure 5.2.

Several parts of the unit cell are shaded to match the coloration of Figure 5.1. Yellow blocks correspond to masses, blue cylinders to springs mediating nearest-neighbor interaction and the red cylinders connected to frames are springs con-

[2] They emphasize that it is necessary to go to a 3D design, to not have any overlap (or contact) of the beyond-nearest-neighbour couplings.

veying the beyond-nearest-neighbor interaction. The critical parameters of this architecture are the radii r_1 and r_2 of the cylindrical rods[3]. The larger the respective radii are, the larger are the effective spring constants (local) D_1 and (nonlocal) D_3. The red-shaded rods are inclined in such a manner that they connect the shown unit cell to its third nearest neighbor. Thus, the order of nonlocality is $N = 3$, identical to the configuration chosen in the toy-model.

Furthermore, the geometry is achiral, as it features two mirror planes and a rotation-reflection symmetry [26]. Therefore, the two lowest acoustical and transverse phonon-bands are degenerate and a roton-like dispersion can be expected for both of them[4].

To form a metamaterial structure from this unit cell, it is imposed onto a translation lattice with tetragonal symmetry. Consequently, roton-like dispersion is only expected to occur for waves propagating along the z-axis with wavevector $\mathbf{k} = (0, 0, k_z)^{\mathrm{T}}$.

The Fabricated Metamaterial Sample

In order to perform experiments, finite metamaterial samples comprised of $2 \times 2 \times 50$ unit cells forming a beam were fabricated by my colleague Tobias Frenzel, using 3D laser microprinting (described in Section 2.3). For the printing process, a hatching distance of $d_{\mathrm{hatch}} = 300\,\mathrm{nm}$, and slicing distance of $d_{\mathrm{slice}} = 700\,\mathrm{nm}$ were chosen. Since the sample exceeds the printing field, several printing fields were stitched together. The spacing of these fields was 200 µm. Furthermore, a laser power of 27.5 mW and a laser focus scan speed (focus velocity) of $0.125\,\mathrm{m\,s^{-1}}$ were used. A bottom plate was included at one end of the beam samples to ease sample manipulation. The plate was printed at a laser power of 50 mW, scan speed of $0.140\,\mathrm{m\,s^{-1}}$ as well as $d_{\mathrm{hatch}} = 0.5\,\mu\mathrm{m}$, and $d_{\mathrm{slice}} = 1.5\,\mu\mathrm{m}$. After printing, the samples were rinsed for 20 min respectively in propylene glycol methyl ether acetate (PGMEA) and acetone, before critical point drying in CO_2, see Section 2.3. The writing strategy created by Tobias Frenzel can be inferred from the machine-code files contained in the repository of the corresponding publication[5] [94]. A showcase of the fabricated sample as they were used in the experiments is provided in Figure 5.3. Best results for the roton-like dispersion relation were achieved with slightly differing values for the radii r_1 and r_2 as originally introduced in the caption of Figure 5.2. While the axial lattice constant was maintained at $a_z = 100\,\mu\mathrm{m}$, the radii were $2r_1 = 16.8\,\mu\mathrm{m}$, $2r_2 = 25.2\,\mu\mathrm{m}$ were used.

[3] For $r_2 \gg r_1$, the roton-like minimum conceptually approaches zero frequency [26].

[4] Furthermore, the achirality sets this approach to achieve a roton-like dispersion apart from the metamaterials discussed in Section 5.3.

[5] https://doi.org/10.35097/488

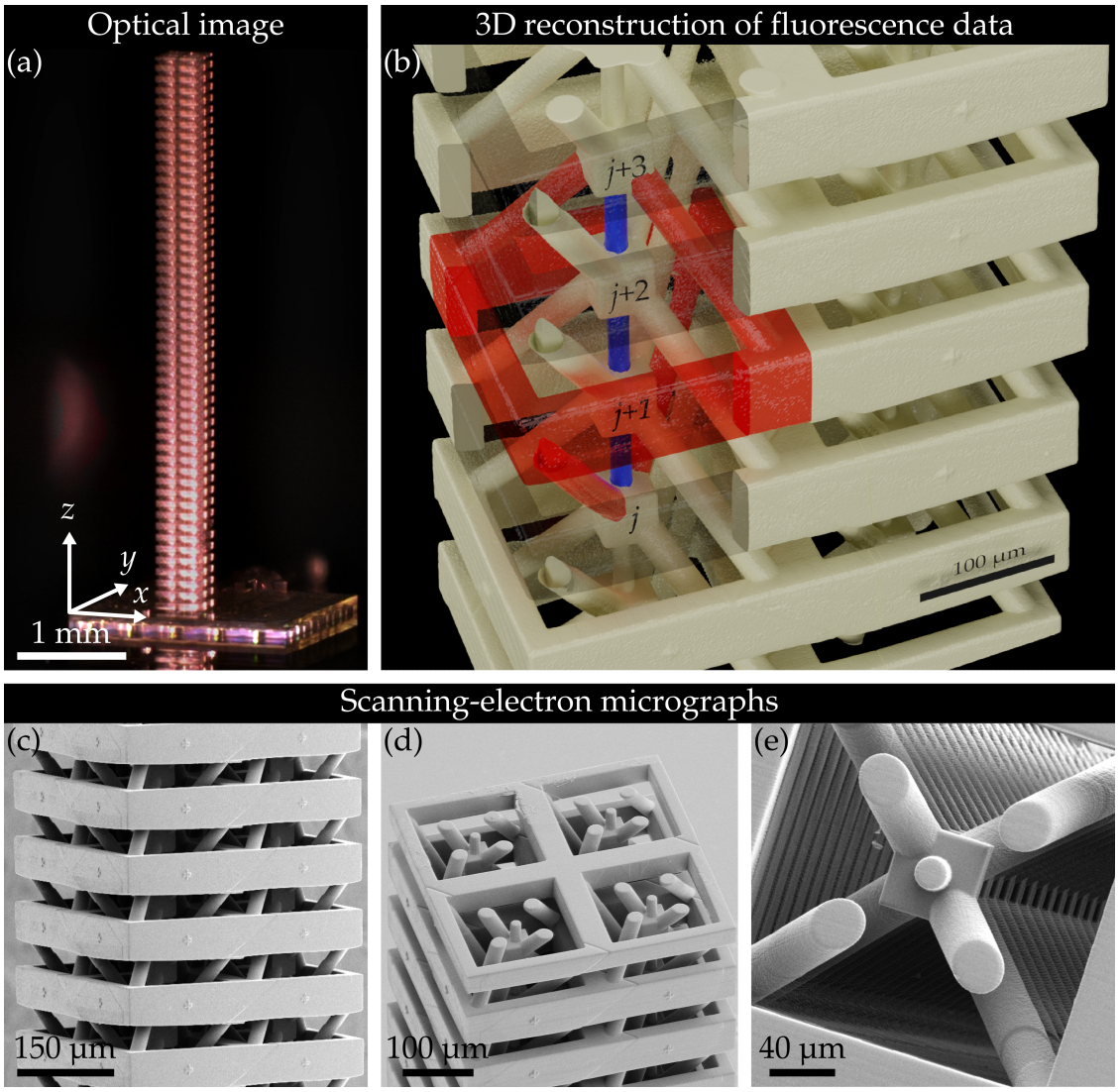

Figure 5.3: Showcase of the microscale metamaterial sample with nonlocal couplings. (a) Wide-field optical micrograph offering an overview of a printed polymer sample, consisting out of $2 \times 2 \times 50$ unit cells (for x, y and z). (b) 3D reconstruction of an iso-intensity surface obtained using a confocal flourescence microscope (LSM800, Zeiss). Signal is provided by the autofluorescence of the polymer. Coloring, mass-numbering and scale bar added in post-processing with Blender for visualization. The blue and red coloration highlights the nearest-neighbor and beyond-nearest-neighbor coupling, following the logic of Figure 5.2. Some superficial unit cell features are rendered transparent to unveil the interior of the microstructure. (c,d,e) Scanning-electron micrographs of a beam sample. (c) Close-up of the beam showing the outer-frames with cross-shaped markers for tracking with DIC analysis. (d) Topmost layers of the beam and (e) top-view along the beam (z-)axis through several unit cells. Figure and caption taken from [94] and adapted under (CC BY 4.0), published by Sci. Adv. 2021.

Band-Structure Measurements

At the time in which these experiments were performed, the experimental setup only featured the confocal-imaging branch. Logically, only the measurement of the in-plane displacement vector components was possible at the time. For the investigations of the roton metamaterial-beam samples this is sufficient, as long as the displacement of one of the transverse-polarized modes lies within the image plane. This is achieved by orienting the beam axis under 90° to the optical axis of the illumination path. In other words, looking at the sample from a side view.

As explained in Section 4.3.1 of the previous Chapter 4, elastic waves were excited using a piezoelectric transducer driven with a time-harmonic amplified voltage. To mainly excite transverse waves, the actuator axis was oriented under 90° to the beam axis. Following the procedure described in Section 4.3.3, the displacement field along the beam axis was sampled at 51 regions of interest (ROI) the spacing of which followed the periodicity a_z. The zeroth ROI is placed on the bottom plate and provides quantitative information about the mechanical excitation of the sample. Each ROI consisted of 60×60 pixels with a pixel size of $p = 500\,\mathrm{nm}$. Each ROI is centered on a cross-shaped marker to enhance image contrast and improve the signal-to-noise ratio of the following DIC analysis to extract the in-plane displacement-vector components. From this data, the amplitude envelope of the standing wave pattern oscillating at the excitation frequency f_m is reconstructed (cf. Figure 4.14). To extract the dispersion for relation over the frequency range covered by the hybridized phonon bands, amplitude envelopes for frequencies $f_\mathrm{m} = 20\,\mathrm{kHz}$ to $200\,\mathrm{kHz}$ in steps of $\Delta f = 5\,\mathrm{kHz}$ were acquired. The latter determines the frequency resolution of the band-structure measurement. Due to the beam sample consisting of 50 ROI in real-space, a total of 26 points in k-space result in the interval $k_z \in [0, \pi/a_z]$, which governs the k-space resolution of the experiment. Since only transverse polarized waves show roton-like behavior, it is sufficient to focus on the x-displacement vector component (coordinate system cf. Figure 5.3(a)).

For comparison, experimental results of these amplitude envelopes are plotted next to predictions from a finite-element analysis performed by Yi Chen in the left column of Figure 5.4(a) and (b). In the calculations, a Young's modulus of $E = 4.19\,\mathrm{GPa}$, a Poisson's ratio of $\nu = 0.4$ and a mass density of $\rho = 1140\,\mathrm{kg\,m^{-3}}$ for the constituent polymer were chosen. The complex amplitude-field $\tilde{A}^{(j)}(\omega)$, as a function of lattice site (or ROI number) j and angular frequency $\omega = 2\pi f_\mathrm{m}$ is depiction as a false-color plot[6]. In order to eliminate the influence of the frequency response of the piezoelectric transducer, $\tilde{A}^{(j)}(\omega)$ is normalized to unity power density $\sum_{j=1}^{50} |\tilde{A}^{(j)}(\omega)|^2 = 1$.

[6] This is another equivalent way of depicting the amplitude snapshot shown in Figure 4.14.

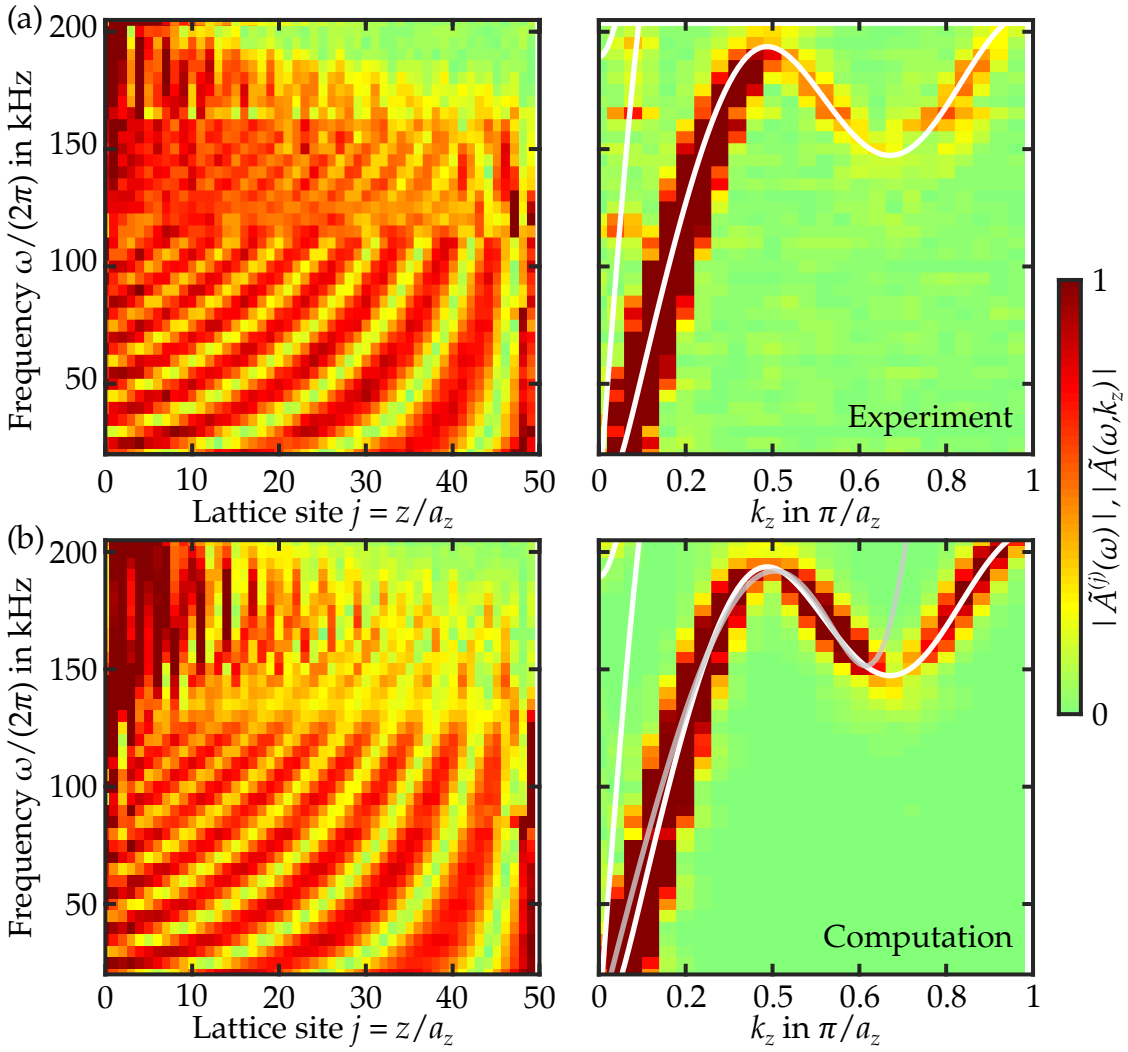

Figure 5.4: Comparison of measured and calculated displacement amplitude data and resulting roton-like dispersion relation for transverse elastic waves propagating along the z-direction. (a) On the left side, experimental raw data for the displacement-vector amplitude distribution over the lattice sites j, given in false-color by $|\tilde{A}^{(j)}(\omega)|$. On the right side, the corresponding band structure obtained by Fourier transformation with respect to space. The bands can be identified by following the maxima in the false-color plot of $|\tilde{A}(\omega, k_z)|$. The white solid lines are the roton-like bands predicted for a lossless metamaterial beam which is infinite along the direction of wave propagation. (b) Same as (a) but calculated using finite-element analysis for a finite beam including damping. Good agreement between computations and experiments is evident. Additionally, the gray curve represents the approximate analytical dispersion relation obtained from a higher-order gradient effective-medium model, which is elaborated in the text (cf. Equation 5.4). Figure and caption taken from [94] and adapted under (CC BY 4.0), published by Sci. Adv. 2021.

Subsequent Fourier transformation of the real part of $\tilde{A}^{(j)}(\omega)$ with respect to space $j = z/a_z$ yields $\tilde{A}(\omega, k_z)$. The maxima of the latter's absolute value reveal the desired band structure, see Figure 5.4 right column.

From Figure 5.4 it becomes apparent that predictions from theory using finite-element analysis for both infinite beams (Equation 2.48) and finite-beam samples (Equation 2.52) agree well with the experimental results. Naturally, computations for a finite sample are not affected by measurement noise, which makes the bands in Figure 5.4(b) appear slightly more prominent.

The result of the effective-medium description, is indicated by the gray line in Figure 5.4(b) (right). The coefficients c_2, c_4 and c_6 of which are obtained by fitting to the experimental data in the interval $k_z \in [0, 0.6\pi/a_z]$. As discussed previously, such a description cannot capture Bragg-reflections at the edge of the Brillouin zone. More information can be found in [94].

Summary

To the date of writing this thesis, achieving a roton-like dispersion through nonlocal coupling is extended in theory to two [112] and three [113] dimensions by Ke Wang et al. However, the underlying metamaterial structures exhibit an enormous increase in complexity and are thus challenging to fabricate. Hence, experimental evidence may be subject to future work. Furthermore, a roton-like dispersion was also achieved for photons in a cable-network metamaterial [114], extending the principle of nonlocal coupling to the electromagnetic domain, directly following the predictions made in [94]. Nonetheless, the experiments reported here on the microscale samples are among the first to realize a roton-like dispersion in the lowest acoustic bands of a metamaterial. It is thus safe to say that this work [94] sparked several interesting follow-up research and emphasizes the utility of nonlocal couplings in the tailoring of the dispersion relation for not just elastic waves.

In addition, the experimental results advocate and validate the method of tracking elastic waves using a confocal scanning microscope as a tool for this thesis. Thus, they formed an important milestone from which the experimental setup was expanded on to also capture the third displacement vector component via laser-Doppler vibrometry.

5.3 Chirality-Induced Roton-Like Dispersion

In this section, I report the realization of a roton-like dispersion relation in a microscale mechanical metamaterial through different means than beyond-nearest-neighbor coupling. Here, a carefully designed chiral structure with pronounced nonlocal chiral couplings was used. These results were produced during the Masters thesis of my former student Jonathan Schneider and were subsequently published [45].

Unfortunately, no simple and intuitive toy-model is known to me, in order to explain how the roton-like dispersion relation comes about through chirality. This may very well be attributed to the fact that the definition of chirality is somewhat difficult (if not impossible) in one dimension. Factually, not even Cauchy-elasticity can capture chiral effects[7]. Instead, an extension to micropolar elasticty, following Eringen [110, 111, 116] is required[8].

Along these lines, roton-like dispersion induced by chirality was predicted by Kishine et al. Their paper [27] was the key initiator for the work reported in this section. In contrast to the nonlocal case from above, hybridization of an optical and acoustic band produce the roton-like minimum (cf. Figure 2.4 hybridization of blue and magenta band needed), instead of the hybridization of two acoustic bands. However, no explicit structure or design path was provided to engineer a corresponding chiral material showing such a dispersion.

In the following text, a brief summary of the paper from Kishine et al. is given, to superficially present the effect of chirality on the dispersion relation of phonons. Subsequently, the unit-cell design conceived by Yi Chen, Muamer Kadic and Martin Wegener is explained. Afterwards, the sample fabrication, experiments and results are addressed.

5.3.1 *Effect of Chirality on the Phonon Dispersion*

Before discussing the phonon dispersion relation in a chiral material, I want to quickly introduce chirality itself. Chirality describes a special asymmetry of objects and was first defined by Lord Kelvin in 1984 [117] and refined by Whyte [118, 119]. An object is deemed chiral, if it cannot be superimposed by translations or rotations upon a mirror image of itself. More precicely, it lacks a plane of symmetry, a centre of symmetry, and any $4n$-fold inversion axis, according to

[7] Lakes states that an even rank tensor is inherently inversion-symmetric and hence cannot capture chiral phenomena [115].

[8] According to Eringen, chirality can be interpreted as a manifestation of nonlocality [116].

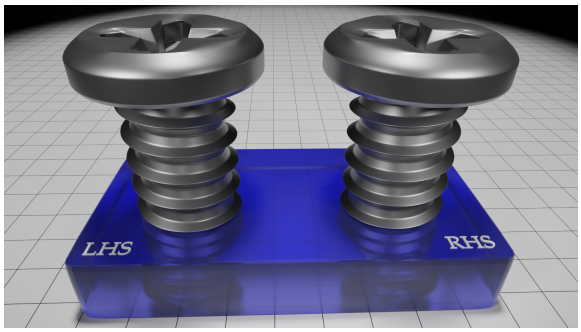

Figure 5.5: Example for chirality. A render of two screws embedded in a slab. The screws differ by their thread pitch. The left screw is left handed (LHS) and the right screw is right handed (RHS). The screws cannot be made congruent with each other using simple translations or rotations. A mirror operation is necessary. Thus, they are chiral objects.

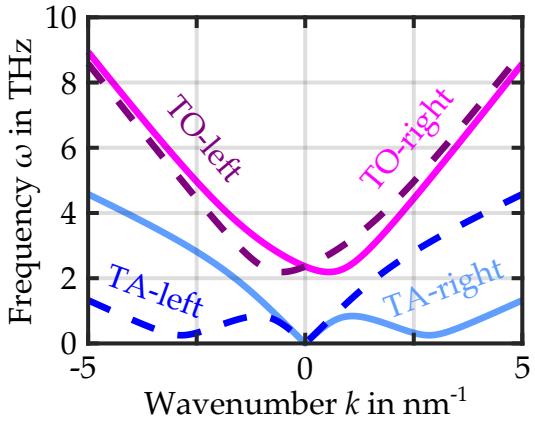

Figure 5.6: Elastic-wave (or phonon) dispersion in a chiral crystal. The transverse acoustic (TA) and optic (TO) are plotted for the left handedness (dashed lines) and right handedness (solid lines), respectively. The lowest bands show roton-like dispersion. The exact trend of the bands depends on the chosen values for the material parameters. In this example, the values from Kishine et al. were used [27].

Whyte. Very common examples of such objects are human hands[9] or the thread of mechanical screws, see Figure 5.5.

For elastic metamaterials, the interest in chirality induced effects such as acoustical activity, the counterpart to optical activity, was only recently rekindled. In part, by the work of Tobias Frenzel et al. in 2019 [13]. Following this upcoming field, Kishine et al. used micropolar elasticity to predict a roton-like dispersion relation in a chiral metamaterial. Their core idea is based on chirality lifting the degeneracy of transverse acoustic (TA) and transverse optical (TO) bands, respectively. The splitting of the TA bands is the manifestation of acoustic activity [120]. Furthermore, the minimum of the TO bands is shifted away from $k = 0$ generating a region of negative group velocity for the TO-modes. Hybridization of a TO-right handed band with a TA-right handed band leads to an anti-crossing, and the bands become hybridized. In other words, the negative group velocity behavior of the optical modes becomes admixed into the acoustical modes. For sufficiently large coupling of the bands, a roton-like dispersion ensues. Calculated bands following Kishine et al. are plotted in Figure 5.6. Both, the shift of the TO-band minima away from $k = 0$, as well as the roton-like dispersion for the TA bands are visible.

[9] "Chiral" is derived from the Greek word for "hand". (Wikipedia on the 20th of September 2023).

Remark on Micropolar Elasticity

As aforementioned, a chiral material cannot be described by Cauchy-elasticity and as such cannot provide effective material parameters. Eringens micropolar elasticity expands Cauchy-elasticity with additional rotational degrees of freedom. Hence, a material is said to be made up of points, which also can rotate around all three normal axis. These degrees of freedom require the introduction of additional tensorial quantities. For deformation, the curvature tensor κ_{ij} and for stresses, the couple-stress tensor m_{ij} must be introduced. The constitutive law (similar to Hooke's law) is derived in the linear elastic regime from the principle of conservation of energy and leads to an effective elastic matrix with 9×9 components. For the interested reader, a rigorous description of micropolar elasticity is given in Eringens work [110, 111, 116]. A micropolar description of chiral metamaterials is introduced by Yi Chen et al. in [121] and replicated in part within the supporting material of [45].

5.3.2 *Exploiting Extreme Chiral Couplings*

While the authors of [27] nicely predicted the possibility of roton-like dispersion in a chiral material, no architecture or structure of a metamaterial unit cell was proposed. However, it was made clear that chirality is a necessity but by far no guarantee to observe roton-like behavior. The material parameters must be carefully taylored, in order to introduce sufficient coupling and admixture of optical and acoustical bands. The core idea governing the following design is to split both optical and acoustical bands of a metamaterial crystal due to chirality and admix the aforementioned negative group velocity behavior of optical modes into acoustical ones.

A structure designed by my aforementioned colleagues which can fulfill this criteria is shown as a blue print in Figure 5.7. In principle, the material design is based on an arrangement of cubes (yellow) with side-length L imposed onto a simple cubic translation lattice[10] with lattice constant a. Naturally, these cubes have three translational and three rotational degrees of freedom. The crucial part lies in the nature of the coupling rods (blue) between the cubes of adjacent unit cells. These rods form chiral connections, not only between nearest neighbours, but also between neighbours along the face-diagonals. One such chiral coupling is highlighted in red in Figure 5.7(b). As a consequence, the unit cell has three axes with fourfold rotational symmetry (face normals), four axes with threefold rotational symmetry (body diagonals), no center of inversion, no mirror planes, and no rotation-reflection symmetries [45].

[10] Kishine et al. considered tetragonal crystal symmetry. Here, cubic symmetry was chosen.

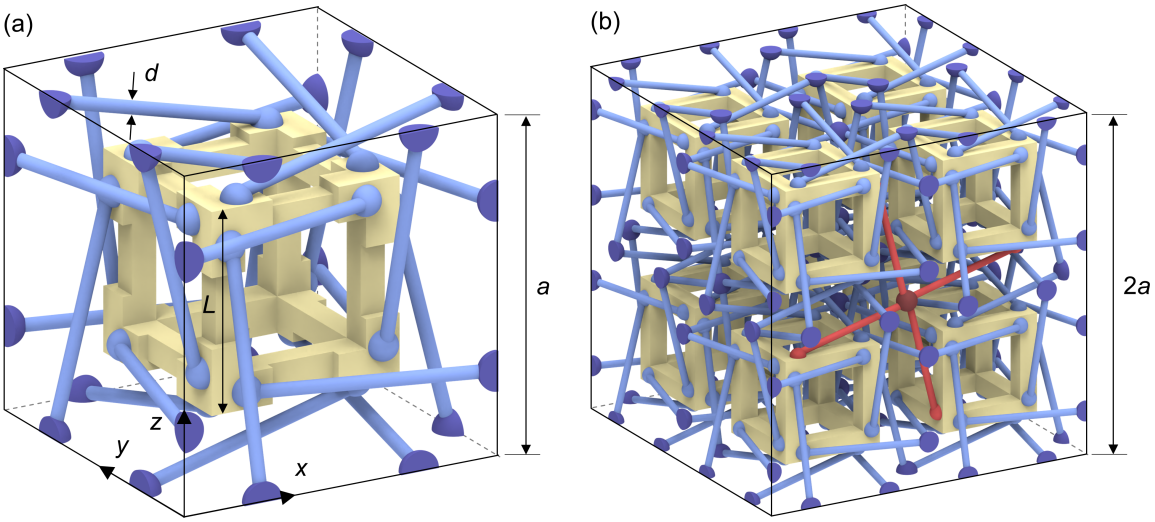

Figure 5.7: Blue print of the unit cell for the chiral roton metamaterial. Coloration is for visualization only. (a) Single unit cell with lattice constant a. A hollowed-out cuboid (yellow) with side length L is at the center of the unit cell. In total, 24 cylindrical rods (light blue) with diameter d are connected to the cuboid by 24 half-spheres (light blue) at one end. At the other end, they merge into 24 quarter-spheres (dark blue). The unit cell features no mirror symmetries, but all rotational symmetries of a cube. (b) A small metamaterial crystal assembled from $2 \times 2 \times 2$ unit cells. One of the extreme chiral couplings between unit cells is highlighted (red) for clarity. Those couplings arguably convey a weak form of nonlocality, since they connect not only neighboring unit cells, but also unit cells along the face diagonals of the underlying translation lattice. Figure and caption taken from [45] and adapted under (CC BY 4.0), published by Adv. Func. Mat. 2023.

Furthermore, it is those connections that couple translational degrees of freedom of the cubes to rotational ones. This ultimately leads to the required admixture of optical and acoustical bands. This can be verified by inspecting the mode shapes of TA and TO bands at small wavenumbers k, respectively. As described in [45], the TA bands feature circular polarized modes that are dominated by translations of the cubes. The TO bands on the other hand mainly show rotations of the cubes. For larger k, the TO and TA bands hybridize and roton-like dispersion manifests in the lowest band. The corresponding modes in the negative group velocity region now feature simultaneous translation and rotation of the cubes, a somewhat intuitive result.

The critical parameter dictating the degree of admixture and hence the "depth" in frequency of the roton-like minimum is the coupling rod diameter d. This geometric parameter is directly linked to the previously mentioned careful tailoring of the resulting effective material parameters in order to obtain roton-like dispersion through chirality. Conceptually, for $d/a \to 0$ the minimum would

approach zero frequency. Yet such a structure is impossible to fabricate and mechanically unstable. Conversely, finite-element calculations predicted, that for too large values of d, the roton-like behavior vanishes. For the following fabrication of metamaterial-beam samples, this poses a significant challenge. The coupling rods must be thin enough to ensure roton-like dispersion and at the same time be stiff enough to support the structure during and after printing.

The Fabricated Metamaterial Sample

For fabrication via laser microprinting, a hatching distance of $d_{\text{hatch}} = 200\,\text{nm}$, and slicing distance of $d_{\text{slice}} = 300\,\text{nm}$ were chosen. The laser power was set to 27.5 mW and a laser focus scan speed (focus velocity) of $0.145\,\text{m}\,\text{s}^{-1}$ was used. The bottom plate was again written using a laser power of 50 mW, scan speed of $0.140\,\text{m}\,\text{s}^{-1}$ as well as $d_{\text{hatch}} = 0.5\,\mu\text{m}$, and $d_{\text{slice}} = 1.5\,\mu\text{m}$.

The sample fabrication proved to be remarkably challenging and took almost a full year of tedious iterative optimization[11]. The reason for this was the vast number of fine and overhanging parts in the unit cell (cf. Figure 5.8(c)). Especially the slender rods with diameter d are only connected on one end at certain times during the printing process. Therefore, they may drift away or bend even during the time they are printed. A sophisticated printing and sample development strategy had to be designed, to counteract and minimize these defects. The most noteworthy is the "laying-down" of the beam onto the substrate. This means, they were printed with their axis parallel to the plane of the substrate, instead of normal to it.

To remove the samples non-destructively from the substrate, the latter was spin coated with a sacrificial layer of polyvinyl alcohol (PVA) with $\approx 150\,\text{nm}$ thickness. After printing and washing-away of the unpolymerized resist with two subsequent baths in PGMEA and ethanol respectively, the sacrificial layer was dissolved in hot water, detaching the sample. No critical point drying was employed, instead, the samples were air dried in ambient laboratory conditions. A gallery of a metamaterial beam fabricated in such a way is shown in Figure 5.8. The sample consists of $3 \times 3 \times 40$ unit cells (x, y and z) and thus forms a beam with. The lattice constant is $a = 185\,\mu\text{m}$ and (coupling) rod diameter is $d \approx 7.5\,\mu\text{m}$.

[11] The latter was at the core of the Masters thesis of Jonathan Schneider.

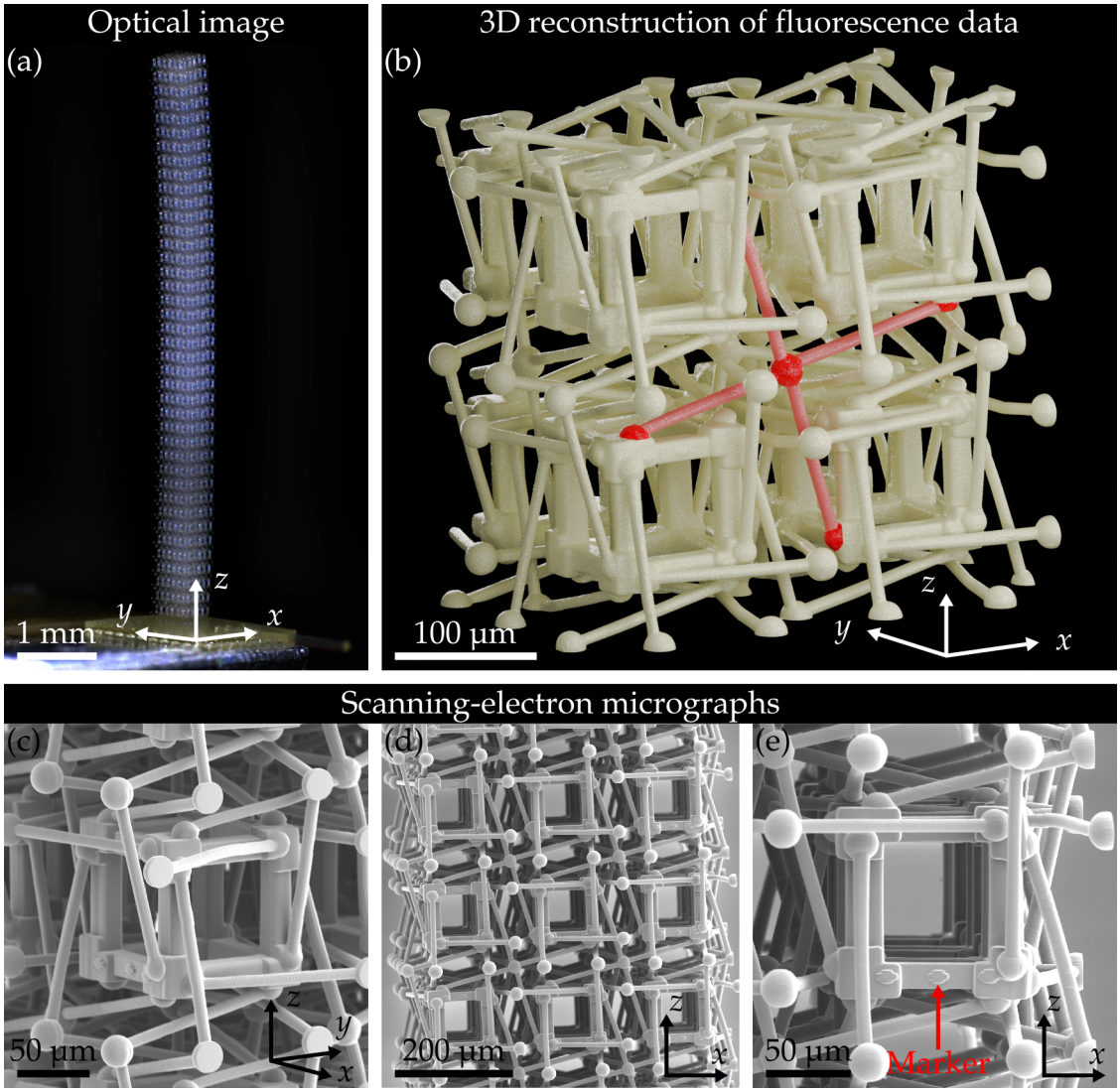

Figure 5.8: Showcase of the microscale metamaterial sample with extreme chiral couplings. (a) Wide-field optical micrograph presenting an overview of a printed polymer sample, comprised out of $3 \times 3 \times 40$ unit cells (for x, y and z). (b) 3D iso-intensity surface acquired with a confocal fluorescence microscope (LSM800, Zeiss) from the autofluorescence of the polymer. Similar to Figure 5.7(b), an extreme chiral coupling is highlighted (red). (c,d,e) Side-view scanning-electron micrographs of a beam sample. (c) Close-up oblique view onto a single unit cell of a beam sample. Several rods are slightly bend, which is a consequence from fabricating overhanging parts with 3D laser microprinting. (d) View through the side of a beam sample, showing 3×3 unit cells at the surface. This viewing angle is convenient to inspect for defects or falsely connected parts due to the proximity effect. (e) Zoom-in on the bottom right unit cells from (d). The arrow (red) points towards one of the cross-shaped markers used for tracking with DIC analysis. Figure and caption taken from [45] and expanded under (CC BY 4.0), published by Adv. Func. Mat. 2023.

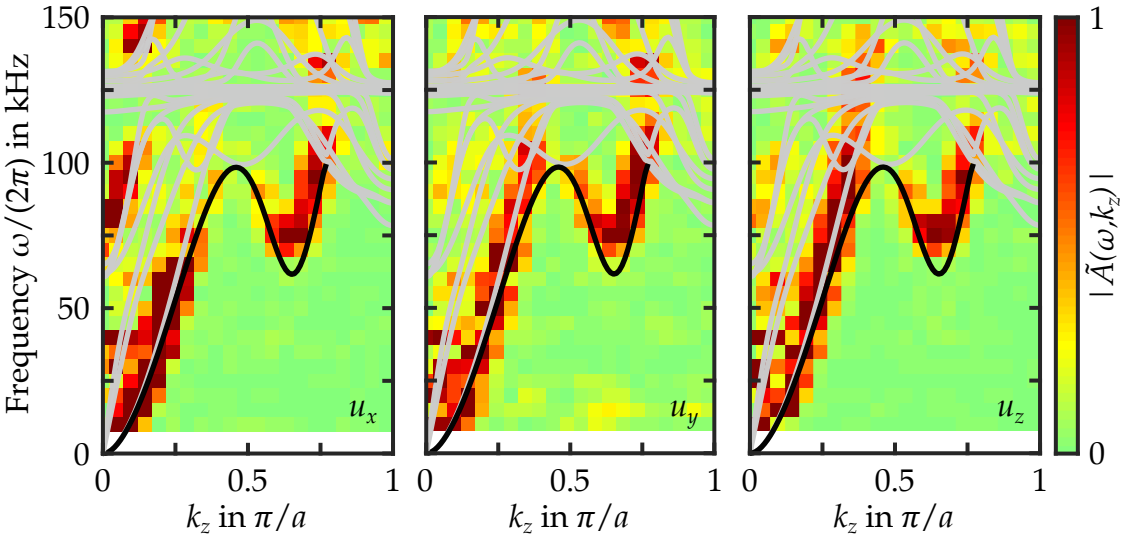

Figure 5.9: Experimental dispersion relation results for the chiral metamaterial-beam sample. In analogy to Figure 5.4(a), the dispersion relation is obtained by Fourier transform with respect to space of the displacement-vector-component amplitude distribution (amplitude envelope) for every excitation frequency. The results are again depicted as false-color plots of $|\tilde{A}(\omega, k_z)|$. Bands are visible by following the false-color maxima. The panels are labeled with the according displacement-vector component (u_x, u_y and u_z), from which they were derived of. Due to the symmetry of the metamaterial structure, the dispersion relation derived from each of the three displacement-vector components reveals the roton-like dispersion in the lowest band. The solid lines are numerically calculated bands using finite-element analysis for an infinite beam along z and a 3×3 cross-section. The lowest band is emphasized in black. In the chosen coordinate system, the beam axis aligns with the z-direction. Thus, the u_x and u_z components were measured with DIC analysis (in-plane) while the u_y component was measured with vibrometry (out-of-plane). Figure and caption taken from [45] and adapted under (CC BY 4.0), published by Adv. Func. Mat. 2023.

Band-Structure Measurements

To measure the band structure for the chiral metamaterial-beam samples, we conducted similar experiments as already described in Section 4.3.3 and Section 5.2. The displacement field of elastic waves propagating along the beam z-axis was sampled on 41 ROI. The zeroth ROI was positioned on the bottom plate to survey the displacement excitation. The residual 40 ROI were spaced by the lattice constant a and centered on cross-shaped markers (cf. Figure 5.8(e)). For this project, the laser-Doppler-vibrometry branch was included in the experimental setup (cf. Figure 4.7. Therefore, displacement-vector-component amplitude distributions (amplitude envelopes) for all three spatial directions were measured.

The investigated excitation frequency range was 10 kHz to 150 kHz with 5 kHz increment i.e. temporal frequency resolution. ROI size and pixel size were identical as given in Section 5.2. For each ROI and frequency, 2048 images were acquired for DIC analysis. For laser-Doppler vibrometry, 2^{19} data points as described in Section 4.3.3 were acquired. The displacement vector amplitudes were extracted for each ROI from the raw data using discrete fast Fourier transformation (FFT) with respect to time as mentioned in Section 4.3.2. To prevent spectral leakage, the raw-displacement data was truncated to yield a FFT resolution of an integer fraction of the excitation frequency[12]. To do so, $u_x(\mathbf{r}, t)$ and $u_z(\mathbf{r}, t)$ raw data was truncated from 2048 to 2000 points to provide a FFT resolution of 5 kHz. For $u_y(\mathbf{r}, t)$ the raw data was truncated from $2^{19}/64 = 8192$ to 6250 data points, equating to a resolution of 1.25 kHz. Lastly, the obtained amplitude envelopes were Hann-windowed and Fourier transformed with respect to real space to assemble the band structure for elastic waves (i.e. phonons) propagating along the z-axis.

The experimental results are collected in Figure 5.9. For the lowest band showing roton-like dispersion, a significant peak-to-valley ratio of $\omega(k_{\text{min}})/\omega(k_{\text{max}}) \approx 0.63$ was achieved. Thus a broadband region of negative group velocity was created. Solid lines are bands computed from finite-element analysis for an infinite beam with 3×3 unit-cell cross-section. In the computations, a Young's modulus of $E = 4.19\,\text{GPa}$, a Poisson's ratio of $\nu = 0.4$ and a mass density of $\rho = 1140\,\text{kg}\,\text{m}^{-3}$ were chosen for the constituent polymer.

The region in the lowest band showing the targeted dispersion is emphasized in black. Higher bands, depicted in gray, originate either from local resonances in the material or a large number of back-folded bands as a consequence of the finite beam cross-section. Overall, an excellent agreement between the theory and the experiment was achieved. For comparison of the experimental data with finite-element calculations for finite beam sample (cf. Figure 5.4(b)), the reader is referred to supporting information of publication [45]

[12] Considering the (effective) sample rates of imaging and vibrometry, respectively.

Summary

In this project, based on the prediction of possible roton-like dispersion by Kishine et al., a chiral microscale metamaterial was designed and fabricated. The roton-like dispersion resulted from carefully designed admixture of the chirality-split optical and acoustic bands. This behavior was observed in the experiment for waves propagating along the axis of finite metamaterial-beam samples. Due to the symmetry of the unit cell, this roton-like behavior is predicted to occur for waves propagating along the other principal directions as well, given sufficient sample size along those directions. To the date of the corresponding publication [45], this was arguably the first demonstrations in how to achieve roton-like dispersion through different means than beyond-nearest-neighbor interaction.

Furthermore, due to the use of the laser-Doppler-vibrometry branch, all three displacement-vector components could be measured simultaneously. Thus, the roton-like band could be easily reconstructed from all three displacement-vector components without reorienting the sample in the setup.

Chapter 6

6 Extremal Cauchy-Elastic Materials

Within this Chapter, I report my experiments on extremal Cauchy-elastic materials, namely Tetramode and Monomode metamaterials. This designation follows the proposition of Milton and Cherkaev [28] in their work from 1995. In order to explain the nomenclature, I briefly summarize their definition and outline the most important properties of such materials. Subsequently, I report my experiments on a finite Tetramode metamaterial, where the material acts as a polarizer for transverse elastic waves (phonons). Afterwards, I address my experiments on Monomode metamaterial-beam samples. As in the previous Chapter, a roton-like dispersion is achieved. Here however, the single soft-mode of the material is hybridized exploiting an intricate back-folding strategy. The results of the experiments on both materials were previously published [92, 122].

6.1 Definition and Properties

The generalized Hooke's law in three dimensions links the deformation response of a material to the loads applied onto it. As has been summarized in Chapter 2, for linear elasticity, several symmetries can be exploited to vastly reduce the number of independents in the stiffness tensor $\mathbf{C}$. Subsequently, the tensor reduces to a 6×6 matrix in Voigt-notation [29, 123] (cf. Equation 2.27). Inherently, for this case, six eigenvalues of $\mathbf{C}$ can be found, each of which belong to a orthogonal mode of deformation. Due to the orthogonality, each of these eigenvalues can independently be zero. Each vanishing eigenvalue corresponds to a so-called "soft" mode of deformation. In the static case, such a mode conceptually requires zero force or energy to induce. Consequently, for dynamic elastic waves, this corresponds to wave-velocities lying at strictly zero frequency (cf. Equation 2.37).

In the year 1995, Milton and Cherkaev used this attribute of vanishing eigenvalues to define extremal Cauchy-elastic materials [28]. Furthermore, they suggested to name materials according to the number of these vanishing (or in practise extremely small with respect to the other) eigenvalues[1]. Numbering the modes (or vanishing eigenvalues) with $N = 1, 2, 3, 4, 5, 6$ yields $N = 1$ Monomode, $N = 2$ Dimode, $N = 3$ Trimode, $N = 4$ Tetramode, $N = 5$ Pentamode and $N = 6$ Hexamode materials.

In practise, it is possible to engineer approximates of such materials as metamaterials using a smart arrangement of bodies, connected by small hinges or joints. To achieve an ideal extremal metamaterial, those hinges need to be ideal in the sense that they dissipate no energy and require no force to actuate. Only then can the metamaterial feature a truly "soft" mode i.e. have one or more vanishing eigenvalues of $\mathbf{C}$. In reality, this usually is equivalent with a geometric parameter, i.e. a connection-point diameter d to go to zero. Naturally, this is not possible to fabricate, as such metamaterials would just fall apart. Thus, all fabricated instances of an extremal Cauchy-elastic metamaterial will represent approximations with a finite d.

Along these lines and following the suggestions of Milton and Cherkaev [28], a Pentamode metamaterial using double-cone elements connected at their tips was demonstrated on the microsscale [12] in 2012. Such a material is only stable under hydrostatic pressure which is accompanied by extreme ratios of the bulk modulus K to shear modulus G (cf. Equation 2.31 with $B/G \approx 1000$ [124]).

In [12], the Pentamode character of the material was validated by numerical calculations calibrated to the geometric parameters of the fabricated samples. Experiments on macroscale [124] and microscale [17] samples were supplemented shortly after in 2013 and 2014, respectively.

[1] Their original work used a mixture of Latin and Greek numbering, here we decided to stick to Greek number words.

In the experiments from 2014, the Pentamode metamaterial was used as an acoustic cloak, i.e. shielding an object from forces applied upon a layer of pentamode metamaterial. This property attracted considerable attention in the field of seismic wave protection [125]. Moving forward, it is naturally worthwhile to further investigate the interesting extremal elastic properties of such materials to tailor wave-propagation. Two experimental implementations of such tailoring are addressed in the following sections.

6.2 Polarizing Elastic Waves using a Tetramode Metamaterial

As aforementioned, a Pentamode metamaterial was used as an acoustic cloak, shielding an object from the displacement field induced by external forces [17]. Experiments were conducted quasi-statically (force loading on the order of seconds).

This raises a maybe relatively naive but to some intuitive question. If the displacement field can be controlled in such a way, that it is directed somewhat "around" a structure, then maybe there is also the possibility to selectively suppress only certain displacement polarizations?

A theoretical study from 2012 provided the answer to that question by band-structure calculations for elastic waves (phonons) in a pentamode metamaterial [126]. It was shown that for certain wave propagation directions through the material, a suppression of (transverse) shear-waves is predicted. Hence, out of three possible displacement-field polarizations for elastic waves in mechanics, only the longitudinal one is preserved[2].

This shows that the idea to use extremal Cauchy-elastic materials as polarizers for elastic waves is not new. However, a polarizer for a single transversely polarized wave, i.e. the counterpart to a wire-grid polarizer[3] in optics [127], remained absent. Here, I report my experimental demonstration of such a transverse and broadband elastic-wave polarizer, formed from a Tetramode metamaterial which was published in [92].

6.2.1 Unit-Cell Design and Elastic Properties

The underlying unit-cell design of the Tetramode metamaterials was based on the suggestion of Yu Wei et al. [92]. In principle, two geometrical elements are used to build the unit cell of tetragonal symmetry. Double-cones of central diameter D are joined at their tips using half-spheres of radius r.

[2] The polarization refers to the orientation of displacement field $\mathbf{u}(\mathbf{r}, t)$ to wavevector $\mathbf{k}$

[3] It is legitimate to view such a polarizer as a two dimensional metamaterial.

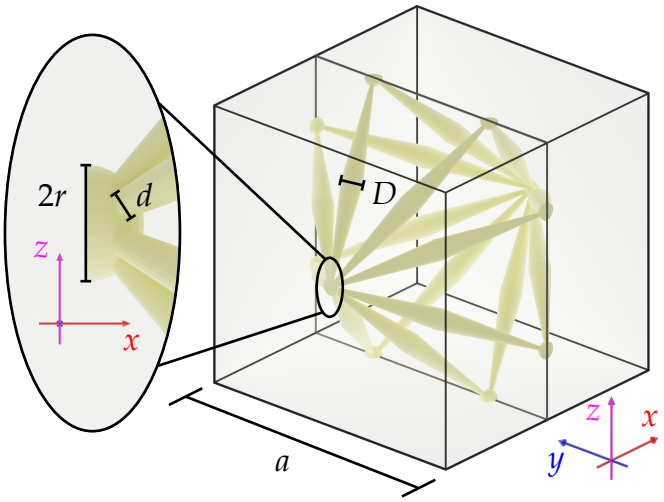

Figure 6.1: Blue print of Tetramode unit cell with lattice constant a. Design parameters for the double-cones are the central diameter D and the critical diameter d, where they are merged into the half-spheres (inset) with radius r. Figure and caption based on [92] under (CC BY 4.0), published by Adv. Mat. 2023.

The blue print of the unit cell is rendered in Figure 6.1. It is those spheres that represent the modification undertaken from the original designs suggestion. Without those spheres, the critical geometrical parameter of the structure would be the diameter of the tip-connections of all double-cones. Such a structure however is extremely sensitive to imperfection during printing and thus challenging to fabricate. Introduction of the spheres eases this process and assists in obtaining a well-defined geometry. The critical geometric parameter of this unit cell is now the ideally circular connection with diameter d of the double-cones and spheres. It is the thickness d that directly influences the shear-stiffness of the material and how little the joints resist to external loading by forces. A metamaterial crystal of tetragonal symmetry is formed by imposing the unit cell onto a simple-cubic translation lattice with lattice constant a.

The response of the material to external loads can be summarized as follows. Due to the unit-cell geometry, the material can efficiently withstand a shear load $\sigma_{zx} = \sigma_{xz} \neq 0$ (equivalently due to symmetry $\sigma_{yx} = \sigma_{xy} \neq 0$) with little deformation. The occurring forces can be decomposed into components along the center axis of the double-cones, along which they are stiff. Consequently, the material appears "hard" and shows little deformation. For all other (shear or normal) loading conditions, such a decomposition is not possible and the connections between spheres and double-cones yield, effectively acting as hinges. Thus, the material appears compliant i.e. "soft" and deforms more. This mechanism is further illustrated in the supporting information of [92].

Widening this conceptual understanding of the unit-cell mechanism to an infinitely expanded bulk structure, was performed by my co-authors Yu Wei and Yi Chen. In their numeric simulations using finite element analysis in COMSOL, several ratios of d/a were investigated [92].

(a)

$d = 4\,\mu\text{m},\ D = 16\,\mu\text{m},\ a = 200\,\mu\text{m}$

$\mathbf{C}_{\text{eff}}$ / MPa =

$$\begin{pmatrix} 0.14 & 0.06 & 0.06 & 0 & 0 & 0 \\ & 0.07 & 0.00 & 0 & 0 & 0 \\ & & 0.07 & 0 & 0 & 0 \\ & & & 0.01 & 0 & 0 \\ & \text{sym} & & & 6.21 & 0 \\ & & & & & 6.21 \end{pmatrix}$$

$\mathbf{V}$/MPa = $(0.02\ 0.07\ 0.19\ 0.01\ \mathbf{6.21}\ \mathbf{6.21})^{\text{T}}$

(b)

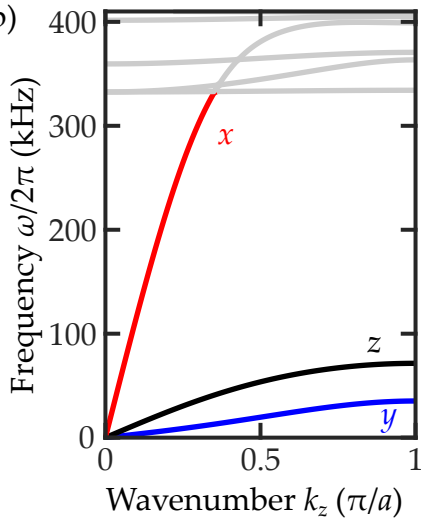

Figure 6.2: Static and dynamic properties of the Tetramode metamaterial. (a) Geometric parameters targeted for fabrication are given. $\mathbf{C}_{\text{eff}}$ is the calculated effective elasticity matrix $\mathbf{C}_{\text{eff}}$ derived from the phase velocities in the long-wavelength limit (cf. supporting information of [92]). The eigenvalues are listed in $\mathbf{V}$. Two of which, emphasized in bold-face, are at least one order of magnitude larger than the remaining four. Thus, the materials is Tetramode. (b) Corresponding band-structure-calculation results for an infinite bulk and waves propagating along the z-direction with wavenumber k_z. Three bands emerge, which are labeled according to their dominant displacement-field polarization. The x- and y-polarized modes are transverse waves, while the z-polarized mode is longitudinal. Figure and caption taken from [92] and expanded under (CC BY 4.0), published by Adv. Mat. 2023.

Conceptually, when $d/a \to 0$, the joints become ideal and the material would exhibit ideal Tetramode behavior. Obviously, some compromise must be made in order to arrive at a geometry fit for fabrication. Given the finite voxel size in printing as a fundamental constraint, we arrived at the targeted geometric parameters of $a = 200\,\mu\text{m}$, $d = 4\,\mu\text{m}$, hence $d/a = 0.02$.

The corresponding effective stiffnes matrix $\mathbf{C}_{\text{eff}}$ is given in Figure 6.2(a), together with its respective eigenvalues. Two out of the six eigenvalues are at least one order of magnitude larger than the remaining four[4], making this metamaterial Tetramode in unison with Miltons and Cherkaevs definition. The stiffness matrix was derived in the long-wavelength limit from finite-element band-structure calculations, the results of which are depicted in Figure 6.2(b). To arrive at these results, $E = 4.19\,\text{GPa}$, $\nu = 0.4$ and $\rho = 1190\,\text{kg}\,\text{m}^{-3}$ were chosen for the Young's modulus, Poisson's ratio and mass density of the constituent polymer, respectively.

[4] For $d/a \to 0$ the four small eigenvalues would tend to zero.

In regard of the experiments, it is sufficient to only discuss waves propagating along z-direction with wavevector $\mathbf{k} = (0, 0, k_z)^{\mathrm{T}}$ within the first Brillouin zone. This direction of wave propagation is chosen in the experiments reported below. In total, three bands are present. Two bands correspond to transverse (shear) modes, namely modes with x-polarized (red) and y-polarized (blue) displacement fields. The third band corresponds to longitudinal i.e. z-polarized modes (magenta). The bands differ significantly in their slope and thus the frequency region $f = \omega/(2\pi)$ they cover in the first Brillouin zone. Therein lies the key point of the material. Over a broad frequency region, between roughly 80 kHz and 320 kHz, only x-polarized elastic waves can propagate. Waves featuring y- and z-polarization become evanescent and are thus suppressed[5]. This polarization sensitive discrimination gives rise to the polarizer behavior of the sample. In contrast to the Pentamode metamaterial from [126], only one of the two (transverse) polarizations as well as the longitudinally polarization are suppressed.

6.2.2 *The Fabricated Sample*

For the experiments, finite samples with $9 \times 6 \times 6$ unit cells (along x, y, z) were fabricated using 3D laser microprinting. The number of unit cells was chosen as a compromise between expected polarizer action and fabrication time of ≈ 12 h. Optimization of the sophisticated writing strategy was done by Jonathan Schneider. A showcase of such a finite sample and its unit cell is given in Figure 6.3. Again, an iso-intensity surface reconstructions was acquired using the auto-fluorescence of the polymer to demonstrate the high sample quality. Since the performance of the sample relies heavily on the critical parameter d, we measured this parameter on fabricated samples. However, it is unwise to do so from an iso-intensity surface, as the latter strongly depends on the chosen treshhold value for reconstruction. Thus, the scanning-electron micrographs (cf. Figure 6.3(c)) were used to verify the intended magnitude of $d = 4\,\mu$m.

A residual asymmetry in the intended sphere-shape of the connections between adjacent unit cells remain. We attribute this to the elliptical shape (extended along the z-axis) of the printing voxel. With the used resist system, we arrived at the limit of the possible voxel-compensation without jeopardizing the sample integrity. Alternatively, a different resist system like the Microfabrication Solution Set Small Features (3D SF, Nanoscribe) instead of Microfabrication Solution Set Medium Features (3D MF, Nanoscribe) could be used. This would potentially allow for even smaller ratios of d/a. However, using the 3D SF may escalate printing times tremendously. The reason for that being the vastly reduced writing field by factor of two compared to the 3D MF.

[5] For $d/a \to 0$, the corresponding bands would lie at strictly zero frequency.

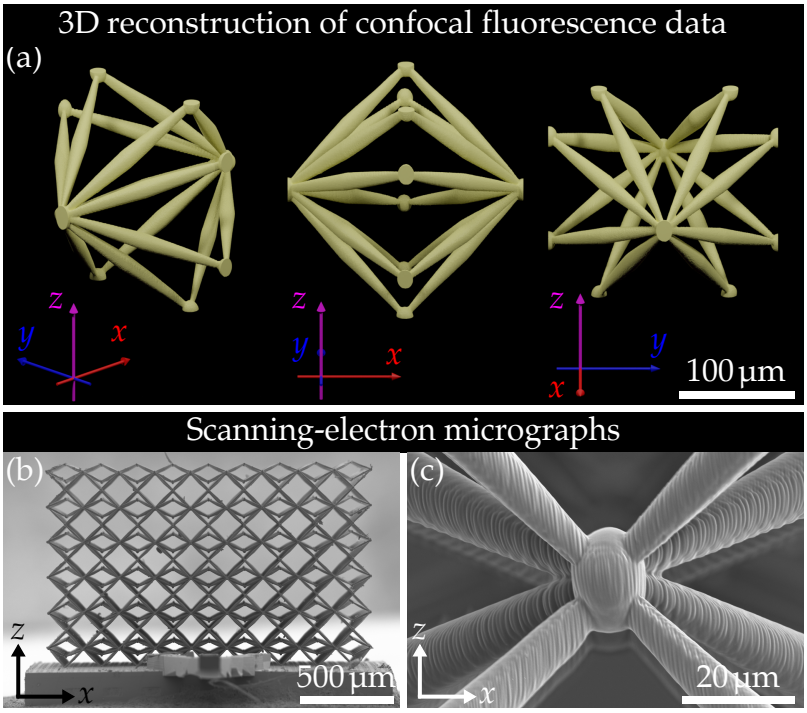

Figure 6.3: Showcase of the Tetramode metamaterial sample features. (a) Reconstructed 3D iso-intensity surfaces from a single unit cell under different viewing angles. Data acquired with a confocal fluoerscence microscope (LSM800, Zeiss). Coloration and tripods added in Blender. (b) Side-view of a sample comprised of $9 \times 6 \times 6$ unit cells (along x, y, z) on its bottom plate. (c) Connection between two adjacent unit cells. Due to the shape of the voxel during printing, the intended sphere-shape is elongated along z, forming an ellipsoid. Figure and caption taken from [92] and expanded under (CC BY 4.0), published by Adv. Mat. 2023.

Consequently, even a different writing strategy may be required to fabricate adequate samples. Thus, we chose to account for those imperfections in the numerical simulations instead to verify the persistence of the polarizer action.

For fabrication with the commercial printer (PPGT, Nanoscribe) a hatching distance of $d_{\text{hatch}} = 300\,\text{nm}$, and slicing distance of $d_{\text{slice}} = 500\,\text{nm}$ were chosen. The focus velocity (scan speed) was set to $0.110\,\text{m}\,\text{s}^{-1}$, and a laser power of 37.5 mW was used. Again, a bottom plate was included at one end of the samples to facilitate sample manipulation. The plate was printed at a laser power of 50 mW, scan speed of $0.140\,\text{m}\,\text{s}^{-1}$ as well as $d_{\text{hatch}} = 0.5\,\mu\text{m}$, and $d_{\text{slice}} = 1.5\,\mu\text{m}$[6]. To rid the samples of unpolymerized resist, they were submerged in a bath of propylene glycol methyl ether acetate for a minimum of 30 min, followed by a 5 min rinse in acetone. The latter was finally removed using critical-point drying in CO_2.

[6] Parameters and writing strategy can be deduced from the repository published with [92].

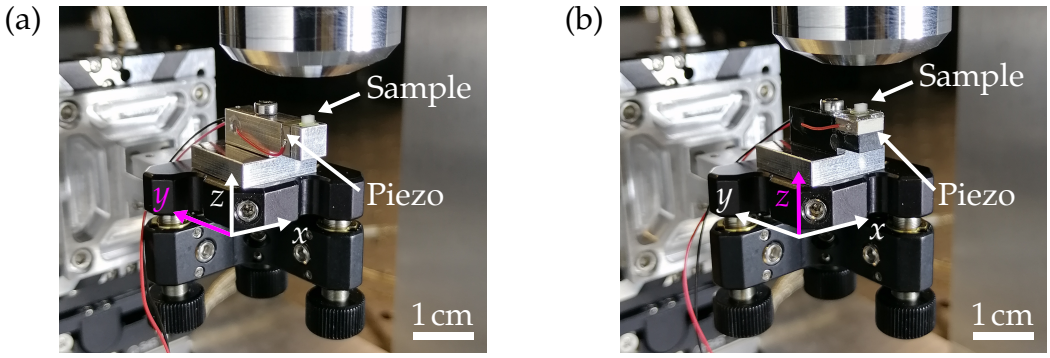

Figure 6.4: Photographs of two Tetramode metamaterial samples in the experimental setup. (a) The sample is coupled to a piezoelectric transducer (cf. Figure 4.11). To orient the transducer axis along the y-direction (magenta), an aluminum cuboid is used as an elbow piece. The transducer can be identified by the emerging cables, through which it is driven with a voltage to excite elastic waves. Below, a three-axis tilt platform can be used to align the sample with the focal plane of the microscope objective lens. (b) Similar to (a), but with the transducer axis aligned with the z-direction (magenta). To achieve this orientation, a silica glass substrate is glued onto the transducer, before the sample is glued onto the silica glass. Figure and caption modified from [92] under (CC BY 4.0), published by Adv. Mat. 2023.

6.2.3 *Measuring the Polarizer Action*

The general idea of the experiment can be summarized with few words. In order to characterize the polarizer performance, elastic waves of arbitrary polarization need to be coupled into the sample. Subsequently, the displacement field of those waves has to be tracked at designated input and output locations. The component-wise amplitude-ratio of input displacement-vector components to output displacement-vector components reveals which displacement polarization is supported or suppressed. Sweeping the excitation frequency over a broad frequency range indicates the frequency dependence of this polarizer action.

Elastic waves were excited within the sample by coupling them to a piezoelectric transducer, see Figure 4.11. The latter was driven with a time-harmonic voltage, as described in (Section 4.3.1). At ultrasound frequencies, the transducer shows nonzero displacements along all three spatial directions $\mathbf{u}(\mathbf{r},t) = (u_x(\mathbf{r},t), u_y(\mathbf{r},t), u_z(\mathbf{r},t))^{\mathrm{T}}$, which provides the desired arbitrary input-wave polarization (cf. Figure 4.13). Nonetheless, for the experiments two configurations were chosen to maximize the displacement input that is polarized along directions of strong suppression i.e. where a small displacement is expected at the output. Those configurations are shown in Figure 6.4, where two samples are installed in the setup. For showing a strong suppression for say the u_y displacement-vector

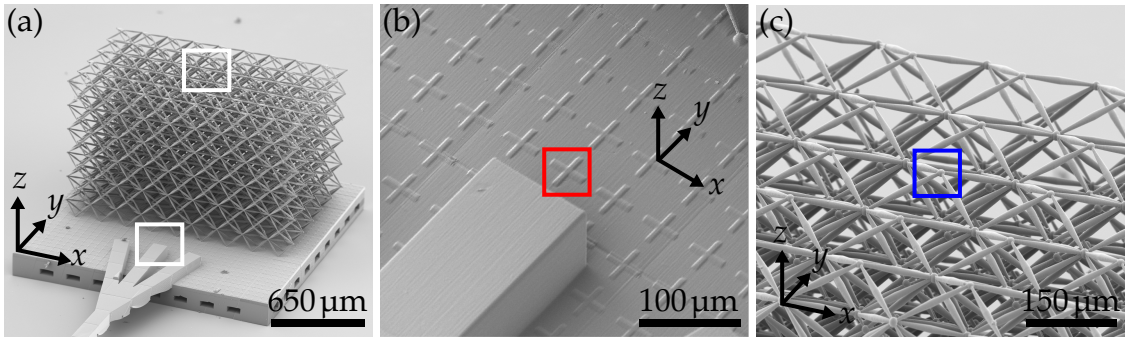

Figure 6.5: Scanning-electron micrographs of polarizer input and output locations. (a) Oblique-view of a sample with bottom plate. The regions enclosed by white rectangles are magnified in the following panels. (b) Magnified view of the lower white rectangle of (a). The red square on a cross-shaped marker highlights the position designated as displacement "input" to the Tetramode metamaterial sample. (c) Magnified view of the upper white rectangle of (a). The blue square positioned on a half-sphere marks the position designated as displacement output. The position is chosen in the top middle of the sample to stay away from edge-effects which deteriorate the polarizer performance. Figure and caption taken from [92] and expanded under (CC BY 4.0), published by Adv. Mat. 2023.

component, it is beneficial to start out with a large displacement amplitude along the y-direction. This in mind, in Figure 6.4(a) the transducer axis points along the y-direction and in Figure 6.4(b) respectively along the z-direction. To calculate the displacement ratio, the time-dependent displacement-vector components were measured on cross-shaped markers on the bottom plate (input), and at the top center of the sample (output). Figure 6.5 highlights those locations. The output location was deliberately chosen to be as far away as possible from the edges of the sample. A finite sample exhibits significant edge effects that deteriorate the polarizer action due to numerous back-folded bands.

For both sample configurations, u_x and u_y were measured with DIC analysis, while u_z was measured with laser-Doppler vibrometry. To compute the displacement ratio, the displacement-vector-component amplitudes were extracted using Fourier analysis of the raw-data as explained in Section 5.3.2. The excitation frequency was incremented from 0 kHz to 300 kHz in steps of $\Delta f = 10\,\text{kHz}$. We observed that for a displacement input

$$\mathbf{u}_{\text{in}}(\mathbf{r}, t) = (u_x(\mathbf{r}, t), u_y(\mathbf{r}, t), u_z(\mathbf{r}, t))^{\text{T}} ,$$

only the x-component remains, such that

$$\mathbf{u}_{\text{out}}(\mathbf{r}, t) = (u_x(\mathbf{r}, t), u_y(\mathbf{r}, t) \approx 0, u_z(\mathbf{r}, t) \approx 0)^{\text{T}}.$$

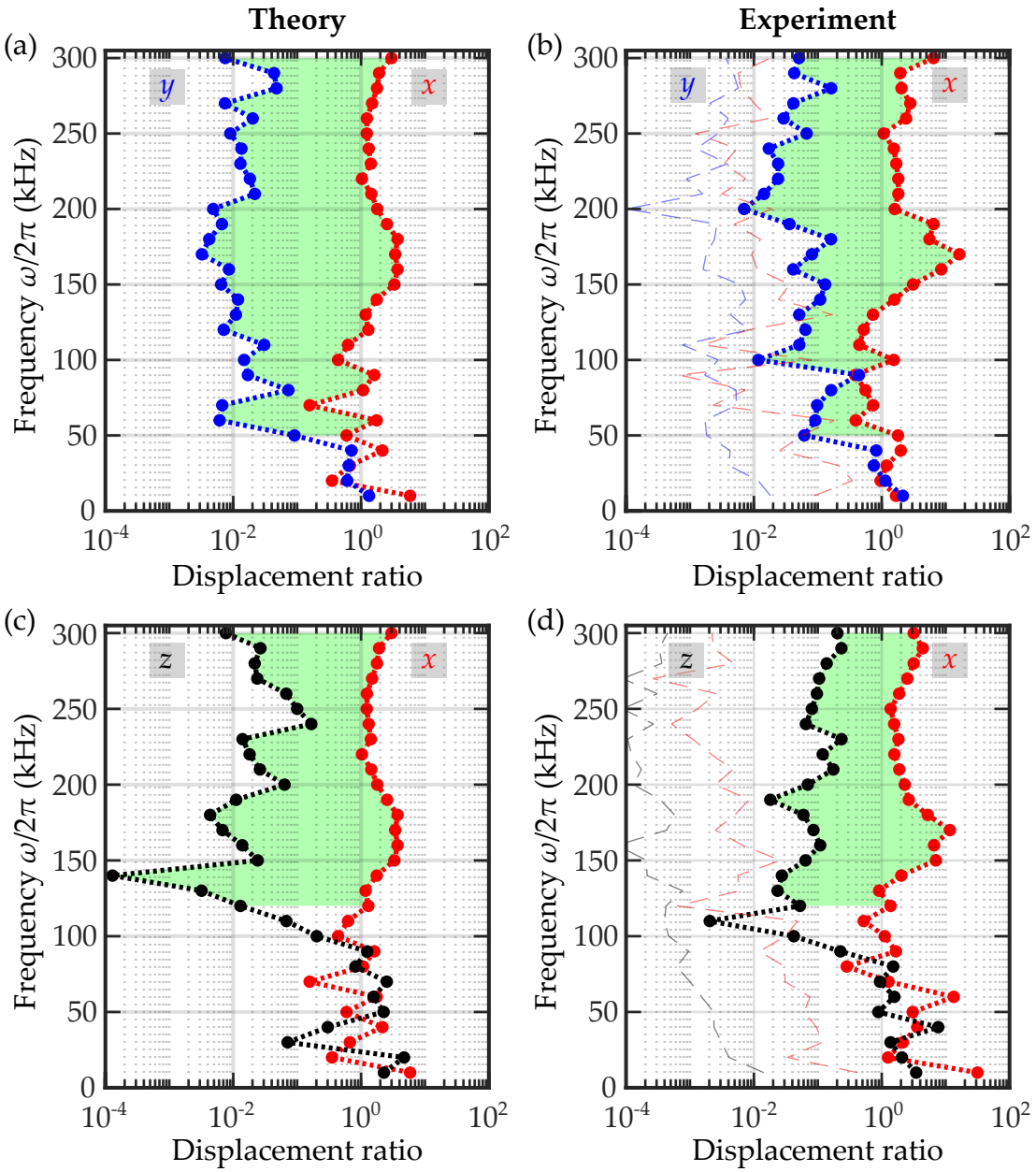

Figure 6.6: Polarizer action of the Tetramode metamaterial. The displacement ratio of output to input displacement (cf. Figure 6.5) is plotted component-wise versus frequency. (a) Results computed with finite element analysis for waves polarized along the y-direction (blue) and x-direction (red). (b) As (a) but results from the experiment. The dashed lines indicate the noise-floor of the experiment. To obtain this data, the piezoelectric transducer axis was aligned along the y-direction. (c, d) Analogous to (a, b), respectively. In (d), the transducer axis was aligned with the z-direction. For z and y, a suppression of up to two orders of magnitude over a broad frequency range can be seen. This range is emphasized by the green-shaded area. For these experiments, x- and y-displacements were obtained from DIC analysis, while z-displacements (black) were measured using vibrometry. Figure and caption taken from [92] and expanded under (CC BY 4.0), published by Adv. Mat. 2023.

To illustrate these findings versus frequency, the component-wise ratio of input to output displacement amplitude is plotted in Figure 6.6. The green shaded area highlights the frequency range of expected polarizer action. This region is linked to the frequency range of the band-structure calculations, where only a x-polarized mode is supported to propagate. The dashed lines in Figure 6.6(b, d) indicate noise-floor of the setup. This floor was computed from the component-wise ratio of $\mathbf{u}_{\text{in}}$ for every frequency, to $\mathbf{u}_{\text{out}}$ for $f = 0\,\text{kHz}$ i.e. when the transducer was not driven at all. These lines serve as a sanity check for the results. It is unphysical to detect a displacement smaller than the displacement noise-level when no waves are excited. From the dashed lines it becomes clear, why two configurations i.e. orientations for the transducer axis were chosen. If the input displacement along for example the y-direction (or z-direction) is large, the dashed line is pushed to smaller displacement ratios. Additionally, it is not necessary to orient the transducer axis along the x-direction, since a displacement ratio close to unity is expected, which is connected to a nanometer-scale output displacement, well within the setups resolution limit. In summary, data points for the displacement ratio lying below the corresponding dashed line should be discarded. However, this was not necessary for the presented results, and it becomes apparent that the setup is in principle capable of detecting even smaller displacement-ratios (down to 10^{-4}).

Comparing Figure 6.6(a) to (b) and (c) to (d), good qualitative agreement between prediction from theory and measured result for the polarizer performance is evident. A residual quantitative mismatch is attributed to remaining sample imperfections from fabrication. Nonetheless, a suppression in amplitude for the unwanted ($y-$ and $z-$) polarizations of up to two orders of magnitude is achieved. When referring to polarizers in optics, usually one concerns oneself with power (or intensity) and not with electric-field amplitude. To obtain a comparable quantity for the polarizer action of the tetramode metamaterial, the displacement ratio need to be squared. This yields a suppression of up to four orders of magnitude with respect to mechanical power. This is on-par with commercially available wire-grid polarizers [127].

Summary

With this work, we expanded the scope of available tools for ultrasound elastic-wave control with a polymer-based Tetramode metamaterial. The fact that four out of six deformation modes are "soft" is exploited to simulate, fabricate and experimentally investigate a compact broadband polarizer for transverse elastic waves or phonons. In both theory and experiment, a polarizer performance on the level of wire-grid polarizers from electromagnetism were predicted and achieved. Consequently, mechanical counterpart for transverse wave polarization was demonstrated. Furthermore, systematic scaling of the polarizer performance is possible by adding material both laterally or axially. Thereby, the usable polarizer output area is expanded (avoid edge effects) or the suppression of the unwanted wave polarizations is strengthened, respectively.

In terms of the experimental procedure for tracking all three displacement-vector components, the experiments on the Tetramode metamaterial were the first conducted with inclusion of the vibrometry branch in the setup. Therefore, they showcased the usefulness and practicality of vibrometry as a supplement to DIC analysis in a microscopy system. If one had to rely only on DIC analysis, the experiments would have been a lot more challenging. Rotation of the sample would have been necessary, in order to supplement the missing displacement vector component. Since the displacements here are small and the polarizer action is extremely direction-dependent, small misalignment in this rotation could deteriorate the detected performance drastically. With the vibrometry branch, these issues can be avoided completely.

6.3 Roton-Like Dispersion in Monomode-Metamaterial Beams

Within this section, I revisit the roton-like dispersion discussed in the previous chapter. Albeit here, the dispersion was yet again engineered through a very different mechanism as before. Namely, the exploitation of these soft modes present in a monomode material.

To avoid confusion, I want to provide a quick clarification of when I use "mode" as singular or "modes" as plural in the following text and in the context of extremal Cauchy-elastic materials. As the name suggests, a Monomode material features one soft mode of deformation [28]. For the dynamic case, when considering elastic waves, this corresponds to a relatively "flat" band along a certain direction in k-space. This band features a small phase and group velocity for the propagating waves[7]. Therefore, it is appropriate to speak of soft modes (thus in plural), when referring to modes described by this dispersion band.

The occurrence of the soft modes is necessary, but not sufficient to produce a roton-like minimum. Additionally, back-folding of the soft modes is required, with subsequent admixture of the corresponding bands to achieve the desired region of negative group velocity. The concept and the experiment results were published in [122] and are reported in the following.

6.3.1 Monomode Design and Back-Folding Strategy of the Soft Modes

The architecture of the Monomode metamaterial starts from a 2D periodic arrangement of rhombuses connected at their tips by circles, which is shown in Figure 6.7(a). The in-plane periodicity of the underlying square lattice is given by the lattice constant a, which is consequently also the length of the chosen unit cell[8]. The rhombuses are characterized by their thickness D, and the circles by their radius r (cf. inset in Figure 6.7(a)). Similar to the Tetramode metamaterial discussed in Section 6.2, the critical geometric parameter of the structure is the diameter d of the connections between rhombuses and circles (spheres and double-cones previously). The value of d dictates how easily those connections yield under load i.e. how close those connections come to ideal hinges. As typical for an extremal Cauchy-elastic material, for $d/a \to 0$, ideal hinges and thus an ideal Monomode metamaterial ensues.

[7] For an ideal Monomode material, the band would lie at zero frequency for finite k.
[8] Primitive Wigner-Seitz cell is smaller, cf. dashed box Figure 6.7(a)

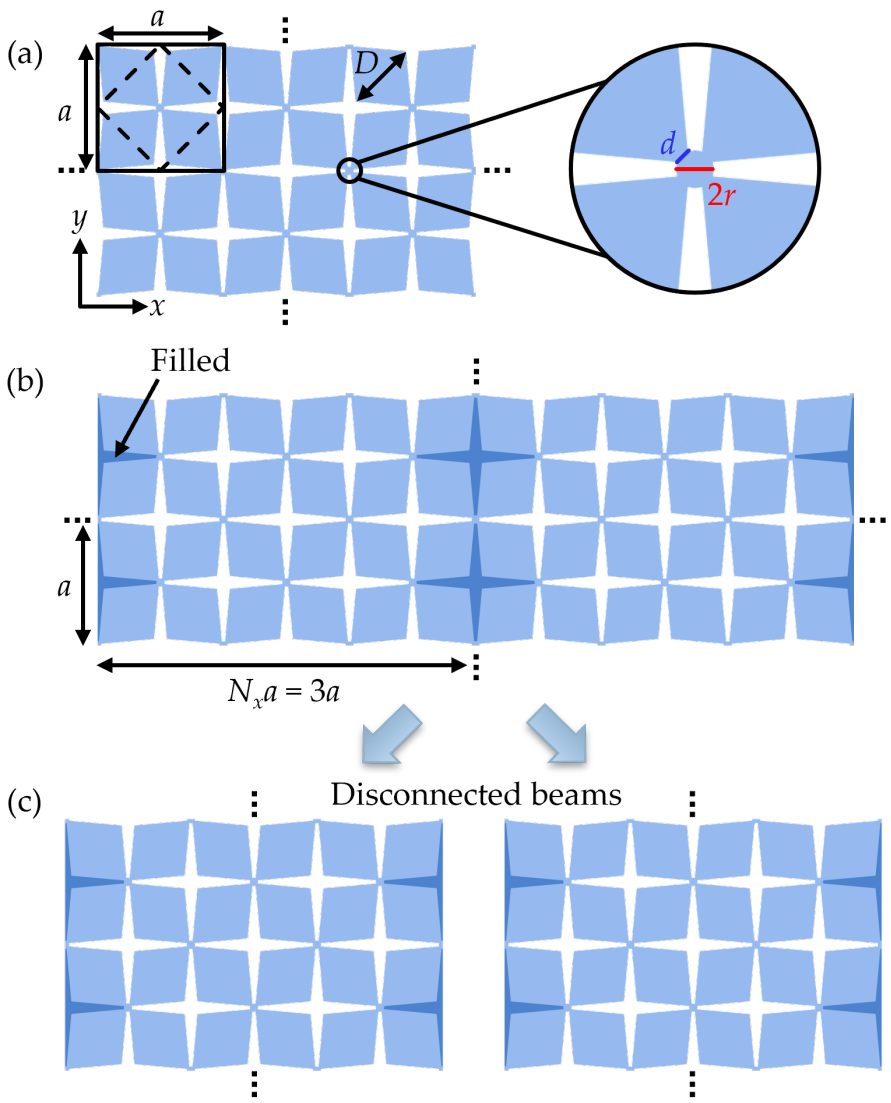

Figure 6.7: Monomode-metamaterial design for the back-folding strategy. (a) Infinite metamaterial bulk consisting of rhombuses with thickness D and circles with radii r (light blue). Extrusion out of the paper plane creates the three-dimensional structure. A unit cell of length a is enclosed by the black box, while the dashed box shows the primitive unit cell. The Inset enlarges the critical connection between rhombuses and circles. The diameter d of this connection is the critical geometric parameter of the Monomode metamaterial. (b) Introduction of a supercell with periodicity $N_x a = 3a$ by filling some voids (dark blue). This alteration shrinks the first Brillouin zone compared to (a) and introduces the desired back-folding of bands. (c) Disconnecting the bulk metamaterial along the x-direction at the periodicity of the supercell creates an array of separate beams, the dispersion relations of which are mutually degenerate. Importantly, the dispersion relation of the phonon bands is drastically altered by this modification. Figure and caption taken from [122] and expanded under (CC BY 4.0), published by Adv. Mat. 2023.

Similar to the spheres introduced in the Tetramode metamaterial, the circles connecting the rhombuses could be spared but significantly facilitate the control over the value of d during manufacturing and actually represents a degree of freedom for the tailoring of the dispersion.

From this planar outline of Figure 6.7, a three dimensional metamaterial is obtained when extruding the material along the z-direction by extrusion length a_z. Thereby, the rhombuses turn into skewed cuboids, and the circles into cylinders. Conceptually, this extrusion is irrelevant when considering periodic structures along all three spatial dimensions. For the subsequent experiments, a finite a_z has to be chosen, effectively creating a perforated plate or metamaterial slab. This geometry is vastly simpler in its design compared to the other structures discussed in this work, easing the manufacturing process significantly.

In analogy to the Tetramode metamaterial, the eigenvalues of the stiffness matrix can be derived in the long-wavelength limit from band-structure calculations [92] based on finite-element methods[9]. Assuming $E = 4.19\,\mathrm{GPa}$, $\nu = 0.4$ and $\rho = 1190\,\mathrm{kg\,m^{-3}}$ for the Young's modulus, Poisson's ratio and mass density of the constituent polymer, respectively and choosing the same geometric parameters used in the experiments (given in the next section below), one finds: 3.295 GPa, 0.875 GPa, 0.385 GPa, 0.296 GPa, 0.296 GPa, and 0.006 GPa [122]. Especially the last value is roughy three orders of magnitude smaller than the next largest one, hence making the metamaterial Monomode [28].

To understand how the Monomode character of the material is combined with a back-folding strategy to create a roton-like dispersion, it is helpful to consider Figure 6.7 and Figure 6.8 side by side. Before returning to the real-space metamaterial design in Figure 6.7, I shift to considerations in reciprocal-space depicted in Figure 6.8.

For elastic waves, the Monomode character of the material manifest in the calculated band structure for a bulk metamaterial as a valley in the dispersion surface of the lowest band. This valley lies at a diagonal with respect to the k_y, k_y-plane and can be clearly seen in Figure 6.8(a). Modes within the groove are emphasized by the black solid line, which would lie at strictly zero frequency for $d \to 0$. All modes along this line are considered "soft". For finite d, the modes correspond to transverse shear modes, propagating diagonally in the x, y-plane (cf. Figure 6.7(a)). To illustrate the back-folding procedure, two dashed curves are included in Figure 6.8(a). The first monotonously rising curve emerging at the edge of the blue subsurface (i.e. $k_x = k_y = 0$) only illustrates the edge of the dispersion surface at $k_x = 0$. The second dashed line is included twice. Once at $k_x = \pi/(3a)$ and again at $k_x = 0$.

[9] Conducted by Yi Chen in COMSOL.

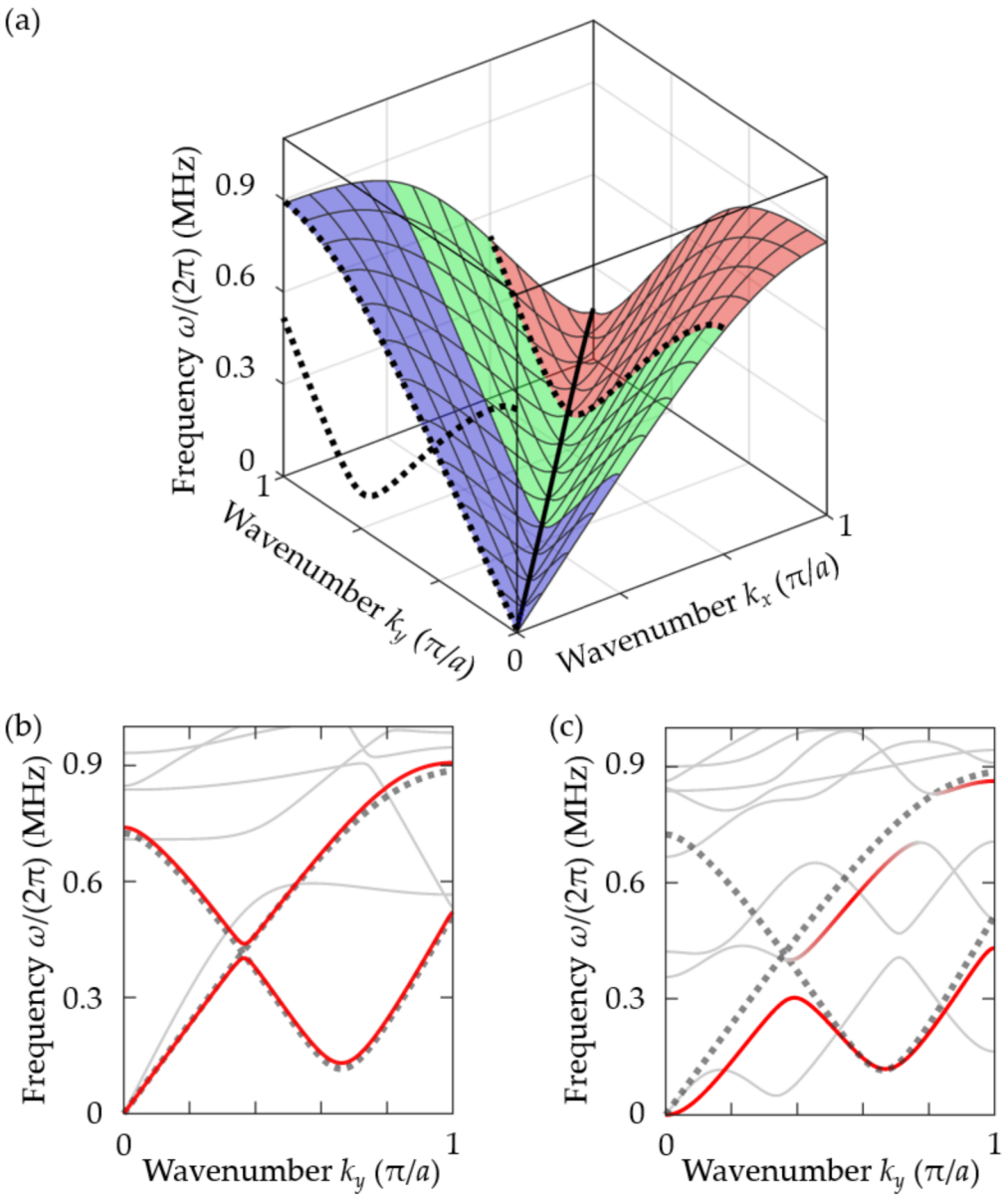

Figure 6.8: Back-folding strategy in reciprocal-space. (a) Frequency surface of the lowest modes over k_x and k_y in a bulk Monomode metamaterial (transverse shear modes). The solid black line extending diagonally describes the "soft" modes. The coloration of the surface helps to comprehend the introduction of a supercell $N_x a = 3a$, shrinking the first Brillouin zone to $|k_x| < \pm\pi/(3a)$. The green and red sections are shifted by $2\pi/(3a)$ along negative k_x. Consequently, the black dashed curve between the green and red sections now lies at $k_y = 0$ and crosses the band extending along k_y. (b) Dispersion for the bulk material with supercell period $N_x a = 3a$. For visualization, the uncoupled bands are kept (dotted lines). The supercell introduces coupling between those bands leading to weakly hybridized bands (red). (c) Dispersion for a beam of width $N_x a = 3a$. The new boundary condition dramatically strengthens the hybridization, even extending it to other (longitudinal) bands. Figure and caption adapted from [122] under (CC BY 4.0), published by Adv. Mat. 2023.

There, the line becomes valid when artificially considering a different periodicity of $N_x a = 3a$ along the x-direction. The edge between the red and green subsurfaces is back-folded to $k_x = 0$ and the dashed lines (i.e. bands) simply overlap. In other words, the first Brillouin zone shrinks along k_x. So far, no coupling between the bands is introduced, since merely a different representation was chosen and no alteration to the structure is performed[10]. Up to this point, the structure remains identical to Figure 6.7(a).

Actual back-folding and hybridization of the bands (dashed lines at $k_x = 0$) is realized with an alteration to the structure. In this case, by introduction of a supercell with period $N_x a$ along the x-direction. This is done physically by filling voids in the material, as shown in Figure 6.7(b). Coupling of the previously overlapping bands ensues[11]. Initially, the hybridization is weak, which can be inferred from the small gap between the two red bands shown in Figure 6.8(b). However, a roton-like dispersion of the lowest band can already be recognized. Two local extrema connected by a region of negative group-velocity $\mathrm{d}\omega/\mathrm{d}k_y < 0$ are visible. The minimum at $k_y = 2\pi/(N_x a)$ is directly related to the back-folded soft modes of the Monomode metamaterial.

In a follow-up step, the boundary condition along the x-direction is significantly altered. The material is dissected every $N_x = 3$ unit cells into an array of identical beams, depicted in Figure 6.7(c). Since the beams are identical, their respective elastic-wave dispersions are degenerate. Thus, for the following discussion, it is sufficient to only discuss a single beam. As a consequence the dissection, the coupling between the bands dramatically strengthens. Hybridization even extends to initially longitudinal modes, which is evident from Figure 6.8(c). Not only the lowest red band shows a roton-like behavior, but also the lowest grey band as well which corresponds to longitudinal modes. The reason for this behavior becomes clear when observing the individual mode-shapes, i.e. the displacement field of the modes (similar to Section 5.3.2).

For a Monomode bulk, the longitudinal modes feature a displacement field $\mathbf{u}(\mathbf{r}, t)$ with mostly parallel orientation to the wave vector $\mathbf{k}$. For laterally finite samples, such as beams, the orientation of the displacement field changes significantly for those modes. Now, large displacement-vector components orthogonal to $\mathbf{k}$ arise, which are generally considered for transverse modes. Thus, the originally longitudinal modes are no longer pure in the sense of their polarization, suggesting a strong admixture with transverse modes. Accordingly, they should be considered longitudinal-like, and they become subject to the same back-folding and hybridization mechanism.

[10] Inherently, choosing different unit-cell sizes without altering the structure leaves the underlying physics unchanged.

[11] Similar to the admixture of negative group-velocity behavior of chiral optical modes into acoustic modes (Section 5.3.2 and [27]), the negative group-velocity property of the soft modes is admixed into the original band, giving rise to a roton-like dispersion of the lowest band.

In conclusion, the exact shape of the bands depends on only two parameters, which in turn are important for the intended tailoring of the band structure. The first parameter d directly influences the Monomode character of the metamaterial and thus the "depth" of the valley from Figure 6.8(a). Consequently, d also influences the "depth" of the roton-like minimum in the dispersion bands, moving the minimum closer to zero frequency for $d \to 0$. The second parameter is the number of unit cells N_x enclosed in a single supercell. Lowering or increasing N_x gives rise to fewer or additional local extrema in the bands, respectively. In [122], computed band-structure results for $N_x = 2$ and $N_x = 4$ are included, supplementing Figure 6.8. In the experiments, I only investigated samples with $N_x = 2, 3$. Fabricating samples with $N_x = 4$ is straightforward. However, a larger number of unit cells would be required to yield sufficient k-space resolution to resolve the additionally occurring local extrema.

Remark on nonlocality and altered periodicty

The introduction of the supercell with $N_x a = 3a$ may bring to mind the beyond-nearest-neighbor coupling from Section 5.2, where also an additional periodicity of $3a$ was introduced. However, there are noteworthy differences.

In the nonlocal approach, this periodicity was introduced along the parallel and not the orthogonal propagation direction of the excited elastic waves with wavevector $\mathbf{k}$. However, the introduction of the beyond-nearest-neighbor coupling did not alter the underlying periodicity along $\mathbf{k}$, which remained strictly a [26].

For the Monomode metamaterial, introduction of the supercell by filling voids every $N_x = 2$ or $N_x = 3$ unit cells, creates a new periodicity orthogonal to $\mathbf{k}$ (i.e. along the x-direction) with $3a$. As a consequence of this distinctness, the effects on the dispersion bands were also arguably conceptually different between the two approaches.

6.3.2 *The Fabricated Metamaterial Samples*

The geometry files for fabrication were generated in COMSOL Multiphysics by Yi Chen and myself. Subsequently, I took care of optimizing the writing strategy. All samples fabricated for the experiments featured a common in-plane lattice constant of $a = 300\,\mu\text{m}$, out-of-plane extrusion length of $a_z = 600\,\mu\text{m}$ and rhombus diameter $D = 148.5\,\mu\text{m}$. Furthermore, common numbers of unit cells along y-direction, $N_y = 40$ and z-direction $N_z = 1$ were chosen. Only the two important parameters N_x and d were varied, giving rise to different sample generations[12].

[12] The radius r of the connecting circles (cylinders) is intrinsically linked to d and thus cannot be independently modified.

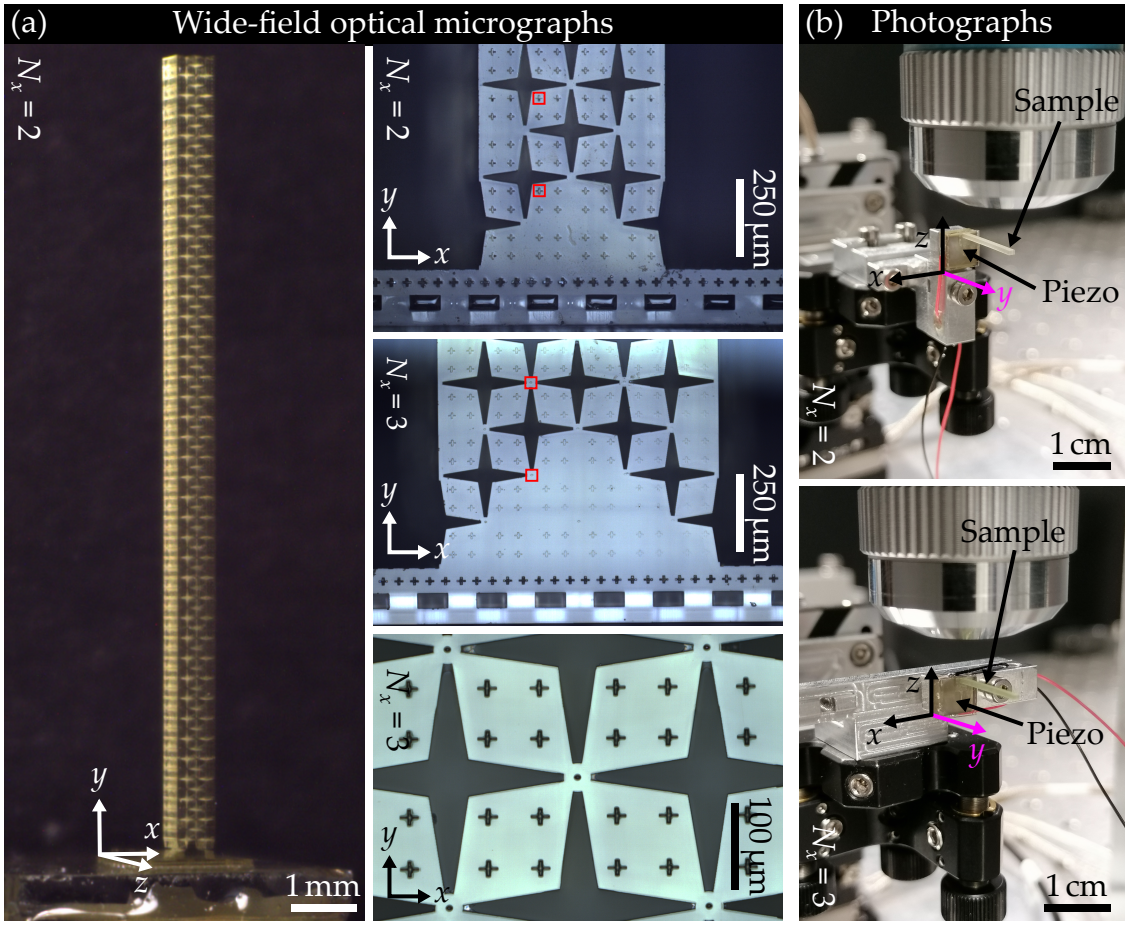

Figure 6.9: Showcase of the fabricated Monomode metamaterial. (a) Wide-field optical micrographs offering different views on several sample features. To the left, a sample comprised of $N_y = 40$ layers along the beam y-axis and $N_x = 2$ unit cells along the x-axis is shown. The bottom plate of the sample can be seen close to the tripod. On the right column, several close-ups are presented. On the top (middle), the connection of a beam with $N_x = 2$ ($N_x = 3$) to its bottom plate is magnified. This wedge-shaped transition region is deliberately designed to efficiently couple the mechanical excitation into the modes showing roton-like dispersion. On the sides of the beam, the added mass introducing the supercell can be seen, also. On the bottom, a single unit cell is displayed. The cross-shaped markers in the rhomboids, and the circular markers in the rhomboid-connecting cylinders are visible. In each unit cell along the beam axis, one such marker was tracked to sample the displacement field $\mathbf{u}(\mathbf{r}, t)$. Regions of interest placed on markers are highlighted by red squares. (b) Samples with $N_x = 2$ and $N_x = 3$ glued onto a piezoelectric transducer and mounted in the setup for elastic-wave tracking. The transducer axis is highlighted (magenta). Figure and caption adapted from [122] under (CC BY 4.0), published by Adv. Mat. 2023.

A showcase of fabricated metamaterial beams is given in Figure 6.9. To confirm consistency in d between simulated geometry and experiment, the value of d was measured using optical wide-field microscope (Smartzoom 5, Zeiss) or the experimental setups confocal-imaging branch with its calibrated field of view. The samples were once again printed onto a bottom plate. The transition region between bottom plate and the lowest layers of the metamaterial samples were tailored specifically. Filling several voids implements a wedge-shape. which ensures coupling of the mechanical excitation into the desired modes with roton-like dispersion. On each rhombus, 2×2 cross-shaped markers are implemented as shallow intrusions of roughly 20 µm into the polymer. In the center of the cylinders, round markers were implemented with the same intrusion depth. Those markers create additional contrast for displacement tracking with DIC analysis.

The samples were printed in similar fashion as the chiral metamaterial from Section 5.3, albeit with much simpler printing strategy. Their beam axis was oriented parallel to the substrate, however, no sacrificial layer was required due to the simplicity and rigidity of the Monomode material. All sample variations (with respect to d and N_x) were fabricated with a hatching distance of $d_{\text{hatch}} = 500\,\text{nm}$, and slicing distance of $d_{\text{slice}} = 1.5\,\mu\text{m}$. The focus velocity (scan speed) was set to $0.140\,\text{m}\,\text{s}^{-1}$. For the samples with $d = 16.4\,\mu\text{m}$ and $d = 45.2\,\mu\text{m}$ a laser power of 50 mW was used. The latter was measured at the entrance pupil of the objective lens. To achieve the smaller value of $d = 9.3\,\mu\text{m}$, the laser power was reduced to 20 mW. Again, a bottom plate was included at one end of each sample to facilitate sample manipulation. The plate was printed with the same parameters as the respective sample itself.

For development, the samples were submerged for 45 min in PGMEA and 5 min in acetone before air-drying under ambient laboratory conditions. The markers were implemented as intrusions on the sample side facing the substrate. Therefore, it was necessary to detach the sample from the substrate while submerged in PGMEA. Otherwise, unpolymerized photoresist could remain in the intrusions rendering the markers useless. As usual, more details on writing parameters and printing strategy can be inferred from the machine code and job files published in the corresponding repository of [122].

6.3.3 *Band-Structure Measurement*

The experiments to extract the band structure for elastic waves from the displacement field $\mathbf{u}(\mathbf{r},t) = (u_x(\mathbf{r},t), u_y(\mathbf{r},t), u_z(\mathbf{r},t))^{\mathrm{T}}$ were conducted as described in Section 4.3[13]. The samples were mounted with their beam axis parallel to the field of view of the confocal-imaging branch, enabling a side-view showing the markers, cf. Figure 6.9(b). In this orientation, u_x and u_y were determined with DIC analysis from confocal image data, and u_z using the laser-Doppler vibrometry.

The displacement field was sampled at 41 ROI, the first of which was positioned at a cross-shaped marker on the bottom plate to survey the displacement excitation. The remaining 40 ROI were positioned onto either cross-shaped or round cylindrical markers, each on a separate unit cell spaced by a, cf. red boxes in Figure 6.9(a). In principle, it does not matter if cross-shaped or cylindrical markers are selected, as long as equivalent markers are used for each experiment. Depending on the shape of the amplitude envelope of a mode, different types of markers have different displacement amplitudes and therefore my vary the signal to noise in the displacement measurement. Extraction of the displacement vector component amplitude distribution (amplitude envelope) of the ensuing 3D standing-wave pattern was performed with Fourier analysis of the time-resolved raw displacement data. The covered frequency range was 10 kHz to 600 kHz in increments of 5 kHz, covering the frequency range of the back-folded and hybridized bands. Fourier transform of the amplitude envelopes with respect to real-space reveals the desired band structure.

A total of six sample generations were investigated. Three different choices for d were realized, both with $N_x = 2$ or $N_x = 3$ in order to investigate the dependence of the band structure on those parameters independently. For the sake of brevity, I focus on the most important findings and results. The complete dataset can be found in [122] and its supporting information. Results for samples with $d = 16.4\,\mu\mathrm{m}$ and $N_x = 2$ as well as $N_x = 3$ are depicted in Figure 6.10.

In both cases, the roton-like bands emerge in the dispersion relation derived from both $u_x(\mathbf{r},t)$ and $u_y(\mathbf{r},t)$ respectively. At frequencies above 420 kHz, optical modes emerge which are in good agreement with theory predictions (grey lines). As mentioned above, this is due to the fact that the finite lateral extend of the beam causes both longitudinal and transverse modes to feature significant displacement contributions along x and y. The exception being the modes of the ordinary flexural band of a beam, the displacement field of which is oriented along z. Hence, those modes only exhibit significant displacements in $u_z(\mathbf{r},t)$. Consequently, the modes are only revealed in the right-most panels of Figure 6.10.

[13] In a similar manor as for the nonlocal (Section 5.2) and chiral (Section 5.3) metamaterial beams.

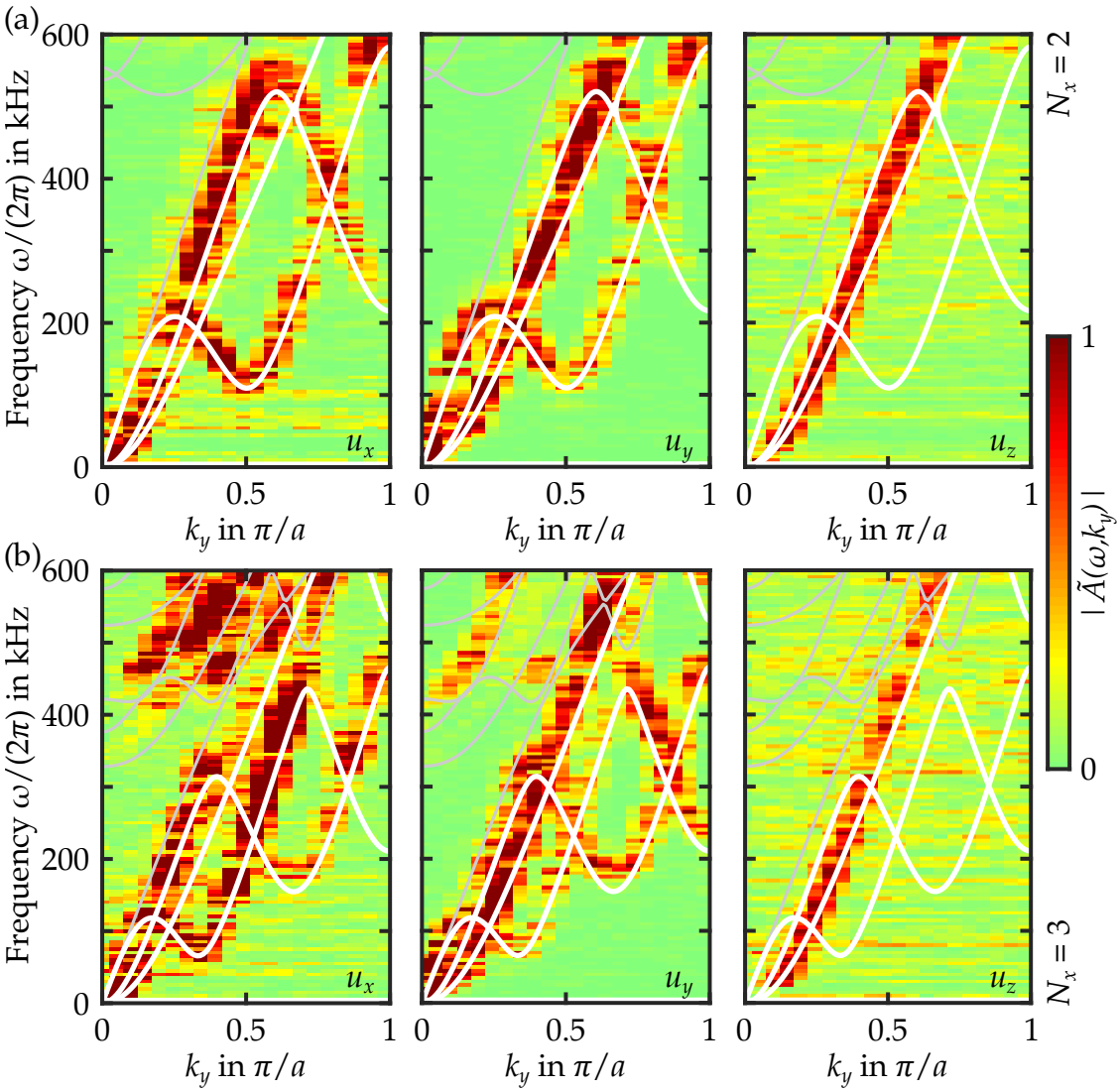

Figure 6.10: Dispersion-relation-measurement results on Monomode-beam samples. The critical parameter of the structure is $d = 16.4\,\mu\text{m}$. As in the previous Chapter, the modulus of the complex response function $|\tilde{A}(\omega, k_y)|$ is plotted in false-color versus wavenumber k_y and frequency $\omega/(2\pi)$. Solid white lines represent the computed three lowest bands for an infinite beam ($N_y = \infty$). (a) Results for a sample with $N_x = 2$ cells along x. From left to right, the results for $|\tilde{A}(\omega, k_y)|$ derived from the respective displacement-vector components (u_x, u_y and u_z) via 2D Fourier transformation are depicted. In the first two panels, distinct regions of negative slope are achieved. Thus, the roton-like bands are clearly visible and agree well with theory. The third panel only shows a single band. The latter corresponds to modes polarized along the z-axis, which follow the dispersion expected for a simple beam. Modes with roton-like dispersion remain absent, since they do not feature displacement-field components along z. (b) In analogy to (a) but for a larger supercell with $N_x a = 3a$. Additional local extrema emerge, as it is expected for the now even smaller first Brillouin zone as compared to $N_x a = 2a$ in (a). Figure and caption adapted from [122] under (CC BY 4.0), published by Adv. Mat. 2023.

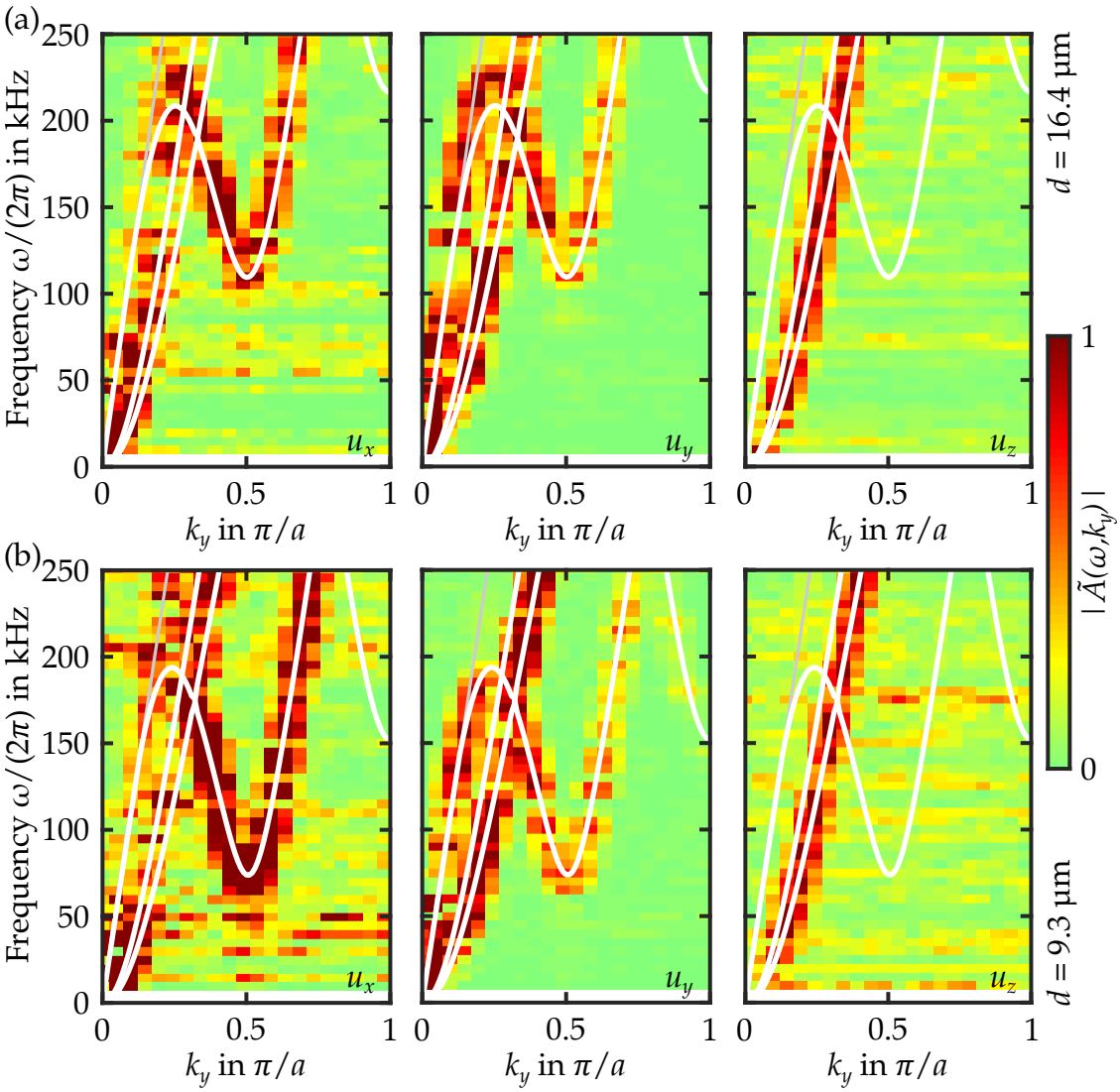

Figure 6.11: Influence of the critical parameter on the dispersion bands. (a) Identical data to Figure 6.10 but in a reduced frequency range to better visualize the local band minimum. (b) Data in the same frequency range but for a sample with reduced critical parameter from $d = 16.4\,\mu m$ to $d = 9.3\,\mu m$. Induced by the 32 % reduction in d, the local minimum shifts in frequency by 43 % from 110 kHz to 75 kHz. This behavior agrees nicely with theory (white lines), as a smaller value of d makes the "soft" mode even "softer" and lowers the roton-like minimum. Consequently, these results demonstrate how the dispersion can be tailored directly by controlling the geometric parameter d. Figure and caption adapted from [122] under (CC BY 4.0), published by Adv. Mat. 2023.

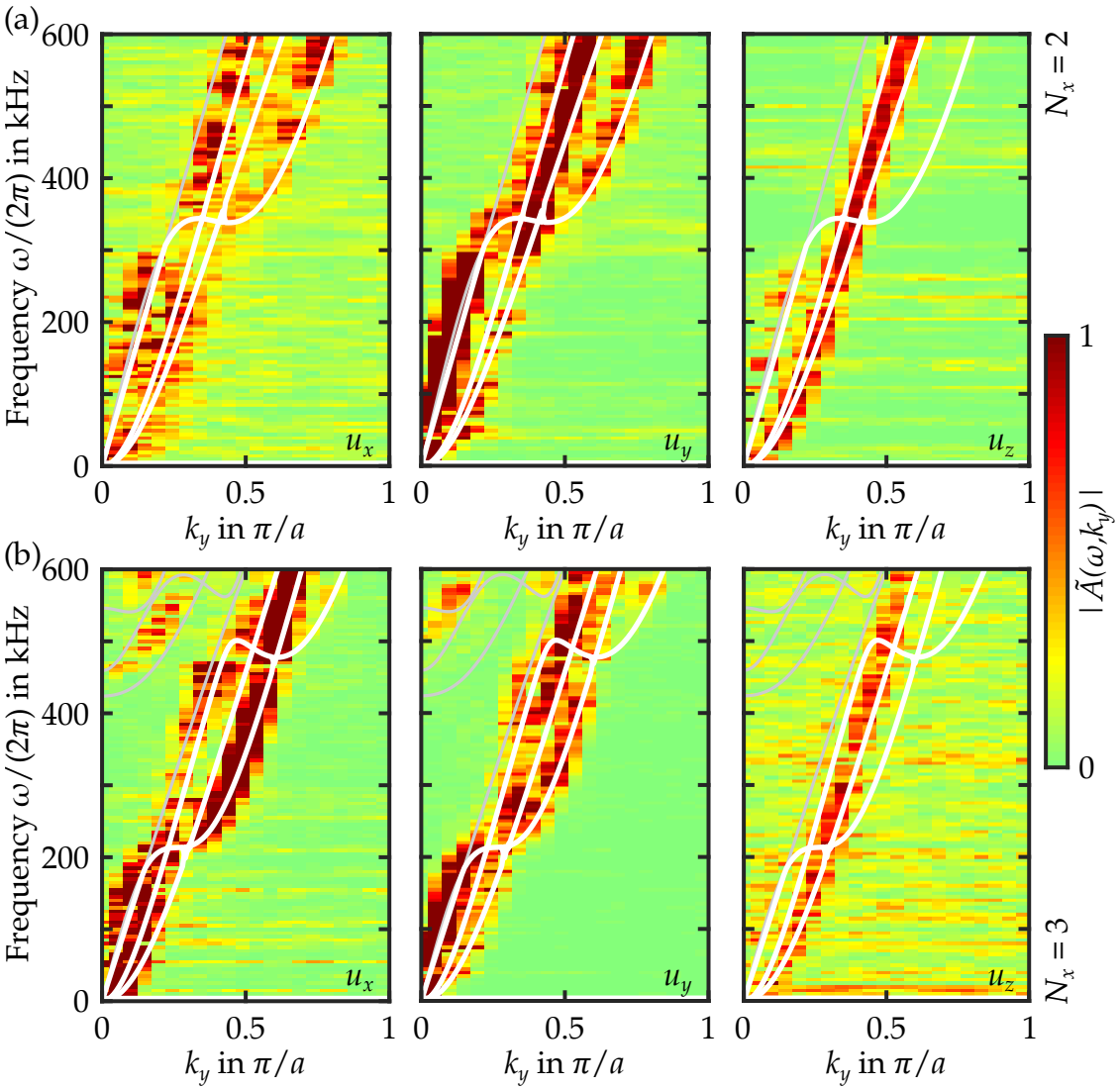

Figure 6.12: Creating saddle points in the dispersion relation. The data is depicted in the same false-color manner as in Figure 6.10 and Figure 6.11. Formation of saddle points was achieved for beam samples with super lattice size (a) $N_x a = 2a$ and (b) $N_x a = 3a$, respectively. The value of the critical parameter was increased to $d = 45.2\,\mu\text{m}$. These experiments further emphasize how by increasing the diameter d, adjacent local extrema can be merged into a saddle point, controlling the number of points with zero group-velocity through different means than changing N_x. Figure and caption adapted from [122] under (CC BY 4.0), published by Adv. Mat. 2023.

Eminent agreement between calculations for infinite beams ($N_y = \infty$) with the experimental data for finite beams ($N_y = 40$) is found. As an intermediary result, Figure 6.10 shows how the number of local extrema can be controlled by adjusting N_x. Subsequently, those proof-of-principle experiments are extended by studying the influence of smaller and larger d, respectively.

As aforementioned, reducing the value of the critical parameter should further "soften" the already "soft" modes in the Monomode metamaterial. Consequently, the roton-like minimum is expected to shift to lower frequencies. Experimental results confirming this hypothesis are depicted in Figure 6.11. A comparison is made between samples with $N_x = 2$ and $d = 16.4\,\mu\text{m}$ versus $d = 9.3\,\mu\text{m}$. In the depicted reduced frequency range it can be seen how the roton-like minimum indeed shifts down in frequency almost proportionally to the reduction in d.

It is natural to also go towards larger values of d. Experiments were conducted for samples with $N_x = 2$ and $N_x = 3$ with $d = 45.2\,\mu\text{m}$. The results are given in Figure 6.12. The value of d was deliberatly chosen to merge the local maxima and minima together in frequency and wavenumber, thus creating a saddle point. In a way, this shows that the number of local extrema is not only controllable by the value of N_x, but also by the value of d. Logically, increasing d diminishes the Monomode properties of the metamaterial. Going to even larger values of d is not interesting as little further insight is expected. For large enough d, the structure will turn into a simple un-perforated plate or slab and the dispersion transitions into the one expected for a solid plate or slab.

Summary

Within the project I reiterated above, we realized another, namely a third mechanism to obtain roton-like dispersion relation for elastic waves in a microscale metamaterial. The Monomode property of an extremal Cauchy-elastic material was explicitly used to tailor the lowest bands for elastic waves. A vast reduction in complexity of the underlying metamaterial geometry was demonstrated. The tailoring of the dispersion relation is achieved by controlling only two parameters. The benefits of this may be twofold. On one hand, this may ease the access of new research groups to the field of dispersion relation engineering of the lowest bands. On the other hand, since the geometry is in principle a perforated plate, other more scalable fabrication techniques may be employed. Thus, larger quantities can be fabricated, making the material available for potential applications.

Furthermore, this mechanism to obtain roton-like dispersion through back-folding might nourish the endeavor to obtain equivalent results in the fields of acoustics and optics - similar to the case for the nonlocal approach. Additionally, these results may provide an incentive to further consider the dynamic properties of extremal Cauchy-elastic materials in the context of dispersion engineering.

Chapter 7

7 Summary, Conclusion and Outlook

Within this thesis, I have developed a procedure for the time-resolved tracking of elastic waves by their displacement field in three-dimensions with nanometer-displacement resolution at ultrasound frequencies. In contrast to previous work on the matter by others, no stroboscopic illumination or high-speed camera was required. Instead, the high analog bandwidth of an avalanche photodiode detector was used in conjunction with synchronization between data acquisition and elastic-wave excitation within a self-build confocal laser-scanning back-scattering microscope. Based on this synchronization, in-plane displacement information could be extracted from images with the help of well-established digital-image cross-correlation analysis. The so-far missing out-of-plane displacement information was supplemented using laser-Doppler vibrometry which was seamlessly integrated into the confocal microscope.

Expanding the displacement measurement over several layers of metamaterial-beam samples allowed to reconstruct the elastic-wave dispersion for waves of arbitrary polarization, thereby fulfilling both core goals that I set out to achieve within my thesis. The measurement procedure as well as the experimental setup were validated in experimental projects by myself and my master student on four different types of microscale mechanical metamaterials, leading to several publications in high-impact scientific journals and conference contributions of myself and my colleagues.

In three out of the four projects, a roton-like dispersion for elastic waves was engineered by my colleagues, and subsequently observed in experiments which I either conducted myself or supervised. This interesting dispersion relation, resembling the roton dispersion of liquid helium, features a wide range of negative group-velocity in the lowest phonon bands. Thus, giving rise to backward-waves and equivalently a negative index of refraction, conceptually at zero loss.

While the outcome of the three projects may seem very similar, three vastly different underlying mechanisms were used to achieve such dispersion. Namely, nonlocality, extreme chiral coupling, and band back-folding of soft modes within an extremal Cauchy-elastic Monomode metamaterial.

With the three-dimensional displacement measurement capability of the setup, a more complete picture of the metamaterial eigenmodes i.e. elastic-wave displacement fields was made accessible and thus allowed to observe elastic waves of truly arbitrary (displacement) polarization. Especially this aspect was picked up by myself to demonstrate and characterize a microscale broadband polarizer for transverse elastic waves. The corresponding metamaterial was based on another extremal Cauchy-elastic material, namely a Tetramode metamaterial. Therefore the setup also contributed to the research on this so-far sparsely experimentally investigated material class. In the following, I supplement a brief summary of the key points from the individual Chapters of my work.

In Chapter 2, an introduction into linear Cauchy-elasticity was given. The focus was put on the generalized Hooke's law in 3D as the constitutive law between stresses and strains. As the core of this thesis revolves around elasto-dynamic phenomena, a summary on the equations of motions was included, a solution of which are elastic waves. Their dispersion was derived for simple masses-and-spring systems such as linear chains to form a knowledge base for the content of the following Chapters. The Chapter concluded by summarizing 3D laser microprinting as a means to fabricate the microscale polymer-based mechanical metamaterials. The intend of this Chapter was to provide the necessary fundamentals from continuum mechanics, such that novices in the field of mechanics may follow the experimental results on mechanical metamaterials presented within this work.

Following this reasoning in Chapter 3, the necessary background information on the optical metrology techniques for displacement measurement were given. The principle of confocal microscopy and its resolution limit were summarized. Digital-image cross-correlation analysis was introduced as a method to extract in-plane displacements of magnitude well below the optical resolution limit of the previously discussed microscope. Laser-Doppler vibrometry was explained, starting with the Doppler effect itself and leading towards the exploitation of this effect in an interferometer to obtain time-resolved out-of-plane displacement data. The resolution limit of a vibrometry system was discussed and it was shown that the technology is suitable for (sub)nanometer displacement measurements, even for low-reflectivity samples such as polymer-based metamaterials.

In Chapter 4, the commissioning of the experimental setup was reported and its displacement measurement capabilities demonstrated. The commissioning process was divided into two parts. The first part focused on the confocal-imaging branch and the second part on the seamless addition of the laser-Doppler-vibrometry branch. Two key aspects were discussed which are crucial to obtain correct absolute displacement measurements in three dimensions. The first aspect addresses a potential cross-talk between out-of-plane and in-plane displacements for too-fine axial sectioning of the confocal-imaging branch. It was stated, that the axial sectioning should be chosen orders of magnitudes larger ($\propto$ µm) than the expected displacement magnitudes ($\propto$ nm). Furthermore, flat surfaces oriented perpendicular to the optical axis should be selected for measurement. Additionally, a calibration procedure was described to remove the effect of the Gouy-phase shift on the out-of-plane displacement detected by vibrometry-integrated microscopes. Following these preparations, an example of the displacement-measurement capabilities was given for a single location. Therein, the data acquisition for the confocal imaging was described, in order to measure displacements correctly in the ultrasound frequency range without the need for high frame-rates or stroboscopic illumination. The Chapter closed with a demonstration of the procedure used in the following Chapters to obtain the dispersion relation i.e. band structure for elastic waves in a metamaterial-beam sample.

In Chapter 5, the first two projects revolving around such dispersion-relation measurements were reported. Each report was preceded by a short summary on the underlying respective theory. Two types of mechanical metamaterials were investigated, which use different mechanisms to obtain the aforementioned interesting roton-like dispersion relation for elastic waves. With the setup, the displacement fields of such waves, including the peculiar backward-waves, were observed and the underlying dispersion relations were extracted. The first metamaterial featured tetragonal symmetry and incorporated nonlocal interaction for waves propagation along a single spatial direction. The corresponding results sparked multiple experimental and theoretical follow-up projects in acoustics and electrodynamics, partly expanding the effect to higher dimensions of wave propagation. The second material followed the suggestion to obtain such dispersion through other means, namely through chirality. Owing to the chirality of the unit cell, the eigenmodes featured displacements along all three spatial directions. Thus, vibrometry was the ideal addition to the setup to observe and extract the dispersion from all three displacement-vector components respectively in one experiment, without the need for reorienting the sample.

Chapter 6 opened with the definition and properties of extremal Cauchy-elastic materials, as two types of such materials were subjected to experiments. Namely, a Tetramode metamaterial with four soft modes (small eigenvalues in the stiffness matrix), and a Monomode metamaterial with one soft mode. The Tetramode metamaterial was shown to be applicable as a compact and broadband transverse-wave polarizer. Thereby, supplementing previous work by others in the field on Pentamode metamaterials which in turn acted as a longitudinal-wave polarizer. In this thesis, a polarizer performance on-par with commercial transverse (wire-grid) polarizers in optics was achieved. For those experiments, the three-dimensional displacement tracking of the setup again proofed exceptionally useful, since the displacement-field vector of arbitrarily polarized elastic waves could be tracked, without the need to rearrange wave-excitation and sample with respect to each other. With the Monomode metamaterial, a third mechanisms to obtain a roton-like dispersion in metamaterial beams was observed. Herein, the soft mode was combined with a back-folding and hybridization strategy of the lowest dispersion bands. In this project, the setup was not only used to reconstruct the dispersion for a single set of geometric parameters, but also to conduct a parametric study on how alterations of the sample geometry influenced and modulated the lowest dispersion bands in their number of local maxima and frequency range for backward-waves. Thus, proving to be a valuable tool for subsequent work on dispersion engineering in the field of mechanical metamaterials.

Outlook

In terms of metamaterial research, further enhancement of the setup can be envisioned. For example, the system can be easily expanded into a scanning laser-Doppler vibrometer. Thereby, out-of plane displacement information from different regions in the current field of view become obtainable. Furthermore, multi-axis piezoelectric transducers could be implemented, enabling access to additional excitation conditions, or at least enhanced control over the latter. By doing so, I assume that the mechanical excitation could be chosen to efficiently couple into desired eigenmodes of the metamaterial one wants to observe. Consequently, it may be possible to avoid the need to engineer a dedicated transition region within the samples and still excite the favoured eigenmodes efficiently.

Technology-wise, it is apparent that the presented setup features a significantly increased complexity compared to a wide-field imaging approach with stroboscopic illumination. However, compared to wide-field systems, integration of a vibrometry branch along the lines of C. Rembe et al. [100] is straightforward and therefore the extension to the three-dimensional displacement measurement is arguably more convenient. Consequently, I could imagine that the combination of digital-image cross-correlation analysis with laser-Doppler vibrometry in a microscopy system may find more widespread use, especially for the investigation of microscale mechanical metamaterials. For those metamaterials, to the best of my knowledge, the choice of commercial devices capable of 3D displacement tracking at ultrasound frequencies is quite limited. For macroscale samples, commercially available 3D laser-Doppler vibrometers exist [73]. However as mentioned, those systems operate on the macroscale and are orders of magnitude more expensive. For microscale samples, one possibility may be stroboscopic video microscopes using interferometric techniques with elaborate data analysis for 3D-displacement measurements, which was shown as proof-of-concept in 2002 [128]. Alternatively, commercial LDV microscopy systems exist, which feature an integrated stroboscopic-video-microscopy mode [73]. At the time of writing, the lateral resolution of such devices remains on the order of 5 nm [73] and thus do not seem to exploit the full potential of the technique, which may be subject to change in the future [129]. In principle it has also been shown by C. Rembe et al. in 2014 [130] that microscopy based 3D laser-Doppler systems are also possible. However, to my knowledge, no commercially available product has emerged so far along those lines. The future will show, which of those technologies will become more established as research and development progress.

Acknowledgments

Herein, I want to take the opportunity to thank all the people who supported and assisted me during this thesis. While completely listing the names of all individuals would go beyond the scope of this Chapter, I want to at least emphasize the most prominent supporters of my work and apologize to all I may miss.

I want to start by thanking Prof. Dr. Martin Wegener for the opportunity he granted me in the form of this PhD position and suggesting me to the HEiKA Graduate School on Functional Materials to nourish my research project. His support and guidance during the whole time of my thesis manifested in countless scheduled and unscheduled meetings, in which he was always eager to discuss the latest results of my research or discuss and resolve problems that stood in my way. I genuinely appreciate the time he invested when needed as a supervisor.

Next, I want to express my gratitude to Prof. Dr. Muamer Kadic for agreeing to co-referee this thesis. Additionally, I want to thank him for accompanying my thesis from the beginning of the first experiments on mechanical metamaterials. The mutual cooperation yielded fruitful research projects, which lead to the plentiful experimental successes I was able to achieve.

Similarly, I want to thank Yi Chen, who conducted and lead the numerical calculations for modeling and predicting the expected behavior of the mechanical metamaterials I experimented on. Furthermore, I enjoyed to benefit and draw from his extensive knowledge in mechanics, which fostered and expanded my own understanding on the matter.

As for every professional project, a certain bulk of paperwork had to be taken care of. In this regard, I want to thank the secretaries of the Institute of Nanotechnology, foremost Patricia Jäger and Christine Fischer, as well as the staff of the secretariat in the Institute of Applied Physics, namely Ursula Mösle, Claudia Alaya, Monika Brenkmann, Petra Bauer and Gloria Zanda, to support me throughout my employment.

At this point, I am pleased to acknowledge also the support of the people from the workshops of the Institute of Applied physics, who fabricated, machined, cut, ground and soldered countless components and devices I needed for the commissioning of the experimental setup. I want to especially mention Johann Westhauser as our group technician, and Frank Landhäuser as well as Maik Nothdurft from the mechanical workshop.
Furthermore, I want to of course also mention explicitly the help from the electronics workshop, provided by Michael Hippe, Werner Gilde and Helmut Lay. In summary, I always felt that the workshops helped me to overcome challenges quickly through their long-standing expertise in their respective fields.

Furthermore, I want to thank Jannis Weinacker and Jonathan Ludwig Günter Schneider for the enthusiasm and hard work they put in during their respective Master's theses. I have very much enjoyed our cooperation in common projects.

I am indebted to everybody who took the time and tenaciously proof-read the prose I have brought to paper. Your efforts helped me in raising the quality of my work to a level otherwise not possible. Therefore, I want to specifically thank again my former students and now colleagues Jannis Weinacker and Jonathan Schneider, as well as Yi Chen, Tobias Frenzel and my father Dieter Groß for their suggestions.

Naturally, I also want to thank the other group members I had the pleasure of working with during the last four years. I especially valued the mutual support and general atmosphere of fellowship in our group, which made me feel more like working among friends than mere colleagues.

Finally, I want to express my deepest gratitude to my parents Rita and Dieter Groß, and to my girlfriend Annica Antoni. Your support throughout all these years made it possible for me to achieve this early-set life goal of mine.

Tools

For the sake of integrity, I summarize the tools and software I used to realize the experimental setup, perform experiments and data analysis, and create this manuscript.

- Microsoft Visual Studio 2019 was used to write the software for the experimental setup in C++.
- Zemax OpticStudio and MATLAB were used do design the beam path for the confocal-microscopy branch and the vibrometry branch.
- MATLAB was used to implement the analysis of the image data, the demodulation of the data from the laser-Doppler-vibrometry branch, and plotting of the results.
- ImageJ (Fiji) was used to measure lengths in image data, for e.g. the field of view calibration.
- Blender was used for the visualization of the 3D-fluorescence data taken from the metamaterial unit cells, and for other figures throughout this thesis.
- Inkscape and CorelDraw were used to create vector drawings of schematics, typeset data-plots when needed and assemble multi-panel figures.
- Vector graphics from the ComponentLibrary created by Alexander Franzen (2006) were used and modified as needed under (CC BY-NC 3.0).
- The MATLAB toolbox export_fig Version 3.40.0.0 created by Yair Altman was used to export plots from MATLAB. Retrieved on 8th of August 2023.
- The online dictionaries dict.cc and leo.org were used to refine the language of this work.
- LaTeX was used to write this thesis, together with the LaTeX2e class template for diploma theses, based on wissdoc.cls by Roland Bless, 1996-2001 and heavily modified by Robert Schittny, 2015.

Appendix A

A Supplementary Derivations

A.1 Derivation of Symmetry of Stiffnes Tensor

Following [14], for a linear elastic material with stiffness tensor (matrix) $\mathbf{C}$, symmetric small strain tensor $\boldsymbol{\epsilon}$ and symmetric stress tensor σ, it can be shown that $\mathbf{C}$ is also symmetric when inspecting the conservation of potential energy U_{pot}:

$$U_{\text{pot}} = \frac{1}{2}\sigma\boldsymbol{\epsilon} = \frac{1}{2}(\mathbf{C}\boldsymbol{\epsilon})\boldsymbol{\epsilon} = \frac{1}{2}\mathbf{C}\epsilon^2, \tag{A.1}$$

$$\frac{\partial U_{\text{pot}}}{\partial \boldsymbol{\epsilon}} = \frac{\partial}{\partial \boldsymbol{\epsilon}}\left(\frac{1}{2}\mathbf{C}\boldsymbol{\epsilon}^2\right) = \mathbf{C}\boldsymbol{\epsilon} = \sigma, \quad \Rightarrow \quad \sigma_{ij} = \frac{\partial U_{\text{pot}}}{\partial \epsilon_{ij}}, \tag{A.2}$$

$$C_{ijkl} = \frac{\partial \sigma_{ij}}{\partial \epsilon_{kl}} = \frac{\partial}{\partial \epsilon_{kl}}\left(\frac{\partial U_{\text{pot}}}{\partial \epsilon_{ij}}\right) = \frac{\partial^2 U_{\text{pot}}}{\partial \epsilon_{ij}\partial \epsilon_{kl}} = \frac{\partial^2 U_{\text{pot}}}{\partial \epsilon_{kl}\partial \epsilon_{ij}}. \tag{A.3}$$

Since U_{pot} is continuous, the order of the derivation in the last term does not matter. Thus, $\mathbf{C}$ is symmetric.

A.2 Derivation of LDV Detector Signal

Derivation is found in similar manner in chapter 2.1 and following of [82]. The signal of the detector $u(t)$ depends on the absolute square of the real summed electric fields E_1 and E_2:

$$\begin{aligned} E_1(t) &= E_{1,0}\cos(2\pi f_1 t + \phi_1), \\ E_2(t) &= E_{2,0}\cos(2\pi f_2 t + \phi_2). \end{aligned}$$

Therefore:

$$\begin{aligned} i(t) &\propto \left(E_{1,0}\cos(2\pi f_1 t + \phi_1) + E_{2,0}\cos(2\pi f_2 t + \phi_2)\right)^2 \\ &= E_{1,0}^2\cos^2(2\pi f_1 + \phi_1) + E_{2,0}^2\cos^2(2\pi f_2 + \phi_2) \\ &\quad + 2E_{1,0}E_{2,0}\cos(2\pi f_1 t + \phi_1)\cos(2\pi f_2 t + \phi_2) \\ &= E_{1,0}^2\cos^2(2\pi f_1 + \phi_1) + E_{2,0}^2\cos^2(2\pi f_2 + \phi_2) \\ &\quad + E_{1,0}E_{2,0}\cos(2\pi(f_1 + f_2)t + \phi_1 + \phi_2) \\ &\quad + E_{1,0}E_{2,0}\cos(2\pi(f_1 - f_2)t + \phi_1 - \phi_2) \\ &= \bar{E} + E_{1,0}E_{2,0}\cos(2\pi(f_1 - f_2)t + \phi_1 - \phi_2). \end{aligned}$$

A photodetector can neither respond to the high optical frequencies f_1 and f_2 nor their sum $f_1 + f_2$. The resulting output will be an averaged and constant (DC) signal $\bar{E}$. A similar consideration can be made for the complex fields described by exponentials, however, the result remains unchanged when taking the absolute square of the resulting field. To arrive at the result above, the Werner trigonometric formula is used:

$$2\cos\alpha\cos\beta = \cos(\alpha + \beta) + \cos(\alpha - \beta).$$

Appendix B

B Components and Calibrations of the Experimental Setup

Table B.1: Component list of the self-built experimental setup with the confocal imaging branch only. The components are broken down according to their designations used in the schematics (Figure 4.1, Figure 4.7) and text with their corresponding models and manufacturers. Reproduced and adapted from [94] under CC BY 4.0), published by Science Advances 2021.

Component	**Designation**	**Model**
Laser	-	LCX-532S-200, Oxxius
Optical isolator	Faraday isolator	LINOS FI-530-2SV, QIOPTIQ
Halve-wave plate	R1	$\lambda/2$ 532 nm low, B. Halle
Halve-wave plate	R2	WPMQ10M-532, Thorlabs
Clean-up filter	Filter	FLH532-10, Thorlabs
Polarizing beam-splitter cube	PBS	PTW15, B. Halle
Thin-film beam splitter	TFBS	BSW10, Thorlabs
Galvanometer scanner	-	intelliSCAN se 10, Scanlab
Scan lens	SC	2x AC508-250-A, Thorlabs
Tube lens	TL	AC508-200-A-ML, Thorlabs
Objective lens	OL	50x CFI60 TU Plan Epi ELWD, Nikon
Detection lense	DL1	AC254-040-A-ML, Thorlabs
Multimode fiber	-	M122L01 200µm NA 0.22, Thorlabs
Avalanche photodiode module	APD1	C10508-01SPL, Hamamatsu
xyz-Translation stage	-	3x Q-545.140, Physik Instrumente
Piezoelectric transducer	-	PL055.31 PICMA®, Physik Instrumente
Drive signal amplifier	Amplifier	A 1230-01 linear amplifier, Hubert
Vibrometry signal amplifier	RF-amplifier	HVA-200M-40-B, Femto
Function generator	-	33612A, Keysight
Data acquisition unit	DAQ1	ATS9130, AlazarTech
Scanner control card	RTC6	RTC6, Scanlab

Table B.2: Extension to Table B.1 of the component list for the self-built experimental setup. The components added (or in case of the objective lens, replaced) for the vibrometry branch (cf. Figure 4.7) are broken down in the same manner. Reproduced and adapted from [92] under (CC BY 4.0), published by Advanced Materials 2023.

Component	**Designation**	**Model**
Beam splitter cube	BSC1	BS013, Thorlabs
Beam splitter cube	BSC2	BS028, Thorlabs
Objective lens	OL	Plan L 50x/0.60, Leitz Wetzlar
Acousto-optic modulator	AOM	MT80-B30A1,5-VIS, AA Opto-Electronic
Detection lense	DL2	AC254-040-A-ML, Thorlabs
Multimode fiber	-	M122L01 200µm NA 0.22, Thorlabs
Avalanche photodiode module	APD2	C12702-11, Hamamatsu
Vibrometry signal amplifier	RF-amplifier	HVA-200M-40-B, Femto
Data acquisition unit	DAQ2	M4i4450-x8, Spectrum Instrumentation

Table B.3: Calibration factors for different objective lenses. The second row contains the conversion factors of 1 µm into bit-levels of the 20-bit position encoder of the RTC6 galvanometer scanner real-time controller card. The second row contains the displacement amplitude correction factors, with which a displacement amplitude has to be multiplied to obtain a correct absolute displacement value.

Objective lens	Wetzlar PL 8x/0.18	Wetzlar Plan L 25x/0.4	Wetzlar Plan L 50x/0.6	Nikon CFI60 TU Plan Epi ELWD 50x/0.6
Conversion in μm^{-1}	740	230	460	600
Amplitude Correction	1	0.95	1.02	1.90

Bibliography

[1] R. M. Walser, "Electromagnetic metamaterials", in SPIE Proceedings, edited by A. Lakhtakia, W. S. Weiglhofer, and I. J. Hodgkinson (July 2001) (cited on page 3).

[2] M. Kadic, G. W. Milton, M. van Hecke, and M. Wegener, "3D metamaterials", Nat. Rev. Phys. **1**, 198–210 (2019) (cited on pages 3, 4).

[3] R. A. Shelby, D. R. Smith, and S. Schultz, "Experimental Verification of a Negative Index of Refraction", Science **292**, 77–79 (2001) (cited on pages 3, 5, 80).

[4] S. Linden, C. Enkrich, M. Wegener, J. Zhou, T. Koschny, and C. M. Soukoulis, "Magnetic Response of Metamaterials at 100 Terahertz", Science **306**, 1351–1353 (2004) (cited on pages 3, 5, 80).

[5] C. M. Soukoulis, S. Linden, and M. Wegener, "Negative Refractive Index at Optical Wavelengths", Science **315**, 47–49 (2007) (cited on pages 3, 5).

[6] X. Ren, R. Das, P. Tran, T. D. Ngo, and Y. M. Xie, "Auxetic metamaterials and structures: a review", Smart Mater. Struct. **27**, 023001 (2018) (cited on page 3).

[7] R. S. Kshetrimayum, "A brief intro to metamaterials", IEEE Potentials **23**, 44–46 (2004) (cited on page 3).

[8] University Charles Kittel, *Einführung in die Festkörperphysik*, de, 13th ed. (Oldenbourg Wissenschaftsverlag, Aug. 2017) (cited on pages 4, 17, 20, 80, 83).

[9] M. Wegener, "Metamaterials beyond optics", Science **342**, 939–940 (2013) (cited on page 4).

[10] M. Kadic, T. Bückmann, R. Schittny, and M. Wegener, "Metamaterials beyond electromagnetism", Rep. Prog. Phys. **76**, 126501 (2013) (cited on page 4).

[11] R. Craster, S. Guenneau, M. Kadic, and M. Wegener, "Mechanical metamaterials", Reports on Progress in Physics **86**, 094501 (2023) (cited on page 4).

[12] M. Kadic, T. Bückmann, N. Stenger, M. Thiel, and M. Wegener, "On the practicability of pentamode mechanical metamaterials", Appl. Phys. Lett. **100**, 191901 (2012) (cited on pages 4, 100).

[13] T. Frenzel, J. Köpfler, E. Jung, M. Kadic, and M. Wegener, "Ultrasound experiments on acoustical activity in chiral mechanical metamaterials", Nat. Commun. **10**, 1–6 (2019) (cited on pages 4, 5, 33, 91).

[14] P. L. Gould and Y. Feng, *Introduction to Linear Elasticity* (Springer International Publishing, 2018) (cited on pages 4, 8, 15, 136).

[15] T. Baldacchini, *Three-Dimensional Microfabrication Using Two-Photon Polymerization Fundamentals, Technology, and Applications* (William Andrew, Amsterdam Boston, 2015), p. 512 (cited on pages 4, 22).

[16] T. Bückmann, N. Stenger, M. Kadic, J. Kaschke, A. Frölich, T. Kennerknecht, C. Eberl, M. Thiel, and M. Wegener, "Tailored 3D Mechanical Metamaterials Made by Dip-in Direct-Laser-Writing Optical Lithography", Advanced Materials **24**, 2710–2714 (2012) (cited on page 4).

[17] T. Bückmann, M. Thiel, M. Kadic, R. Schittny, and M. Wegener, "An elasto-mechanical unfeelability cloak made of pentamode metamaterials", Nat. Commun. **5**, 1–6 (2014) (cited on pages 4, 33, 100, 101).

[18] J. Qu, M. Kadic, A. Naber, and M. Wegener, "Micro-structured two-component 3D metamaterials with negative thermal-expansion coefficient from positive constituents", Sci. Rep. **7**, 40643 (2017) (cited on pages 4, 33).

[19] T. Frenzel, V. Hahn, P. Ziemke, J. L. G. Schneider, Y. Chen, P. Kiefer, P. Gumbsch, and M. Wegener, "Large characteristic lengths in 3D chiral elastic metamaterials", Communications Materials **2** (2021) (cited on pages 4, 33).

[20] J. Köpfler, T. Frenzel, J. Schmalian, and M. Wegener, "Fused-Silica 3D Chiral Metamaterials via Helium-Assisted Microcasting Supporting Topologically Protected Twist Edge Resonances with High Mechanical Quality Factors", Advanced Materials **33**, 2103205 (2021) (cited on pages 4, 33).

[21] A. Münchinger, L.-Y. Hsu, F. Fürniß, E. Blasco, and M. Wegener, "3D optomechanical metamaterials", Materials Today **59**, 9–17 (2022) (cited on page 4).

[22] L. Landau, "Theory of the Superfluidity of Helium II", Phys. Rev. **60**, 356–358 (1941) (cited on pages 5, 80).

[23] R. P. Feynman, "Atomic Theory of the Two-Fluid Model of Liquid Helium", Phys. Rev. **94**, 262–277 (1954) (cited on pages 5, 80).

[24] R. P. Feynman and M. Cohen, "Energy Spectrum of the Excitations in Liquid Helium", Phys. Rev. **102**, 1189–1204 (1956) (cited on pages 5, 80).

[25] D. G. Henshaw and A. D. B. Woods, "Modes of Atomic Motions in Liquid Helium by Inelastic Scattering of Neutrons", Phys. Rev. **121**, 1266–1274 (1961) (cited on pages 5, 80).

[26] Y. Chen, M. Kadic, and M. Wegener, "Roton-like acoustical dispersion relations in 3D metamaterials", Nature Communications **12** (2021) (cited on pages 5, 80, 81, 83–85, 116).

[27] J. Kishine, A. S. Ovchinnikov, and A. A. Tereshchenko, "Chirality-Induced Phonon Dispersion in a Noncentrosymmetric Micropolar Crystal", Phys. Rev. Lett. **125**, 245302 (2020) (cited on pages 5, 81, 90–92, 115).

[28] G. W. Milton and A. V. Cherkaev, "Which elasticity tensors are realizable?", ASME J. Eng. Mater. Technol. **117**, 483–493 (1995) (cited on pages 5, 99, 100, 111, 113).

[29] R. Hooke, *Lectures de potentia restitutiva, or of spring explaining the power of springing bodies* (John Martyn, London, 1678) (cited on pages 8, 13, 100).

[30] W. S. Slaughter, *The linearized theory of elasticity* (Springer Science & Business Media, 2012) (cited on pages 8, 16).

[31] S. P. Timoshenko and J. N. Goodier, *Theory of elasticity*, Engineering societies monographs (McGraw-Hill Education Pvt Limited, 2010) (cited on page 8).

[32] I. Newton, I. Cohen, and A. Whitman, *The Principia: Mathematical Principles of Natural Philosophy*, The Principia: Mathematical Principles of Natural Philosophy (University of California Press, 1999) (cited on pages 10, 15).

[33] C. Pettit, *The Cauchy Stress Tensor*, (2021) https://www.youtube.com/watch?v=CGDziWoEEgo&ab_channel=Dr.ClaytonPettit (cited on page 11).

[34] C. Pettit, *The Small (Infinitesimal) and Green Strain Tensors*, (2021) https://www.youtube.com/watch?v=rt4wlXOD5S8&ab_channel=Dr.ClaytonPettit (cited on page 13).

[35] W. Demtröder, *Experimentalphysik 1* (Springer Berlin Heidelberg, 2015) (cited on page 15).

[36] S. Hunklinger, *Festkörperphysik* (DE GRUYTER, Apr. 2014) (cited on pages 16, 17).

[37] *Festkörperphysik* (Springer Berlin Heidelberg, 2009) (cited on page 17).

[38] L. Brillouin, "Les électrons libres dans les métaux et le role des réflexions de Bragg", Journal de Physique et le Radium **1**, 377–400 (1930) (cited on page 18).

[39] A. W, N. Ashcroft, N. Mermin, N. Mermin, and B. C. P. Company, *Solid State Physics*, HRW international editions (Holt, Rinehart and Winston, 1976) (cited on page 21).

[40] H.-B. Sun, S. Matsuo, and H. Misawa, "Three-dimensional photonic crystal structures achieved with two-photon-absorption photopolymerization of resin", Appl. Phys. Lett. **74**, 786–788 (1999) (cited on page 22).

[41] S. Kawata, H.-B. Sun, T. Tanaka, and K. Takada, "Finer features for functional microdevices", Nature **412**, 697–698 (2001) (cited on pages 22, 23).

[42] P. A. Deymier, *Acoustic metamaterials and phononic crystals*, Vol. 173 (Springer Science & Business Media, 2013) (cited on page 22).

[43] S. Maruo, O. Nakamura, and S. Kawata, "Three-dimensional microfabrication with two-photon-absorbed photopolymerization", Optics Letters **22**, 132 (1997) (cited on page 22).

[44] B. H. Cumpston, S. P. Ananthavel, S. Barlow, D. L. Dyer, J. E. Ehrlich, L. L. Erskine, A. A. Heikal, S. M. Kuebler, I.-Y. S. Lee, D. McCord-Maughon, J. Qin, H. Röckel, M. Rumi, X.-L. Wu, S. R. Marder, and J. W. Perry, "Two-photon polymerization initiators for three-dimensional optical data storage and microfabrication", Nature **398**, 51–54 (1999) (cited on page 22).

[45] Y. Chen, J. L. G. Schneider, M. F. Groß, K. Wang, S. Kalt, P. Scott, M. Kadic, and M. Wegener, "Observation of Chirality-Induced Roton-Like Dispersion in a 3D Micropolar Elastic Metamaterial", Advanced Functional Materials, 2302699 (cited on pages 23, 79, 90, 92, 93, 95–98).

[46] J. Fischer, "Three-dimensional optical lithography beyond the diffraction limit", Karlsruhe, Karlsruher Institut für Technologie (KIT), PhD thesis (Karlsruhe, 2012) (cited on page 23).

[47] T. Frenzel, "On 3D Chiral Mechanical Metamaterials", PhD thesis (Karlsruher Institut für Technologie (KIT), 2020), 208 pp. (cited on pages 23, 25, 83).

[48] J. B. Mueller, J. Fischer, F. Mayer, M. Kadic, and M. Wegener, "Polymerization Kinetics in Three-Dimensional Direct Laser Writing", Adv. Mater. **26**, 6566–6571 (2014) (cited on page 23).

[49] V. Hahn, P. Kiefer, T. Frenzel, J. Qu, E. Blasco, C. Barner-Kowollik, and M. Wegener, "Rapid assembly of small materials building blocks (Voxels) into large functional 3D metamaterials", Adv. Funct. Mater., 1907795 (2020) (cited on page 23).

[50] V. Hahn, "On 3D Laser Micro- and Nanoprinting: Faster, Finer, and More Affordable", PhD thesis (Karlsruher Institut für Technologie (KIT), Karlsruhe, 2022) (cited on page 23).

[51] Nanoscribe GmbH, (2015) www.nanoscribe.de (cited on pages 24, 25).

[52] J. Fischer and M. Wegener, "Three-dimensional optical laser lithography beyond the diffraction limit", Laser & Photonics Reviews **7**, 22–44 (2013) (cited on page 26).

[53] H. Goldmann, "Spaltlampenphotographie und – photometric", Ophthalmologica **98**, 257–270 (1939) (cited on page 30).

[54] M. Minsky, *Microscopy apparatus*, US Patent, US3013467A, Dec. 1961 (cited on page 30).

[55] M. Minsky, "Memoir on inventing the confocal scanning microscope", Scanning **10**, 128–138 (1988) (cited on pages 30, 31).

[56] G. Cox, *Optical Imaging Techniques in Cell Biology, Second edition* (CRC Press, 2012), p. 316 (cited on page 30).

[57] P. Davidovits and D. M. Egger, "Scanning Laser Microscope", Nature **223**, 831–831 (1969) (cited on page 31).

[58] J. B. Pawley, ed., *Handbook of Biological Confocal Microscopy* (Springer US, 1995) (cited on page 31).

[59] *C10508-01*, Cat. No. KACC1217E03, Hamamatsu Photonics (Sept. 2017) (cited on pages 31, 38, 70).

[60] E. Abbe, "Beiträge zur Theorie des Mikroskops und der mikroskopischen Wahrnehmung", Archiv für Mikroskopische Anatomie **9**, 413–468 (1873) (cited on page 32).

[61] E. Hecht, *Optik* - (Walter de Gruyter GmbH & Co KG, Berlin, 2018) (cited on pages 32, 44).

[62] B. Richards and E. Wolf, "Electromagnetic Diffraction in Optical Systems. II. Structure of the Image Field in an Aplanatic System", Proceedings of the Royal Society of London. Series A, Mathematical and Physical Sciences **253**, 358–379 (1959) (cited on pages 32, 56).

[63] G. Cox and C. J. Sheppard, "Practical limits of resolution in confocal and non-linear microscopy", Microscopy Research and Technique **63**, 18–22 (2003) (cited on page 32).

[64] J. Zhao, Y. Sang, and F. Duan, "The state of the art of two-dimensional digital image correlation computational method", Engineering Reports **1** (2019) (cited on page 33).

[65] T. Frenzel, M. Kadic, and M. Wegener, "Three-dimensional mechanical metamaterials with a twist", Science **358**, 1072–1074 (2017) (cited on page 33).

[66] J. Köpfler, "On Topological Mechanics of 3D Chiral Metamaterials", 43.32.02; LK 01, PhD thesis (Karlsruher Institut für Technologie (KIT), 2022), 140 pp. (cited on page 33).

[67] T. Frenzel, J. Köpfler, A. Naber, and M. Wegener, "Detecting atomic-scale displacements by optical-image cross-correlation analysis and 3D printed marker arrays", submitted (2020) (cited on pages 33, 35).

[68] C. Shannon, "Communication in the Presence of Noise", Proceedings of the IRE **37**, 10–21 (1949) (cited on pages 35, 70, 72, 73).

[69] C. Doppler, "Ueber das farbige Licht der Doppelsterne und einiger anderer Gestirne des Himmels.", in *Abhandlungen der k. böhm. Gesellschaft der Wissenschaften*, Vol. 2, 5 (Verlag der Königl. Böhm. Gesellschaft der Wissenschaften, Prag, May 1842) (cited on page 36).

[70] A. Einstein, "Zur Elektrodynamik bewegter Körper", Annalen der Physik **322**, 891–921 (1905) (cited on pages 36, 37).

[71] T. H. MAIMAN, "Stimulated Optical Radiation in Ruby", Nature **187**, 493–494 (1960) (cited on page 36).

[72] Y. Yeh and H. Z. Cummins, "Localized Fluid Flow Measurements with an He–Ne Laser Spectrometer", Applied Physics Letters **4**, 176–178 (1964) (cited on page 36).

[73] Polytec GmbH, (2023) `https://www.polytec.com/de` (cited on pages 36, 129).

[74] C. M. Sutton, "Accelerometer Calibration by Dynamic Position Measurement Using Heterodyne Laser Interferometry", Metrologia **27**, 133–138 (1990) (cited on page 36).

[75] A. M. Huber, C. Schwab, T. Linder, S. J. Stoeckli, M. Ferrazzini, N. Dillier, and U. Fisch, "Evaluation of Eardrum Laser Doppler Interferometry as a Diagnostic Tool", The Laryngoscope **111**, 501–507 (2001) (cited on page 36).

[76] D. E. Oliver, "Scanning laser vibrometer for dynamic deflection shape characterization of aerospace structures", in SPIE Proceedings, edited by G. W. Kamerman (June 1995) (cited on page 36).

[77] C. I. Moir, "Miniature laser doppler velocimetry systems", in Optical Sensors 2009, edited by F. Baldini, J. Homola, and R. A. Lieberman (May 2009) (cited on page 36).

[78] G. Trainiti, J. J. Rimoli, and M. Ruzzene, "Optical evaluation of the wave filtering properties of graded undulated lattices", Journal of Applied Physics **123**, 10.1063/1.5011369 (2017) (cited on page 36).

[79] M. Wormser, D. A. Kiefer, S. J. Rupitsch, and C. Körner, "Comparison of Transmission Measurement Methods of Elastic Waves in Phononic Band Gap Materials", Materials **14**, 1133 (2021) (cited on page 36).

[80] C. Rembe and L. Mignanelli, "Introduction to Laser-Doppler Vibrometry", in *Bioanalysis* (Springer International Publishing, 2020), pp. 9–21 (cited on pages 36, 39).

[81] W. Osten, ed., *Optical Inspection of Microsystems, Second Edition* (CRC Press, 2019), p. 584 (cited on pages 36, 43–46, 64).

[82] E. P. Tomasini and P. Castellini, eds., *Laser Doppler Vibrometry* (Springer Berlin Heidelberg, 2020) (cited on pages 36, 136).

[83] P. Chiariotti, C. Rembe, P. Castellini, and M. Allen, "Laser Doppler Vibrometry Measurements in Structural Dynamics", in *Handbook of Experimental Structural Dynamics*, edited by R. Allemang and P. Avitabile (Springer New York, New York, NY, 2020), pp. 1–45 (cited on pages 36, 39, 44).

[84] J. D. Jackson, *Klassische Elektrodynamik* (DE GRUYTER, Dec. 2013) (cited on page 37).

[85] A. Gjurchinovski, "The Doppler effect from a uniformly moving mirror", European Journal of Physics **26**, 643–646 (2005) (cited on page 37).

[86] A. A. Michelson and E. W. Morley, "On the relative motion of the Earth and the luminiferous ether", American Journal of Science **s3-34**, 333–345 (1887) (cited on page 38).

[87] L. Mach, "Über einen Interferenzrefraktor.", Zeitschrift für Instrumentenkunde, 89–93 (1892) (cited on page 38).

[88] L. Zehnder, "Ein neuer Interferenzrefraktor.", Zeitschrift für Instrumentenkunde, 275–285 (1891) (cited on page 38).

[89] J. Maxwell, *A Treatise on Electricity and Magnetism*, A Treatise on Electricity and Magnetism Bd. 1 (Clarendon Press, 1873) (cited on page 39).

[90] D. Colton and R. Kress, *Inverse Acoustic and Electromagnetic Scattering Theory* (Springer Berlin Heidelberg, 1998) (cited on page 42).

[91] M. Schmid, D. Ludescher, and H. Giessen, "Optical properties of photoresists for femtosecond 3D printing: refractive index, extinction, luminescence-dose dependence, aging, heat treatment and comparison between 1-photon and 2-photon exposure", Opt. Mater. Express **9**, 4564–4577 (2019) (cited on page 44).

[92] M. F. Groß, J. L. G. Schneider, Y. Wei, Y. Chen, S. Kalt, M. Kadic, X. Liu, G. Hu, and M. Wegener, "Tetramode Metamaterials as Phonon Polarizers", Advanced Materials **35**, 2211801 (2023) (cited on pages 46, 60, 61, 68, 72, 99, 101–103, 105–108, 113, 139).

[93] M. Bauer, F. Ritter, and G. Siegmund, "High-precision laser vibrometers based on digital Doppler signal processing", in SPIE Proceedings, edited by E. P. Tomasini (May 2002) (cited on page 46).

[94] J. A. I. Martínez, M. F. Groß, Y. Chen, T. Frenzel, V. Laude, M. Kadic, and M. Wegener, "Experimental observation of roton-like dispersion relations in metamaterials", Science Advances **7**, eabm2189 (2021) (cited on pages 50, 51, 70, 71, 79, 81, 83–86, 88, 89, 138).

[95] A. Negrean and H. D. Mansvelder, "Optimal lens design and use in laser-scanning microscopy", Biomed. Opt. Express **5**, 1588–1609 (2014) (cited on page 52).

[96] Scanlab GmbH, (2023) https://www.scanlab.de/de/produkte/scan-zubehoer/scan-objektive (cited on page 54).

[97] C. J. Cogswell, C. J. R. Sheppard, M. C. Moss, and C. V. Howard, "A method for evaluating microscope objectives to optimize performance of confocal systems", Journal of Microscopy **158**, 177–185 (1990) (cited on page 56).

[98] H.-J. von Martens, "Invited Article: Expanded and improved traceability of vibration measurements by laser interferometry", Review of Scientific Instruments **84**, 10.1063/1.4845916 (2013) (cited on page 64).

[99] H. Mishina, T. Asakura, and S. Nagai, "A laser Doppler microscope", Optics Communications **11**, 99–102 (1974) (cited on page 64).

[100] C. Rembe and A. Dräbenstedt, "Laser-scanning confocal vibrometer microscope: Theory and experiments", Review of Scientific Instruments **77** (2006) (cited on pages 64, 129).

[101] L. G. Gouy, *Sur une propriété nouvelle des ondes lumineuses*, fre (Gauthier-Villars Paris, Paris, 1890) (cited on page 64).

[102] E. Abbe, "VII.-On the Estimation of Aperture in the Microscope.", Journal of the Royal Microscopical Society **1**, 388–423 (1881) (cited on page 65).

[103] T. Meeker, "Thickness mode piezoelectric transducers", Ultrasonics **10**, 26–36 (1972) (cited on page 69).

[104] A. V. Oppenheim, R. W. Schafer, and J. R. Buck, *Discrete-Time Signal Processing (2nd Ed.)* (Prentice-Hall, Inc., USA, 1999) (cited on page 73).

[105] *MathWorks Documentation*, (2023) https://de.mathworks.com/help/matlab/ref/fft.html (cited on page 73).

[106] M. Frigo and S. G. Johnson, "The Design and Implementation of FFTW3", Proceedings of the IEEE **93**, Special issue on "Program Generation, Optimization, and Platform Adaptation", 216–231 (2005) (cited on page 73).

[107] A. Brandt, *Noise and Vibration Analysis* (Wiley, Jan. 2011) (cited on pages 73, 77).

[108] D. R. Smith, J. B. Pendry, and M. C. K. Wiltshire, "Metamaterials and Negative Refractive Index", Science **305**, 788–792 (2004) (cited on page 80).

[109] S. A. Cummer, J. Christensen, and A. Alù, "Controlling sound with acoustic metamaterials", Nature Reviews Materials **1** (2016) (cited on page 80).

[110] A. C. Eringen and E. Suhubi, "Nonlinear theory of simple micro-elastic solids—I", Int. J. Eng. Sci. **2**, 189–203 (1964) (cited on pages 81, 90, 92).

[111] E. Suhubl and A. C. Eringen, "Nonlinear theory of micro-elastic solids—II", Int. J. Eng. Sci. **2**, 389–404 (1964) (cited on pages 81, 90, 92).

[112] K. Wang, Y. Chen, M. Kadic, C. Wang, and M. Wegener, "Nonlocal interaction engineering of 2D roton-like dispersion relations in acoustic and mechanical metamaterials", Communications Materials **3** (2022) (cited on page 89).

[113] K. Wang, Y. Chen, M. Kadic, C. Wang, and M. Wegener, "Cubic-symmetry acoustic metamaterials with roton-like dispersion relations", Acta Mechanica Sinica **39** (2023) (cited on page 89).

[114] Y. Chen, M. A. A. Abouelatta, K. Wang, M. Kadic, and M. Wegener, "Nonlocal Cable-Network Metamaterials", Advanced Materials **35**, 2209988 (2023) (cited on page 89).

[115] R. S. Lakes and R. L. Benedict, "Noncentrosymmetry in micropolar elasticity", Int. J. Eng. Sci. **20**, 1161–1167 (1982) (cited on page 90).

[116] A. C. Eringen, *Microcontinuum field theories: I. Foundations and solids* (Springer Science & Business Media, 2012) (cited on pages 90, 92).

[117] T. Kelvin, "The second Robert Boyle lecture", J. Oxf. Univ. Jr. Sci. Club **18**, 25 (1894) (cited on page 90).

[118] L. Whyte, "Chirality", Nature **180**, 513–513 (1957) (cited on page 90).

[119] L. Whyte, "Chirality", Nature **182**, 198–198 (1958) (cited on page 90).

[120] Y. Chen, M. Kadic, S. Guenneau, and M. Wegener, "Isotropic Chiral Acoustic Phonons in 3D Quasicrystalline Metamaterials", Phys. Rev. Lett. **124**, 235502 (2020) (cited on page 91).

[121] Y. Chen, T. Frenzel, S. Guenneau, M. Kadic, and M. Wegener, "Mapping acoustical activity in 3D chiral mechanical metamaterials onto micropolar continuum elasticity", J. Mech. Phys. Solids **137**, 103877 (2020) (cited on page 92).

[122] M. F. Groß, J. L. Schneider, Y. Chen, M. Kadic, and M. Wegener, "Dispersion Engineering by Hybridizing the Back-Folded Soft Mode of Monomode Elastic Metamaterials with Stiff Acoustic Modes", Advanced Materials **n/a**, 2307553 (cited on pages 99, 111–114, 116–122).

[123] G. W. Milton and A. Sawicki, "Theory of composites. Cambridge monographs on applied and computational mathematics", Appl. Mech. Rev. **56**, B27–B28 (2003) (cited on page 100).

[124] R. Schittny, T. Bückmann, M. Kadic, and M. Wegener, "Elastic measurements on macroscopic three-dimensional pentamode metamaterials", Appl. Phys. Lett. **103**, 231905 (2013) (cited on page 100).

[125] S. Brûlé, E. H. Javelaud, S. Enoch, and S. Guenneau, "Experiments on Seismic Metamaterials: Molding Surface Waves", Phys. Rev. Lett. **112**, 133901 (2014) (cited on page 101).

[126] A. Martin, M. Kadic, R. Schittny, T. Bückmann, and M. Wegener, "Phonon band structures of three-dimensional pentamode metamaterials", Phys. Rev. B **86**, 155116 (2012) (cited on pages 101, 104).

[127] L. D. Barron, *Molecular Light Scattering and Optical Activity*, 2nd ed. (Cambridge University Press, 2004) (cited on pages 101, 109).

[128] C. Rembe and R. Muller, "Measurement system for full three-dimensional motion characterization of MEMS", Journal of Microelectromechanical Systems **11**, 479–488 (2002) (cited on page 129).

[129] A. Voss, L. Seyfert, N. Schwesinger, and W. Hemmert, "Stroboscopic video microscopy with sub-nanometer accuracy for characterizing and monitoring MEMS", in Nondestructive Characterization and Monitoring of Advanced Materials, Aerospace, Civil Infrastructure, and Transportation XVI, edited by P. J. Shull, T. Yu, A. L. Gyekenyesi, and H. F. Wu (Apr. 2022) (cited on page 129).

[130] C. Rembe, R. Kowarsch, W. Ochs, A. Dräbenstedt, M. Giesen, and M. Winter, "Optical three-dimensional vibrometer microscope with picometer-resolution in x, y, and z", Optical Engineering **53**, 034108 (2014) (cited on page 129).